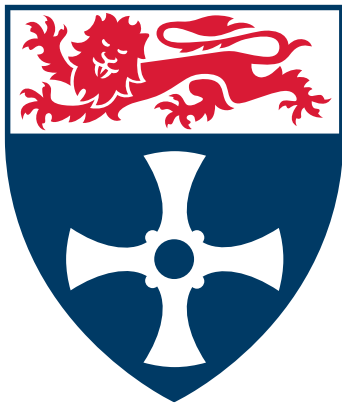


Diamond-doped Silica Aerogels for Solar  
Geoengineering

by

Jovana Vukajlovic



**Newcastle**  
University

Supervisor: Prof Lidija Šiller

School of Engineering

Newcastle University, UK

The dissertation is submitted for the degree of

Doctor of Philosophy

July 2021



## Acknowledgement

Firstly, I would like to thank my supervisor, Prof Lidija Šiller for giving me the opportunity to do this PhD and guiding me throughout my studies. I would like to thank Dr Ian Forbes at Northumbria University for helping us measure the optical properties of our materials. Many thanks to Dr Leonardo Lari at York University and Dr Volkan Degirmenci at Warwick University for their help in sample characterization. I would also like to express my gratitude to my research group and the staff at Newcastle University for their significant support throughout this project. Also, I would like to thank Steve Laidler for critical reading of the thesis. Finally, I would like to thank EPSRC Centre for Doctoral Training in Diamond Science and Technology for financial support.

## Abstract

Geoengineering includes many techniques aimed to fight the global warming, which is one of the biggest problems today. Even though aerosol injection into stratosphere is one of the most promising solar geoengineering techniques, sulfate aerosols, which are suggested for such an application, show significant drawbacks such as infrared (IR) absorption and ozone degradation. Here, a novel composite material comprised of diamonds dispersed in a silica aerogel network is investigated and compared to pure silica aerogel. Silica aerogels are ultralight, highly porous, transparent and can host particles, while fulfilling particle size limitation in terms of potential health risks for humans during respiration. In theoretical models, diamond particles with high refractive index ( $\sim 2.41$ ) showed outstanding up-scattering among other materials, without IR absorption. Moreover, in recent years, the low-cost production of silica aerogels suitable for large scale production has been developed and diamond powders can be purchased at low cost in ton quantities.

Before doping of the silica aerogels, diamond part of the composite was studied since the diamond is outstanding light scatterer and also for future applications of the diamond particles. Two types of diamond particles were used: high pressure high temperature (HPHT) microdiamonds ( $\sim 500$  nm in size) and detonation nanodiamonds (DNDs) ( $\sim 3$  nm in size). Raw HPHT microdiamonds were treated with 1-undecene and zirconia beads and nuclear magnetic resonance (NMR) and Fourier-transform infrared (FTIR) spectroscopy were used to detect the alkyl groups on the surface of the treated HPHT microdiamonds. Both HPHT microdiamonds were free of graphitic  $sp^2$  carbon (Raman scattering). Nanodiamond colloids, original 4 wt% (as purchased) and diluted 1 wt%, were studied in terms of Zeta potential, pH and dynamic light scattering (DLS) measurements to assess the stability of nanoparticles. The results suggest that nanodiamond colloids are not stable in air or after dilution as the particles tend to agglomerate.

Both micro- and nanodiamonds were added to tetraethoxysilane (TEOS)-based silica aerogels. In case of microdiamonds, concentrations of 500, 700 and 900 ppm of diamond particles in the precursor sol before gelation were used. It was observed that the higher the diamond concentration in the sol, the final aerogel contained more wt% of diamond, with the maximum concentration of  $\sim 3.3$  wt% according to X-ray diffraction (XRD). The nanodiamond-doped silica aerogel contained  $\sim 7.5$  wt% of diamond in the final aerogel. It is suggested that the small size of the nanodiamond particles allowed them to incorporate well in the aerogel network

and not to be washed away during solvent exchange step. Furthermore, aerogel with nanodiamonds increased the surface area compared to the both pure aerogel and microdiamond-doped silica aerogel, possible due to similar size of diamond to silica particles that did not disturb the gelation of silica. Although DNDs are not suitable for solar scattering due to graphitic  $sp^2$  carbon, DNDs were used in order to study the doping of aerogels with diamonds. Additionally, scanning electron microscopy (SEM) and transmission electron microscopy (TEM) were used to observe the porous aerogel formation and doping with diamond particles.

The ultraviolet (UV)/Visible (Vis)/Near infrared (NIR) diffuse reflectance showed that composite microdiamond-doped silica aerogel has an improved reflectance compared to microdiamond powder or pure silica alone. The fall speed was calculated to estimate how long the measured materials would stay in the atmosphere before sedimentation. The obtained results are promising and could stimulate further in-depth studies with similar materials with a potential for applications in solar geoengineering.

## List of publications

- Vukajlovic J, Wang J, Forbes I, Šiller L. *Diamond-doped silica aerogel for solar geoengineering*. *Diamond and Related Materials* 2021,117, 108474.
- Vukajlovic J, Wang J, Han X, Forbes I, Šiller L. *Diamonds in silica aerogel for solar scattering*. In: *International Conference on Aerogels for Biomedical and Environmental Applications*. 2020, Santiago de Compostela, Spain.
- Vukajlovic J, Wang J, Han X, Šiller L. *Diamond-doped silica aerogel for Earth's cooling*. In: *1<sup>st</sup> Conference on Aerogel Inspired Materials*, 2019, Newcastle upon Tyne, UK.
- Vukajlovic J, Wang J, Šiller L. *Influence of environmental conditions on nanodiamond colloidal stability*. In: *70<sup>th</sup> Diamond Conference*. 2019, Coventry, UK.
- Vukajlovic J, Wang J, Šiller L. *Relationship between dilution and agglomeration of nanodiamond colloids under environmental conditions*. In: *9<sup>th</sup> International Colloids Conference*. 2019, Barcelona, Spain.
- Vukajlovic J, Corbyn R, Wang J, Han X, Šiller L. *Nanodiamonds in silica aerogel for solar radiation management*. In: *69<sup>th</sup> Diamond Conference*. 2018, Coventry, UK.
- Vukajlovic J, Šiller L. *HPHT diamonds functionalized with hydrocarbons*. Manuscript in preparation.

## Table of content

List of Figures .....	x
List of Tables .....	xvi
Abbreviation list .....	xvii
<b>Chapter 1 Introduction .....</b>	<b>1</b>
<b>Chapter 2 Literature review .....</b>	<b>5</b>
2.1 Solar geoengineering.....	5
2.1.1 Blackbody radiation .....	7
2.1.2 Geoengineering .....	8
2.1.3 Aerosol properties .....	9
2.1.3.1 Mie particle size for solar aerosols .....	11
2.1.4 Fall speed .....	12
2.1.5 Solar Radiation Management considerations.....	13
2.1.6 Promising aerosol candidates .....	14
2.2 Silica aerogels .....	16
2.2.1 Properties and application.....	16
2.2.2 Optical properties .....	16
2.2.3 Synthesis .....	17
2.2.3.1 Sol-gel process .....	18
2.2.3.2 Aging .....	20
2.2.3.3 Drying.....	21
2.2.4 Comparison of different precursors, solvents and modifiers .....	24
2.2.5 Optical application of the doped silica aerogel.....	29
2.3 Diamonds.....	30
2.3.1 Optical properties of diamond.....	31
2.3.2 Diamond synthesis.....	32

2.3.2.1 High pressure high temperature .....	33
2.3.2.2 Detonation synthesis .....	34
2.3.2.2.1 Purification and functionalization of detonation nanodiamonds .....	36
2.3.2.2.2 De-agglomeration of detonation nanodiamonds .....	36
2.3.2.3 Detonation nanodiamonds and high pressure high temperature diamonds comparison.....	37
2.3.3 Colloids.....	38
<b>Chapter 3 Methodology .....</b>	<b>43</b>
3.1 Materials and methods .....	43
3.1.1 Materials .....	43
3.1.2 Microdiamond functionalization treatment.....	44
3.1.3 Raw microdiamond-doped aerogels .....	44
3.1.4 Nanodiamond colloids.....	47
3.1.5 Nanodiamond-doped aerogels synthesis .....	47
3.2 Interaction of the electron beam with the matter.....	47
3.2.1 Scanning electron microscopy.....	49
3.2.2 Transmission electron microscopy .....	51
3.2.2.1 Selected area electron diffraction .....	53
3.2.2.2 Electron energy loss spectroscopy .....	54
3.3 X-ray diffraction .....	56
3.4 Optical Spectroscopies.....	58
3.4.1 UV/Visible absorption spectroscopy .....	59
3.4.2 UV/Visible/Near-infrared reflectance spectroscopy .....	60
3.4.3 Raman scattering spectroscopy .....	61
3.4.4 Fourier transform infrared spectroscopy .....	64
3.5 Nuclear magnetic resonance spectroscopy .....	66
3.6 Dynamic light scattering.....	69

3.6.1 Zeta potential measurement .....	71
3.7 Brunauer-Emmett-Teller and Barrett-Joyner-Halenda theories.....	72
3.8 Fall speed.....	77
3.9 Conclusion .....	77
<b>Chapter 4 Raw and 1-undecene-treated microdiamonds .....</b>	<b>78</b>
4.1 Scanning electron microscopy of microdiamonds.....	79
4.2 Transmission electron microscopy of microdiamonds .....	80
4.3 Dynamic light scattering of microdiamonds .....	82
4.4 Raman scattering spectroscopy of microdiamonds .....	83
4.5 X-ray diffraction of microdiamonds.....	84
4.6 FTIR spectroscopy of microdiamonds.....	85
4.7 Nuclear magnetic resonance spectroscopy of microdiamonds and 1-undecene solution.	86
4.7.1 Solid-state <sup>1</sup> H NMR data of microdiamonds .....	86
4.7.2 Solid-state <sup>13</sup> C NMR data of microdiamonds .....	88
4.7.3 Solution-state <sup>13</sup> C NMR data of 1-undecene solution.....	90
4.8 Conclusion .....	91
<b>Chapter 5 Diamond-doped silica aerogels.....</b>	<b>93</b>
5.1 Scanning electron microscopy of silica aerogels .....	93
5.2 Transmission electron microscopy of microdiamond-doped silica aerogel .....	95
5.3 FTIR spectroscopy of silica aerogels .....	96
5.4 X-ray diffraction of silica aerogels.....	98
5.5 Brunauer-Emmett-Teller and Barrett-Joyner-Halenda analysis of silica aerogels .....	101
5.6 Density and fall speed of silica aerogels .....	105
5.7 Reflectance of microdiamonds, pure and microdiamond-doped silica aerogel .....	107
5.8 Conclusion .....	109
<b>Chapter 6 Detonation nanodiamonds in silica aerogel .....</b>	<b>111</b>

6.1 Characterization of pure detonation nanodiamonds.....	112
6.1.1 High resolution transmission electron microscopy of nanodiamonds .....	112
6.1.2 Selected area electron diffraction of nanodiamonds.....	113
6.1.3 Electron energy loss spectroscopy of nanodiamonds .....	114
6.2 Agglomeration of nanodiamonds upon dilution with DI water.....	114
6.2.1 UV/Visible absorption of nanodiamonds.....	115
6.2.2 The pH and Zeta potential of nanodiamond colloids .....	116
6.2.3 Dynamic light scattering of nanodiamond colloids .....	118
6.3 Nanodiamond-doped silica aerogel .....	120
6.3.1 High resolution transmission electron microscopy of nanodiamond-doped silica aerogel .....	120
6.3.2 X-ray diffraction of nanodiamond-doped silica aerogel .....	121
6.3.3 Brunauer-Emmett-Teller and Barrett-Joyner-Halenda theories of nanodiamond-doped silica aerogel.....	122
6.3.4 Density of nanodiamond-doped silica aerogel.....	125
6.4 Conclusion.....	126
<b>Chapter 7 Conclusion and future work .....</b>	<b>128</b>
7.1 Summary.....	128
7.2 Future recommendations .....	130
<b>References .....</b>	<b>132</b>

## List of Figures

Figure 2.1: Global warming timeline and significant dates for a fight against it. ....	6
Figure 2.2: a) The Sun's and the Earth's blackbody emissions, image taken from [21], and b) atmospheric absorption bands of ozone, oxygen, water vapour and carbon dioxide, image taken from [29].....	7
Figure 2.3: Possible scenario of light interfering with a particle, image taken from [21].....	9
Figure 2.4: Back and forward scattering, image taken from [21]. ....	10
Figure 2.5: The incident angle is: a) smaller, b) equal, and c) greater than the critical angle, image taken from [31].....	10
Figure 2.6: Total and forward scattering, and absorption for a soot particle, image taken from [21]. ....	12
Figure 2.7: Injection of aerosol in the lower stratosphere (on the mountain top for energy efficacy): artillery, a tower, an airplane and balloons, image taken from [3].....	13
Figure 2.8: Down/up-scattering of diamond is optimal for 0.05-0.7 $\mu\text{m}$ , image taken from [6]. ....	15
Figure 2.9: Hemispherical transmittance and reflectance for silica aerogel, image taken from [39].....	17
Figure 2.10: TEOS-ethanol-water ternary phase diagram, image taken from [41]. ....	19
Figure 2.11: Rate of hydrolysis and condensation against the sol pH, image taken from [41].	20
Figure 2.12: Primary and secondary silica aerogel particles; a) rate of neck growth, and b) rate of Ostwald mechanism, image taken from [12]. ....	21
Figure 2.13: a) Drying of the wet gel and subsequent structures, and b) phase diagram of the drying solvent, image taken from [15]. ....	22
Figure 2.14: Silylation process with trimethylchlorosilane (TMCS), where grey spheres represent silica aerogel particles, image taken from [34].....	23
Figure 2.15: a) and b) Phase separation and surface modification, images taken from [20, 52], respectively, and c) APD with sodium bicarbonate, image taken from [18]. ....	28

Figure 2.16: Diamond and graphite hybridization, image taken from [67].	30
Figure 2.17: Diamond unit cell, image taken from [68].	31
Figure 2.18: Phase diagram: diamond and graphite stability zones, image taken from [64].	33
Figure 2.19: HPHT synthesis: a) HPHT setup, and b) the HPHT cell, image taken from [72].	34
Figure 2.20: Detonation synthesis: a) detonation precursors and nanodiamond product, b) reaction path, and c) the following resulting structure, image taken from [74].	35
Figure 2.21: Detonation nanodiamond structure, image taken from [80].	36
Figure 2.22: Diamond particle surrounded by graphitic carbon, image taken from [96].	40
Figure 3.1: a) pure silica aerogel, b) 500 ppm, c) 700 ppm, and d) 900 ppm raw microdiamond-doped aerogel.	46
Figure 3.2: a) 4 wt% nanodiamond colloid, and b) final nanodiamond-doped silica aerogel.	47
Figure 3.3: Schematic representation of the, a) interaction of the incident beam with a sample, image taken from [105], and b) closer look at atomic level scattering and photon emission upon absorption of the incident beam, image taken from [106].	48
Figure 3.4: Schematic representation of SEM instrument, image taken from [108].	50
Figure 3.5: The difference in kinetic energy, as well as number distribution, between secondary and backscattered electrons, image taken from [107].	51
Figure 3.6: The transmission electron microscope, image taken from [110].	53
Figure 3.7: Formation of a diffraction pattern on a recording plane, image taken from [107].	54
Figure 3.8: a) three EELS ranges for barium, yttrium, oxygen and copper, image taken from [107], and b) core shells, image taken from [112].	55
Figure 3.9: Graphite and diamond electronic structures, with bonding and antibonding orbitals, image taken from [113].	56
Figure 3.10: a) Cu X-ray formation, and b) Cu X-ray emission spectrum, image taken from [111].	57
Figure 3.11: X-ray tube, image taken from [111].	58

Figure 3.12: Schematic representation of a goniometer, image taken from [114].	58
Figure 3.13: Spectrophotometer design, image taken from [116].	59
Figure 3.14: Typical UV/Vis dispersive spectrophotometer, image taken from [117].	60
Figure 3.15: Diffuse reflection with integrating sphere: a) without, and b) with specular reflection, image taken from [119].	61
Figure 3.16: Raman scattering, image taken from [121].	63
Figure 3.17: Typical Raman spectrometer, image taken from [117].	64
Figure 3.18: Schematic representation of FTIR spectrometer, image taken from [123].	65
Figure 3.19: ATR crystal with evanescent wave, penetration depth, $d_p$ , and critical angle $\theta$ , image taken from [125].	66
Figure 3.20: Schematic representation of an NMR spectrometer, image taken from [115].	68
Figure 3.21: The correlation function for small and large particles, image taken from [126].	70
Figure 3.22: Schematic representation of Zetasizer, image taken from [126].	71
Figure 3.23: Folded capillary cell used for Zeta potential measurement, image taken from [126].	71
Figure 3.24: Signal generation, image taken from [126].	72
Figure 3.25: a) Six types of adsorption isotherms, b) surface area measurement range, and c) hysteresis loop types, image taken from [134].	74
Figure 3.26: BET plot.	75
Figure 3.27: Relationship between the pore and the capillary radius, image taken from [136].	76
Figure 4.1: SEM image of raw microdiamond powder with scale bar: a) 5 $\mu\text{m}$ , and b) 1 $\mu\text{m}$ .	79
Figure 4.2: SEM image of 1-undecene-treated microdiamond powder with scale bar: a) 5 $\mu\text{m}$ , and b) 1 $\mu\text{m}$ .	80
Figure 4.3: TEM image of raw microdiamond particles with scale bar: a) 2 $\mu\text{m}$ , b) 500 nm, and c) 500 nm.	81

Figure 4.4: TEM image of 1-undecene-treated microdiamond particles with scale bar: a) 2 $\mu\text{m}$ , b) 500 nm, and c) 500 nm. ....	82
Figure 4.5: The DLS particles size distribution of raw diamond (black) and 1-undecene-treated diamond (red). ....	83
Figure 4.6: Raman spectrum of raw (black) and 1-undecene-treated microdiamond (red). ....	84
Figure 4.7: XRD patterns of raw (black) and 1-undecene-treated microdiamond (red). ....	85
Figure 4.8: The FTIR of raw (black) and 1-undecene-treated microdiamond powder (red). ....	86
Figure 4.9: Solid-state $^1\text{H}$ NMR spectrum of raw microdiamond. ....	87
Figure 4.10: Solid-state $^1\text{H}$ NMR spectrum of 1-undecene-treated microdiamond. ....	87
Figure 4.11: Solid-state $^{13}\text{C}$ NMR CP-MAS spectrum of raw microdiamond. ....	88
Figure 4.12: Solid-state $^{13}\text{C}$ NMR MAS spectrum of raw microdiamond. ....	89
Figure 4.13: Solid-state $^{13}\text{C}$ NMR CP-MAS (green) and MAS (red) spectra of 1-undecene-treated microdiamond. ....	90
Figure 4.14: Solution-state $^{13}\text{C}$ NMR spectrum of pure 1-undecene. ....	91
Figure 5.1: SEM image of silica aerogel (fine powder) with scale bar 10 $\mu\text{m}$ . ....	94
Figure 5.2: SEM image of pure silica aerogel with scale bar: a) 500 nm, and b) 200 nm. ....	94
Figure 5.3: TEM image of pure silica aerogel with scale bar: a) 500 nm, and b) 200 nm. ....	95
Figure 5.4: TEM image of 900 ppm raw-microdiamond/silica aerogel with scale bar: a) 500 nm, and b) 200 nm. ....	96
Figure 5.5: FTIR spectra of: a) pure, b) 500 ppm microdiamonds/silica, c) 700 ppm microdiamonds/silica, and d) 900 ppm microdiamonds/silica aerogel. ....	97
Figure 5.6: A representative FTIR spectrum of a silica aerogel. ....	97
Figure 5.7: XRD patterns of: a) pure, b) 500 ppm microdiamonds/silica, c) 700 ppm microdiamonds/silica, and d) 900 ppm microdiamonds/silica aerogel. ....	98
Figure 5.8: A representative XRD pattern of: a) pure, and b) diamond-doped silica aerogel. ....	99

Figure 5.9: Plot of concentration of diamond in the precursor sol (ppm) Vs amount of diamond in the final silica aerogel (wt%) for 500, 700 and 900 ppm microdiamonds/silica aerogels. .	100
Figure 5.10: The nitrogen adsorption-desorption isotherm and the pore size distribution of the 0.5 ml catalyst pure silica aerogel (as insert).....	101
Figure 5.11: The nitrogen adsorption-desorption isotherm and the pore size distribution of the 500 ppm raw microdiamond-doped silica aerogel (as insert). .....	102
Figure 5.12: The nitrogen adsorption-desorption isotherm and the pore size distribution of the 0.6 ml catalyst pure silica aerogel (as insert).....	102
Figure 5.13: The nitrogen adsorption-desorption isotherm and the pore size distribution of the 700 ppm raw microdiamond-doped silica aerogel (as insert). .....	103
Figure 5.14: The nitrogen adsorption-desorption isotherm and the pore size distribution of the 900 ppm raw microdiamond-doped silica aerogel (as insert). .....	103
Figure 5.15: a) BET surface area Vs concentration of diamond in the precursor sol, and b) BET surface area Vs amount of diamond in the final aerogel, for pure (0.5 ml catalyst), pure (0.6 ml catalyst), 500, 700 and 900 ppm microdiamond-doped silica aerogels. ....	105
Figure 5.16: a) Average pore diameter Vs concentration of diamond in the precursor sol, and b) Average pore diameter Vs amount of diamond in the final aerogel, for pure (0.5 ml catalyst), pure (0.6 ml catalyst), 500, 700 and 900 ppm microdiamond-doped silica aerogels. ....	105
Figure 5.17: Reflectance spectra of: a) glass slide only, b) pure aerogel, c) raw microdiamond, and d) 900 ppm raw microdiamond-doped silica aerogel.....	109
Figure 6.1: HRTEM images of nanodiamonds circled in red with scale bar: a) 20 nm, b) 10 nm, c) 5 nm, and d) 2 nm.....	113
Figure 6.2: The SAED pattern of nanodiamonds with Miller indices (111), (220), (311). .....	114
Figure 6.3: The EELS spectrum of carbon K-edge excitation of nanodiamond.....	114
Figure 6.4: UV/Vis absorption of the nanodiamond colloids at different concentrations.....	116
Figure 6.5: pH and Zeta potential of the original (4 wt%) and 1 wt% nanodiamond colloid. .	117
Figure 6.6: a) DLS average particle size, and b) DLS size distribution for original (4 wt%) and diluted (1 wt%) nanodiamond colloids on day 1 and 6. ....	119

Figure 6.7: HRTEM image of nanodiamond-doped silica aerogel with scale bar: a) 20 nm, and b) 5 nm with nanodiamonds labelled in red. ....	121
Figure 6.8: XRD patterns of pure silica aerogel (black) and nanodiamond-doped silica aerogel (red). ....	122
Figure 6.9: The nitrogen adsorption-desorption isotherm of pure silica aerogel with pore size distribution (as insert).....	123
Figure 6.10: The nitrogen adsorption-desorption isotherm of nanodiamond-silica aerogel with pore size distribution (as insert). ....	124
Figure 6.11: BET surface area and bulk density of pure, micro- and nanodiamond-doped silica aerogels discussed in Chapter 5 and 6.....	126

## List of Tables

Table 2.1: Potential aerosols and their proposed optimal radius based on their refractive indices, and densities [8]. .....	15
Table 2.2: Most common silica aerogel precursors and the final aerogel properties .....	26
Table 2.3: Comparison of HPHT and DND particles. ....	38
Table 3.1: Pure and microdiamond-doped silica aerogels with diamond concentration in the precursor and amount of catalyst used to obtain the gel. ....	46
Table 5.1: Comparison between concentration of diamond in the precursor sol (ppm) and amount of diamond in the final silica aerogel (%). ....	100
Table 5.2: Relationship between with XRD percentage of diamond in silica aerogels and BET surface area, pore specific volume, average pore diameter and porosity. ....	104
Table 5.3: Relationship between with XRD percentage of diamond in silica aerogels and skeletal, bulk density and porosity. ....	106
Table 5.4: Average fall speed and time accordingly for raw microdiamond, pure silica and raw microdiamond-doped silica aerogel according to equation 2.5. ....	107
Table 6.1: DLS particle size of the original (4 %) and 1 % colloid. ....	119
Table 6.2: Relationship between with XRD percentage of nanodiamonds in silica aerogel and BET surface area, pore specific volume, average pore diameter and porosity. ....	124
Table 6.3: Relationship between XRD percentage of nanodiamonds in silica aerogel and their skeletal and bulk density, and porosity. ....	125

## Abbreviation list

APD	Ambient pressure drying
ATR	Attenuated total reflectance
BASD	Bead-assisted sonic disintegration
BET	Brunauer-Emmett-Teller
BJH	Barrett-Joyner-Halenda
BSE	Backscattered electrons
CCD	Charge-coupled device
CDCl <sub>3</sub>	Deuterated chloroform
CDR	Carbon dioxide removal
COLD	Low-temperature supercritical drying
CVD	Chemical vapour deposition
DI	Deionized water
DMDMS	Dimethyldimethoxysilane
DLS	Dynamic light scattering
DND	Detonation nanodiamond
EELS	Electron energy loss spectroscopy
FCC	Face-centred cubic
FEG	Field emission gun
FTIR	Fourier transform infrared
GHG	Greenhouse gasses
HMDSO	Hexamethyldisiloxane
HMDZ	Hexamethyldisilazane
HOT	High-temperature supercritical drying

HPHT	High pressure high temperature
HRTEM	High resolution transmission electron microscopy
IPA	Isopropanol
IPCC	Intergovernmental Panel on Climate Change
IR	Infrared
LST	Low surface tension
MTES	Methyltriethoxysilane
MTMS	Methyltrimethoxysilane
NDC	National determined contribution
NiNPs	Nickel nanoparticles
NIR	Near infrared
NMR	Nuclear magnetic resonance
NV	Nitrogen-vacancy
NVN	Nitrogen-vacancy-nitrogen
PDA	Photo diode array
PEDS	Polyethoxydisiloxane
PMT	Photomultiplier tube
PM <sub>2.5</sub>	Particulate matter with particles smaller than 2.5 microns
RDX	1,3,5-trinitroperhydro-1,3,5-triazine
SAED	Selected area electron diffraction
SAUD	Salt-assisted ultrasonic de-aggregation
SCD	Supercritical drying
SCoPEX	Stratospheric Controlled Perturbation Experiment
SE	Secondary electrons

SEM	Scanning electron microscopy
SRM	Solar radiation management
SSA	Single scatter albedo
TEM	Transmission electron microscopy
TEOS	Tetraethoxysilane
TMCS	Trimethylchlorosilane
TMOS	Tetramethoxysilane
TMS	Trimethylsilanol
TNT	2-methyl-1,3,5-trinitrobenzene
TPOS	Tetrapropoxysilane
UNFCC	United Nations Framework Convention on Climate Change
UV	Ultraviolet
Vis	Visible
WG	Waterglass
XRD	X-ray diffraction



## Chapter 1 Introduction

Geoengineering has emerged as a tool to mitigate global warming by either direct carbon dioxide removal or solar radiation management (SRM) [1]. Mount Pinatubo (Philippines) erupted in 1991 releasing sulfur dioxide in the atmosphere. From there, sulfate aerosols as  $\text{H}_2\text{O}-\text{H}_2\text{SO}_4$  droplets were formed, which scattered solar radiation from the Earth. Following the volcanic eruption, a short-lived reduction in global temperature of  $\sim 0.5$  K was observed in 1992, only for the temperature to return to the value prior to the eruption in 1995. [2]. Although the cooling effect was recorded shortly after the volcanic event, long-term risks of such sulfate aerosols remain. As a consequence of a high aerosol concentration, large particles form by condensation, decreasing the effectiveness of the aerosol [3] and shortening the aerosol life-time due to faster settling [4]. In addition, such aerosols can cause acid rain, catalyse the degradation of ozone, and result in a decrease in solar panel productivity [3]. Nevertheless, the cooling effect of sulfate aerosols has inspired the aerosol injection technique to become one of the most prosperous SRM methods due to its cost-effectiveness and potential rapid deployment [5].

Titania (anatase and rutile phase), silicon carbide, diamond, alumina, silica, zirconia, calcite, soot, and sulfuric acid were previously proposed to be used as geoengineering aerosols and were included in various theoretical models [6-8]. Keutsch's group from Harvard University has launched Stratospheric Controlled Perturbation Experiment (SCoPEX) using calcite ( $\text{CaCO}_3$ ) to study the effect of these aerosols on the atmosphere [9, 10]. High refractive index aerosols are believed to significantly improve up-scattering, and in case of diamond particles between  $0.05-0.7 \mu\text{m}$  are predicted to be the most efficient [6].

Although both silica and diamond have been proposed for geoengineering aerosols with intention to reflect light and subsequently reduce heating, they have never been combined or compared. The novel composite could benefit from the good properties of individual materials. Diamond has exceptional properties such as a high refractive index ( $n=2.41$  [6]), absorbs minimally in the IR, and it is non-toxic (biocompatible) [11]. It is thus believed that it might outperform other proposed aerosol materials. Silica aerogel is ultra-porous, light, transparent, low cost and non-toxic [12]. Silica aerogels have recently been proposed to be used in space engineering because they strongly attenuate harmful UVA and UVB radiation (280-400 nm) [13] and another study showed that it does not degrade under UV exposure

[14]. Additionally, silica was determined to be suitable for doping with various nanoparticles, where the nanoparticle optical properties are sustained in the final doped aerogel [15]. The composite structures made of silica aerogels with different carbon nanostructures in the form of nanotubes, nanofibers, and graphene have also been developed [16]. In addition, PM<sub>2.5</sub> aerosols (particles smaller than 2.5 μm) are considered harmful for humans during respiration. Nevertheless, it is suggested that the aerosol particles should be within a size range of ~ 0.1-1 μm in order to minimise health risks [17].

The silica aerogel powders can be now produced on a large scale by low cost at ambient pressure drying processing, due to usage of low cost solvents [18-20]. In addition, diamond powders (prepared by HPHT and detonation synthesis) can be purchased in ton quantities, at low cost. In addition, diamond-silica composite materials, with ultra-light weight (due to low density) are expected to stay longer in the stratosphere than pure diamonds before settling down to the troposphere and the Earth's surface (see further discussion in the thesis), and by using diamond particles smaller than 100 nm as dopants this material could also ensure that the overall particle range is within 0.1-1 μm range.

A well-known fact is that the blackbody radiation emission from Sun and Earth peaks in the UV/Vis and IR range of the electromagnetic spectrum, respectively [21]. The solar aerosols therefore enable cooling by scattering of the sunlight in the shortwave and transmission of the Earth's radiation in the longwave spectrum range. The idea guiding this concept is that silica aerogel would serve as a host and act as lower-cost scatterer, while diamond dopant would be a highly efficient up-scatterer with improving the IR transmittance. The main line of study presented in this thesis is doping of silica aerogel with nano- and microdiamond particles. Additionally, different applications of microdiamond particles and nanodiamond colloids are explored as well in this thesis.

The research hypotheses that have been investigated in this thesis are:

- 1) Shaking treatment of HPHT microdiamonds in 1-undecene and isopropanol with zirconia beads leads to functionalization of microdiamonds particles with alkyl groups
- 2) Stability of detonation nanodiamonds in a colloid decreases with dilution and upon exposure to ambient air and particles agglomerate

- 3) Silica aerogel can be successfully doped with nano- and microdiamonds, where nanodiamonds can be incorporated in final silica aerogel with higher content
- 4) Achieving low bulk density and high surface area of the nano- and microdiamond-doped silica aerogels
- 5) Improved reflectance of microdiamond-doped silica aerogel in the UV/Vis/NIR wavelength range compared to the pure microdiamond powder or pristine silica aerogel alone

The objectives of this thesis are:

- 1) Shaking of HPHT microdiamonds in 1-undecene and isopropanol with zirconia beads and characterization of raw and treated microdiamonds, including nuclear magnetic resonance (NMR) spectroscopy to observe the surface groups on diamond particles
- 2) Zeta potential-pH and DLS size distribution measurements of original 4 wt% and diluted 1 wt% nanodiamond colloid up to 6 days in order to evaluate the colloid stability
- 3) Doping of the silica aerogels with nano- and microdiamonds and evaluation of aerogel properties, including BET surface area, XRD, and SEM and TEM imaging
- 4) Evaluation of fall speed and density of the microdiamond-doped silica aerogel
- 5) Optical measurements of the prepared diamond/silica aerogel composite

This thesis contains seven chapters and the structure is presented below.

Literature review is presented in Chapter 2, where the relevant terms of solar geoengineering, as well as the main properties of diamond and silica aerogel material are shown.

Chapter 3 shows experimental procedures and principles of characterization techniques with measurement conditions used for our samples.

Chapter 4 presents the functionalization treatment of HPHT microdiamonds with 1-undecene, with characterization techniques that look at the diamond particle size and shape, and surface before and after the treatment. Alkyl groups attached on the particle surface has been reported to tune the decay time of fluorescent particles [22].

Raw microdiamonds discussed in Chapter 4 are added to the silica aerogel before gelation in different concentrations and the data are shown in Chapter 5. The properties of the doped

aerogels are compared to the pure silica aerogel. Finally, the optical properties of the pure microdiamonds, silica aerogel and microdiamond-doped silica aerogel are presented.

Chapter 6 shows the characterization of detonation nanodiamonds that form the nanodiamond colloid with positive zeta potential. Also, the comparison between 4 wt% (the original and denoted as a stable nanodiamond colloid by the supplier-NanoCarbon Institute, Japan) and 1 wt% (the diluted) colloid in terms of zeta potential, pH and DLS particle size over a period of 6 days is presented. It has been previously reported [23] that these nanodiamond colloids (from NanoCarbon Institute, Japan) agglomerate upon dilution which is contra intuitive. The aim of the Chapter 6 is to try to explain the reason for agglomeration of nanodiamonds upon dilution, including the study over a period of time, that has not yet been reported. Furthermore, silica aerogel doped with detonation nanodiamonds and properties of the doped aerogel are discussed in this chapter.

The most important results obtained in this work, as well as the future work such as recommendations for improvement of the diamond/silica aerogel composite are presented in Chapter 7.

## Chapter 2 Literature review

*This chapter presents theory behind solar geoengineering and provides literature review of the solar aerosols, silica aerogel and diamond, and discusses the reason for choosing a diamond-silica aerogel composite material for this PhD project. Firstly, some relevant terms from the geoengineering theory were shown, after which a closer look at the desired properties of a solar aerosols was provided. The current state of art of solar aerosol materials was reviewed. Diamond and silica aerogel main characteristics were briefly given with the emphasis on optical properties for the solar aerosol application. Furthermore, potential optical application for diamond in silica aerogels in the future were shown. Additionally, properties of nanodiamond colloids and their application in device fabrication were discussed.*

### 2.1 Solar geoengineering

Human activities on the Earth have led to global warming caused by growth of human population and economies [24]. A global shift in which extreme warm periods are occurring much more frequently than cold periods for most of the planet can be observed. Significant changes in precipitation patterns can also be seen, resulting in an increased occurrence of flooding, droughts, wildfires, as well as rising sea levels, due to the melting of ice within polar regions [25]. Common air pollutants are greenhouse gasses (GHG) (carbon dioxide (CO<sub>2</sub>), methane (CH<sub>4</sub>), nitrous oxide (N<sub>2</sub>O)), black and brown carbon [26].

Some serious actions to mitigate global warming date back to 1990s (see Figure 2.1). *The Intergovernmental Panel on Climate Change (IPCC)* was founded in 1988 with the aim to give scientific insight into climate change. Since then countries have been trying to cope with global warming through agreements to cut the air pollution, enhancement of research in this field, etc. *The 1st IPCC report* was published in 1990 [25]. After that, the *United Nations Framework Convention on Climate Change (UNFCCC)* was established in Rio de Janeiro in 1992 [3]. Under this body, *Kyoto (2005) and Paris (2015) accords* were established. *The 5th IPCC report* in 2014 published that humans have been responsible for global warming with 95 % certainty [3].

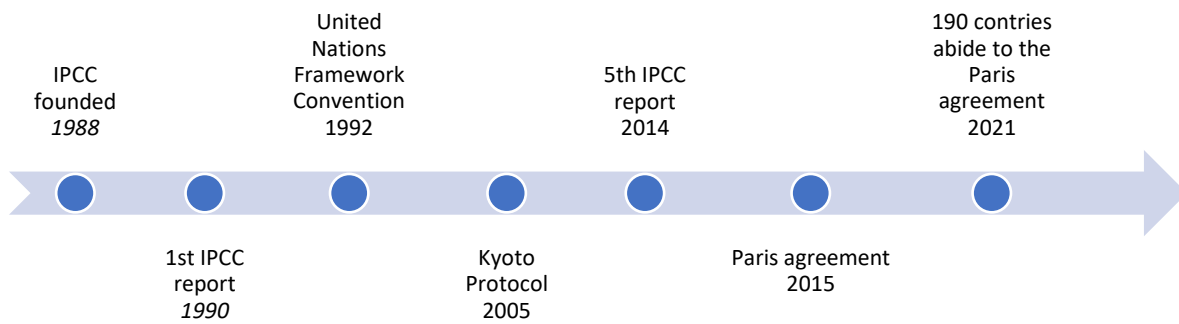


*Figure 2.1: Global warming timeline and significant dates for a fight against it.*

The Kyoto Protocol was announced in 1997 [24], but only ratified in 2005 with 192 parties involved. It is legally binding for developed countries, but some big parties such as the US never ratified this. By signing this, countries are obliged to commit to the emission target established by the accord that can be traded among the countries. The Paris agreement [24] is more flexible than Kyoto and extends to all countries (197) in the world including developing countries and no penalties are enforced. In the most optimistic scenario models suggest that the damage, however, cannot be suddenly reversed [27].

Paris aims to prevent the global average temperature rise above 2 °C above pre-industrial level, although trying to halt it to 1.5 °C. Also, the Paris agreement allows all countries to set they own emission goal known as national determined contribution (NDC) and report every five years, contrary to the Kyoto Protocol, where no clear timeline was set. Furthermore, the beforementioned agreements not only aim to reduce the amount of greenhouse gases emitted, but also support the efforts towards sustainable and clean development for each county [28].

In practice, following the protocols is not straight forward due to the concern that they would weaken the economies of many countries. For instance, the US declared to have an intention of leaving the Paris agreement 2017 [24], while in 2021 Biden’s administration announced to recommit to the Paris accord. As for the leading polluters, only Iran, Iraq and Turkey have not ratified the Paris agreement, with Turkey being the last G20 country not to have done it, while Russia officially joined it in 2019. To date only 7 countries out of 197 have not signed the accord [28].

### 2.1.1 Blackbody radiation

A true blackbody absorbs all incident radiation, without reflecting any of it. It also emits energy with the maximum intensity dependent on temperature. The Sun and the Earth are near-perfect blackbodies. The temperature at the Sun's surface is about 5800 K and hence it emits in the UV, Vis and IR electromagnetic energy range (see Figure 2.2a). The Earth's average temperature at the surface is about 288 K, and therefore, the outgoing radiation is thermal-IR ( $> 2.5 \mu\text{m}$ ). The Sun being the hotter and larger body emits more energy than the Earth and its emission peaks at shorter wavelengths. In other words, the radiation from the Sun that reaches the Earth is mostly made up of UV, Vis and solar-IR ( $0.75\text{--}2.5 \mu\text{m}$ ) radiation and the radiation that is coming back from its surface is mostly thermal-IR [21]. Figure 2.2b shows attenuation of the sunlight as it passes through the Earth's atmosphere due to absorption from ozone, oxygen and nitrogen gas (in the UV below  $0.28 \mu\text{m}$ ) and water vapour and carbon dioxide (in the solar-IR). Visible light is mostly transmitted and it reaches the sea level.

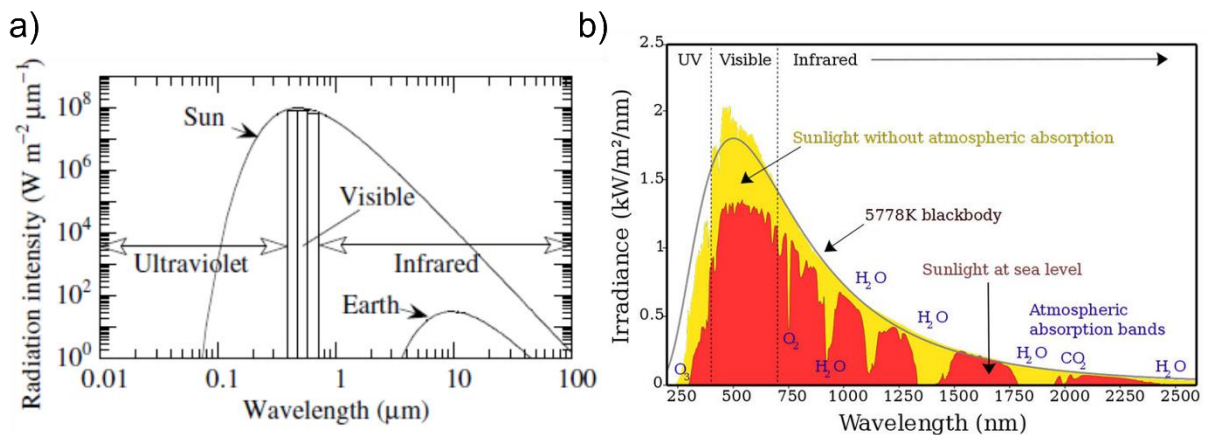


Figure 2.2: a) The Sun's and the Earth's blackbody emissions, image taken from [21], and b) atmospheric absorption bands of ozone, oxygen, water vapour and carbon dioxide, image taken from [29].

Near UV radiation from the Sun contains UV-A, UV-B and UV-C radiation. Unlike UV-A ( $0.32\text{--}0.38 \mu\text{m}$ ) and UV-B ( $0.29\text{--}0.32 \mu\text{m}$ ) energy, which is responsible for tanning or cause sunburn, respectively, UV-C ( $0.25\text{--}0.29 \mu\text{m}$ ) is far more dangerous to life on Earth. Ozone absorbs in the parts of UV-C and UV-B in the stratosphere, from  $0.17$  to  $0.35 \mu\text{m}$ , preventing it to harm the life on Earth. Ozone destruction has a devastating effect on species inhabiting the Earth, allowing more of the harmful radiation to pass through [21].

The balance between the fraction of light that comes in (heating) and that is reflected back (cooling) is known as radiative balance. Radiative forcing occurs when that balance is disturbed [26]. Albedo or reflectance is the ratio of total reflected radiation to total incoming radiation to the Earth [7]. Therefore, the increase in albedo means a decrease in temperature [26].

### *2.1.2 Geoengineering*

Geoengineering includes carbon dioxide removal (CDR) and SRM. The proposed methods should be effective, affordable, quick to develop, and human and environmentally safe. CDR directly removes carbon dioxide from the atmosphere by afforestation, in situ silicate carbonation, CO<sub>2</sub> scrubbers, and fertilization of the ocean [27], while SRM reduces the amount of incoming solar radiation to the Earth's surface: space-reflectors (or sunshades), aerosol injection, surface and cloud albedo enhancement [27]. Notwithstanding their potential, more research is needed in order to evaluate all the plausible effects that aerosol might have on the stratosphere chemistry [3]. It is suggested that aerosol geoengineering has great potential to become the most cost-effective method of all SRM approaches, as well as having the fastest deployment [5]. Budyko first proposed this approach with the use of sulfate aerosols in order to mitigate climate change [30]. Moreover, Crutzen states that geoengineering should be employed in order to buy the humankind some time until it is figured out how to fully eliminate greenhouse gases in case the positive effects overcome the negative side effects [4].

Mount Pinatubo (the Philippines) erupted in 1992 releasing sulfur dioxide in the atmosphere. Sulphuric acid is formed by oxidation of sulphur dioxide. From there, sulfate aerosols as H<sub>2</sub>O-H<sub>2</sub>SO<sub>4</sub> droplets are formed, which scatter the light back from the Earth's surface. The idea of injecting aerosols in order to decrease the global temperature comes from this event [27]. Following the volcanic eruption, the decrease in the global temperature of ~ 0.5 K was observed, but only for a short term. The Earth's temperature returned to the value before eruption in 1995 [2]. The reason behind this is also the biggest disadvantage of sulfate aerosols. Namely, these aerosols absorb IR light and compensate for the initial cooling. Also, with high aerosols concentration large particles are formed by condensation, decreasing the aerosol effectiveness, as well as causing acid rain and catalysing ozone destruction [3].

### 2.1.3 Aerosol properties

Atmospheric aerosols are various atmospheric particles that are in the range from 2 nm to 10  $\mu\text{m}$ . Due to their size, they can stay in the atmosphere for a long time and travel long distances, taking part in many chemical reactions and lastly may influence human health, climate and environment on the Earth [5]. They are typically in either solid or liquid phase. Their origin might be either natural or anthropogenic, while their presence in the atmosphere may occur directly (primary emissions or particles) or their formation may arise from chemical and physical reactions of emitted gases in the atmosphere (secondary emissions). An example of primary particles are sea salt and dust particles, while sulfate aerosols obtained by  $\text{SO}_2$  oxidation are an example of secondary particles [5].

Figure 2.3 shows various possible scenarios that could occur when light reaches the particle such as a diamond particle. Light absorption is not considered here and will be taken into an account for when the scattering efficiency of an aerosol is discussed (see Chapter 2.1.3.1). The light can be either reflected, refracted or diffracted from the particle. The ray labelled 'A' represents reflection of light off the surface of the particle. Ray 'B' is refracted upon entry to the particle, and then again when it leaves. Ray 'C' is diffracted off the surface of the particle. Ray 'D' is firstly refracted upon entry to the particle, followed by double internal reflection and finally refracted when it leaves the particle, while ray 'E' covers the similar path via single internal reflection. The light is mostly scattered forwards, and the rest of the light is scattered sideways and backwards [21].

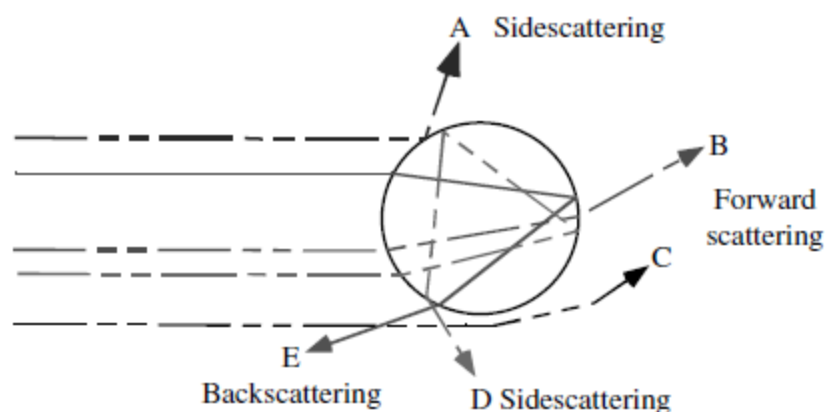


Figure 2.3: Possible scenario of light interfering with a particle, image taken from [21].

Single internal reflection gives rise to light being scattered in the backward direction (see Figure 2.4) which is E-ray in the Figure 2.3. The forward scattering occurs when light is

diffracted or double refracted. From the stratospheric aerosol point of view backscattering is equivalent to the upward scattering. For the current work, backscattering is of interest because it reduces the amount of light from the Sun to heat up the Earth [21].

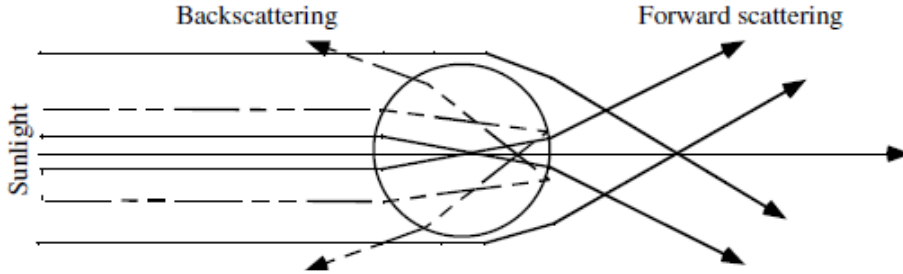


Figure 2.4: Back and forward scattering, image taken from [21].

According to the Snell's law:

$$n_1 \sin \theta_1 = n_2 \sin \theta_2 \quad (2.1)$$

where  $n_1$  and  $n_2$  are refractive indices of two mediums and  $\theta_1$  and  $\theta_2$  are angles of incidence and refraction, respectively. From Figure 2.5, if  $n_1 > n_2$ , then  $\theta_1 < \theta_2$  according to the equation 2.1.

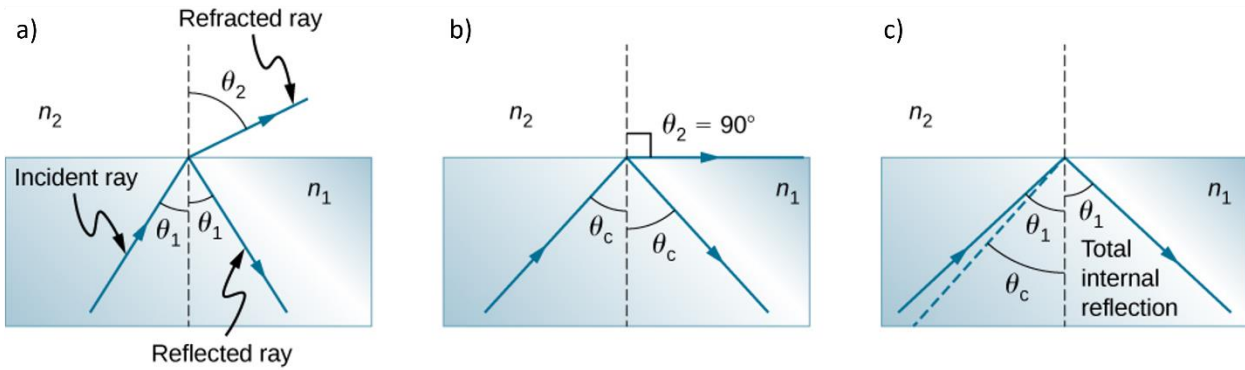


Figure 2.5: The incident angle is: a) smaller, b) equal, and c) greater than the critical angle, image taken from [31].

The use of diamond aerosols in the atmosphere for light scattering is studied in this work. That means that diamond is surrounded with air, which has a lower index of refraction than diamond. A critical angle above which total internal reflection will occur can be defined as:

$$\theta_{1,c} = \sin^{-1} \left( \frac{n_2}{n_1} \sin 90^\circ \right) \quad (2.2)$$

where  $\theta_{1,c}$  is a critical angle of a ray exiting the diamond particle,  $n_1$  and  $n_2$  are refractive indices of diamond and air (atmosphere) ( $n_1 > n_2$ ), respectively. In case  $\theta_1$  is equal or greater than  $\theta_{1,c}$  internal reflection take place. Namely, in order for internal reflection to occur,  $\theta_2$  must be equal or greater than  $90^\circ$ .

### 2.1.3.1 Mie particle size for solar aerosols

Light scattering from aerosols (majority of them) follow Mie theory, because they are similar in size to the incoming light wavelength. It is possible to calculate the scattering from a single particle (single scatter albedo, *SSA*) knowing the complex refractive index for a spherical particle is [5]:

$$m_\lambda = n_\lambda - ik_\lambda \quad (2.3)$$

where  $n_\lambda$  and  $k_\lambda$  are the real and imaginary indices of refraction ( $k_\lambda$  which is used to calculate the absorption extinction coefficient).

Also:

$$SSA = \frac{Q_s}{Q_s + Q_a} \quad (2.4)$$

where  $Q_s$  is the total scattering and  $Q_a$  is the absorption efficiency of the aerosol. The critical *SSA* value is  $\sim 0.85-0.9$  and it is dependent on the surface reflectance of the aerosol. Below that value, aerosols will mostly absorb the light resulting in the net positive radiative forcing, while above that value, aerosols will cause net negative radiative forcing. For  $SSA = 1$ , aerosols scatter all the incident light [5].

Total scattering,  $Q_s$ , equals forward scattering,  $Q_f$ , and backward scattering,  $Q_b$ , with  $Q_b$  being of interest for aerosol engineering. A soot particle which mainly consists of carbon black is taken for an example of backward scattering and its relationship to wavelength of the sunlight and a particle diameter (see Figure 2.6). In this case  $n_\lambda$  of a soot particle is 1.94, while  $k_\lambda$  is 0.66. The shown incident wavelength is 500 nm, and scattering efficiency can be calculating for any other wavelength,  $\lambda_1$ , and particle size,  $d_1$ . Namely, when  $d = 0.5 \mu m d_1/\lambda_1$  is calculated, it allows to read the scattering at the value  $d$  of the diameter on the diagram. Smaller particles follow the Rayleigh scattering regime ( $< 10$  nm in size), while particles in the range between 10 nm to 10  $\mu m$  scatter according to the Mie theory, both scattering and reflecting the highest amount of radiation. Also, particles larger than 10  $\mu m$  abide by the

geometric regime of scattering, achieving a scattering plateau. The most intense scattering and the difference between  $Q_s$  and  $Q_f$  is the highest for a particle size of about 500 nm. In case the radiation wavelength and the particle size are similar values, the most efficient scattering is enabled. It can be also noticed that the soot particle significantly absorbs and therefore the scattering efficiency is lowered. This shows that a desired solar aerosol should have a size of  $\sim 500$  nm, given that the maximum solar radiation is at  $\sim 500$  nm, and should not absorb the incoming light [21].

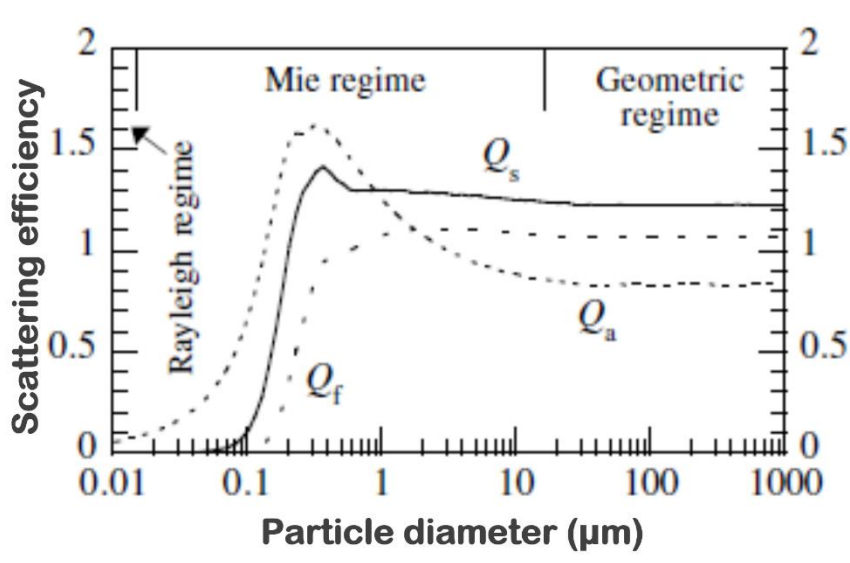


Figure 2.6: Total and forward scattering, and absorption for a soot particle, image taken from [21].

#### 2.1.4 Fall speed

In solar aerosol engineering, not only the value of reflectance, but also the time that aerosols would spend in the atmosphere before sedimentation, plays an important role in the cost-efficacy of the injected aerosols. Therefore, the fall speed, as a function of both particle radius and particle density, should be taken into account when calculating the fall time.

The formula for the fall speed,  $v$  is [21]:

$$v = \frac{2r^2(\rho_p - \rho_a)g}{9\eta_a} G \quad (2.5)$$

where parameters are as follows:  $r$  particle radius,  $\rho_p$  density of a particle,  $\rho_a$  density of air,  $g$  gravitational acceleration,  $\eta_a$  dynamic viscosity of air,  $G$  the dimensionless Cunningham slip correction.

### *2.1.5 Solar Radiation Management considerations*

The troposphere and stratosphere are the first and second of the Earth's atmospheric layers, respectively. The stratospheric and tropospheric circulations are different in nature so that horizontal (poleward) circulation without precipitations is typical for stratosphere, while on the other hand, troposphere has vertical motion with mixing and rain. Hence, the removal of the particles from the stratosphere occurs by settling down caused by gravitation such that larger particles fall faster (are removed faster) in the next atmospheric layer-troposphere where particles are finally removed within a week time from the atmosphere. Owing to the motion in the stratosphere, clouds can survive a couple of years up in the stratosphere in case of volcanic eruptions in the tropics, and for several months when eruption happen at higher latitudes [3].

It can be concluded that the aerosol injection should occur in the Tropics, above the tropopause (the boundary the troposphere and the stratosphere). The tropopause is the layer at ~ 18 km in the Tropics, so it would be optimal to inject the aerosols at ~ 20 km above the Earth [3]. Different means of injection are proposed such as: balloons, airplanes, artillery and towers (see Figure 2.7). It is suggested that balloons are the cheapest option [3].

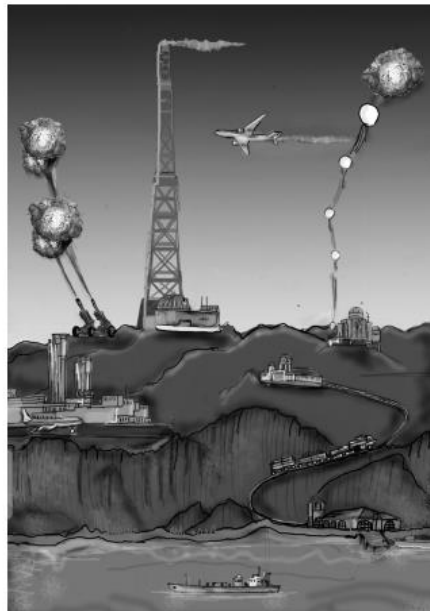


*Figure 2.7: Injection of aerosol in the lower stratosphere (on the mountain top for energy efficacy): artillery, a tower, an airplane and balloons, image taken from [3].*

### *2.1.6 Promising aerosol candidates*

A material that can be used as an engineering aerosol should have high refractive index that would give rise to effective up-scattering [6]. The ideal refractive index is calculated to be 2.96 with an optimal particle radius of 70 nm [7]. Absence of IR absorption is very important since IR absorption would lead to warming and compensate for the cooling effect by up-scattering. Also, a good candidate for this application should be a material with low density in order to not fall to the Earth quickly, not toxic to the environment and life on Earth and that large-scale production can be obtained [6]. Materials other than sulfate aerosols, such as solid aerosols, would scatter incoming radiation more efficiently (per unit mass) due to greater refractive indices than sulfate aerosols, and high refractive index would lead to less forward scattering [7, 32]. It is suggested that reactions involved in ozone depletion, are promoted by water or ice. Absence of water on aerosol surfaces can significantly slow down these reactions, indicating that hydrophobic aerosols are preferred for solar engineering [7].

Titania (anatase and rutile phase), silicon carbide, diamond, alumina, zirconia, calcite, soot, silica and sulfuric acid are proposed to be used as geoengineering aerosols and have been included in various models [6-8]. Table 2.1 sums up several proposed aerosols and their respective refractive indices and proposed particle radii. The density values are given since it is suggested that density might be of concern for the cost of the aerosol injection to the stratosphere and fall speed [7]. Silicon carbide, diamond and titania-anatase are promising candidates for solar aerosols due to high refractive index and low density. The lowest stratospheric heating due to light absorption has been predicted in case of diamond [8]. On the other hand, rutile phase of titania and sulfuric acid, followed by anatase phase of titania and silicon carbide are found to introduce warming due to both short- and longwave absorption [3, 8]. Calcite aerosols are proposed to react with  $\text{HNO}_3$ ,  $\text{H}_2\text{SO}_4$ ,  $\text{HBr}$  and  $\text{HCl}$  acids, reducing the amount of harmful species from the atmosphere [9, 33]. The model suggests that along with inducing negative forcing, ozone depletion will be eliminated [9, 33]. Keutsch's group from Harvard University has launched SCoPEX in order to assess the influence of calcite aerosols on the atmosphere [10].

Table 2.1: Potential aerosols and their proposed optimal radius based on their refractive indices, and densities [8].

Aerosol	Refractive index (at 550 nm)	Optimal radius, nm	Density (g cm <sup>-3</sup> )
Titania (TiO <sub>2</sub> )-rutile	2.88	130	4.13
Titania (TiO <sub>2</sub> )-anatase	2.55	145	3.79
Silicon carbide (SiC)	2.54	150	3.21
Diamond (C)	<b>2.42</b>	<b>150</b>	<b>3.51</b>
Zirconia (ZrO <sub>2</sub> )	2.17	170	5.68
Alumina (Al <sub>2</sub> O <sub>3</sub> )	1.77	215	3.98
Calcite (CaCO <sub>3</sub> )	1.57	275	2.71
Sulfate (H <sub>2</sub> SO <sub>4</sub> ), 70 wt%	1.43	300	1.69

Another study shows that diamond is the better effective up-scatterer compared to alumina and sulfate, where the minimum ratio of down to up scattering is in the range of diamond particle size of 0.05 to 0.7  $\mu\text{m}$  (see Figure 2.8) [6]. In geoengineering, forward/backward scattering of light is equal to down/up scattering, respectively, described in Chapter 2.1.3.

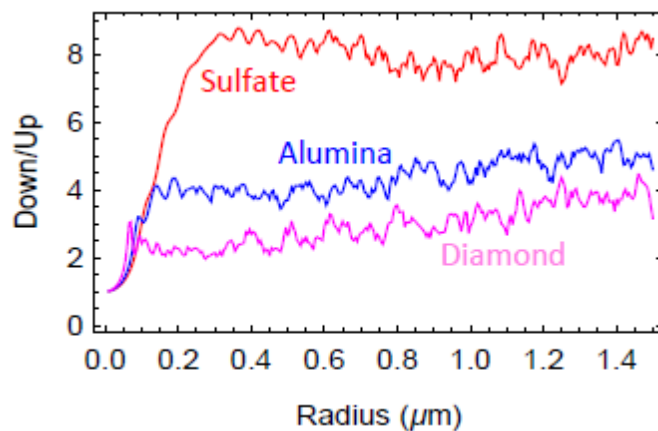


Figure 2.8: Down/up-scattering of diamond is optimal for 0.05-0.7  $\mu\text{m}$ , image taken from [6].

To date, the aerosol field lacks an extensive study to determine whether diamond promotes heterogeneous reactions that lead to ozone loss [6]. Furthermore, experiments need to be performed in the laboratory since real-life materials deviate from models. For instance, particles are not ideally spherical, they contain impurities and other defects. Health and safety issues that use of aerosols might introduce should also be investigated. Namely, some engineering aerosols, such as diamond, are not naturally part of the stratosphere unlike sulfate aerosols [8].

## 2.2 Silica aerogels

### 2.2.1 *Properties and application*

The definition of the term *aerogel* is used to denominate a gel structure where the gas replaces a liquid (usually either water or an organic solvent) and the structure stays about the same (Kistler in 1932) [34]. Silica aerogels are excellent thermal and acoustic insulators with amorphous and highly porous ultralight ( $\sim 99\%$  is air) brittle structure. High specific pore volume and rigid network of silica aerogels, along with transparency, make them suitable for hosting different nanoparticles inside their structure [15]. Wide range of applications, silica aerogels owe to the outstanding properties. In aerospace technology, for instance, the thermal insulating property was used to insulate electronics on the Mars Rover from the cold [34]. NASA stardust collectors are based on high silica aerogel porosity [34].

### 2.2.2 *Optical properties*

Silica aerogel does not absorb in the UV/Vis/NIR up to 1400 nm, hence the interaction with light consists of either transmittance or scattering. Rayleigh scattering, that is proportional to  $\sim 1/\lambda^4$  [35], occurs due to nanostructure of the silica aerogel. Also, since the Rayleigh scattering is more pronounced for the shorter wavelengths, the transmittance takes over scattering when going towards longer wavelengths. Furthermore, the transmittance and reflectance spectra in Figure 2.9 shows that thickness of the silica aerogel sample affects the measurement, with reflectance being higher for the thicker monolithic sample. Simultaneously, transmittance decreases with sample thickness. At wavelengths above 1400 nm, a few distinctive absorption bands are present at wavelengths:  $\sim 1400$  nm and 1900 nm related to water and  $\text{CO}_2$  [36, 37], respectively, and  $\sim 2300$ -2500 nm related to O-H and Si-O [36, 38]. Also, in this range of the electromagnetic spectrum reflectance and transmittance measurements of silica aerogel are not correlated [39]. When the silica aerogel

and air have similar refractive indices ( $\sim 1$ ), as well as when the particles of the silica aerogel are smaller, higher transparency is achieved. Also, the refractive index of silica depends on the bulk density of the synthesised aerogel, a lower density would yield a lower refractive index [40].

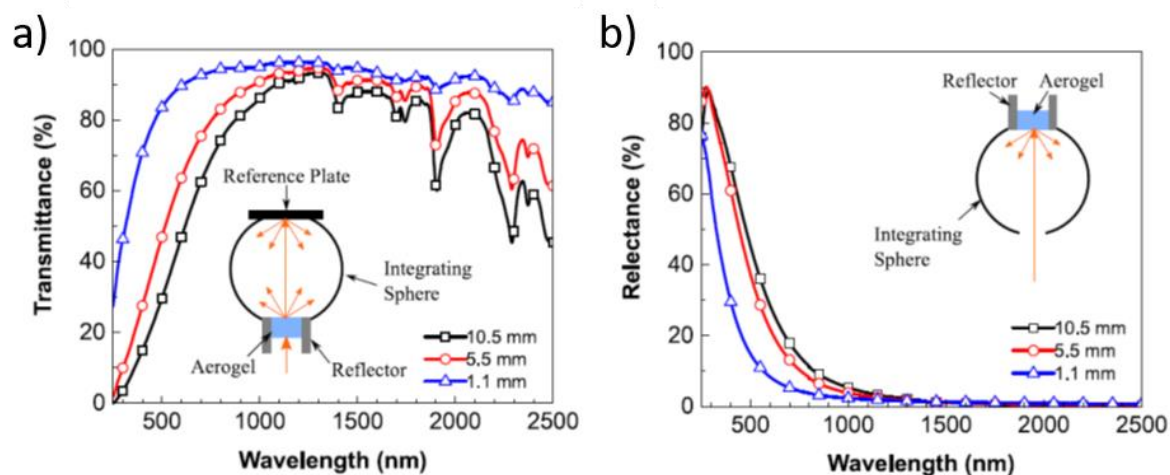


Figure 2.9: Hemispherical transmittance and reflectance for silica aerogel, image taken from [39].

### 2.2.3 Synthesis

Kistler came up first with the term aerogel in 1932 when he used the supercritical method in order to obtain aerogel. The procedure was based on heating the gel above the supercritical conditions (pressure and temperature) of liquid the gel was immersed in. Since the first Kistler's aerogel, many changes have been employed in the synthesis process in order to improve it. Kistler used sodium metasilicate ( $\text{Na}_2\text{SiO}_3$ , waterglass- WG) as a precursor which leads to formation of salt byproduct that needs to be removed later on and requires water to alcohol exchange before the drying. In 1960s, Teichner included alkoxysilane precursors ( $\text{Si}(\text{OR})_4$ , where R is an alkyl and OR is an alkoxide group) in order to eliminate the salt byproduct and avoid the exchange step, shortening the synthesis time. Utilization of carbon dioxide as a drying agent was introduced in 1980s, removing the previously used alcohol from the process, making the synthesis safer. Alcohols are potentially hazardous because they may cause explosions under high temperature/high pressure conditions [34].

The aerogel synthesis comprises of three main steps: sol-gel process, aging and drying. Also, a solvent exchange step is usually added between aging and drying, when the aging solvent is replaced by the drying solvent. The aging solvent may also be the mother solution (the same

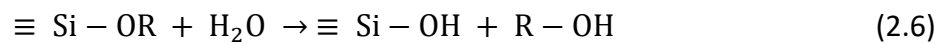
as for sol-gel process), while the choice of the drying solvent depends on the following drying method [12].

### 2.2.3.1 Sol-gel process

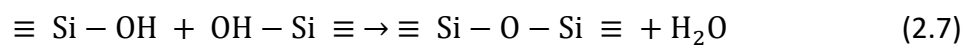
The 3D porous nanostructured network is obtained by polymerization that leads to formation of siloxane bridges ( $\equiv\text{Si-O-Si}\equiv$ ) between Si atoms so that at the end of the process every Si atom is linked to other Si atoms with four bonds by siloxane bridges. The transition from sol (liquid) to gel (solid) is called gelation (or sol-gel transformation) [12].

In case that the alkoxy silane precursors are used, gel formation occurs through reactions of hydrolysis and polycondensation of water and alcohol [34].

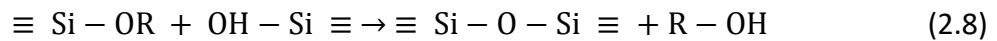
Hydrolysis:



Polycondensation of water:



Polycondensation of alcohol:



Since common alkoxy silanes TEOS, tetramethoxysilane (TMOS), etc.) are not completely miscible with water, alcohols are usually added to the mixture in order to provide full miscibility (see Figure 2.10) [41].

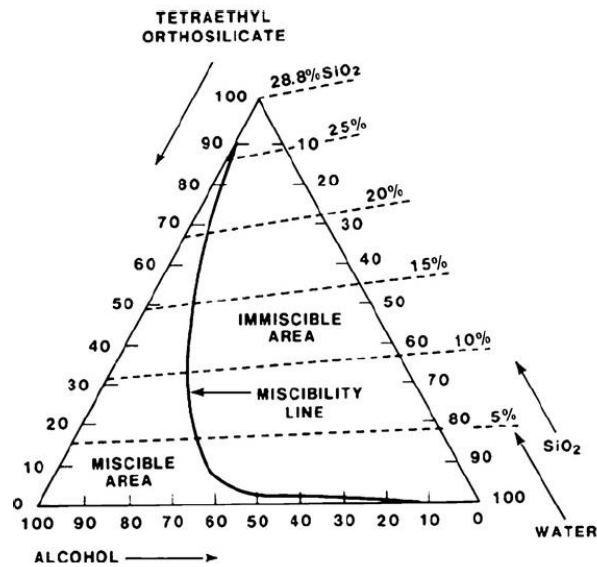


Figure 2.10: TEOS-ethanol-water ternary phase diagram, image taken from [41].

The primary particles that are first generated connect with each other to form secondary particles, giving rise to the final structure. Both primary and secondary particles are bonded to each other with siloxane bridges [12]. Si-O is  $\approx 50\%$  covalent bond [34] which allows  $\equiv \text{Si-O-Si} \equiv$  to have great deal of angle freedom for connection giving the random 3D structure. The bond is polarized so that Si has a small positive charge which gives rise to the slow reaction kinetics unless hydrolysis and condensation reactions are accelerated [34].

The silica particles are about 10 nm in size, while the pore sizes can fit into micropore (less than 2 nm), mesopore (2-50 nm) or macropore (bigger than 50 nm) range. It is common for silica aerogels to have all three types of pores ranging 5-100 nm with average pore diameter being 20-40 nm. The BET surface area is up to 1000  $\text{m}^2/\text{g}$  [41].

Acid and/or base catalysts are used for the sol-gel transformation, which could otherwise take up to a few days to be finished [12]. Acid catalysts are often HCl and HF, while  $\text{NH}_3$ , NaF and  $\text{NH}_4\text{F}$  are often used as base catalysts. Also, different catalysts lead to different morphology of the final aerogel. While acid catalyst increases the speed of the hydrolysis reaction that is now faster than the condensation reaction, the condensation rate is faster than the hydrolysis rate in the case of a base catalyst. The acid catalyst gives polymer-like structure and the base catalyst leads to colloidal gel [34]. Two-step catalysation is often used, when both acid and base catalyst are added to the precursor sol [41]. Figure 2.11 shows that basic pH gives faster condensation than hydrolysis [41].

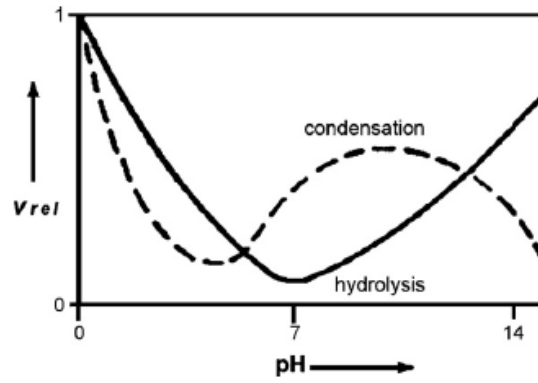


Figure 2.11: Rate of hydrolysis and condensation against the sol pH, image taken from [41].

### 2.2.3.2 Aging

Aging is employed after the gel formation in order to strengthen the gel by increasing the number of bonds between secondary particles. The properties of the final aerogel are improved compared to aerogel that is synthesised without the aging process. Strengthening of the silica network occurs through neck growth, where surface particles first dissolve and then re-precipitate on the neck of the secondary particles, and an Ostwald ripening process, where smaller particles dissolve and then precipitate on the bigger particles (see Figure 2.12) [12].

Both mechanisms are driven by a solubility difference. Solubility,  $S$ , is given by [41]:

$$S = S_0 e^{\left(\frac{2\gamma_{sl}V_m}{RT r}\right)} \quad (2.9)$$

where  $S_0$  is solubility of the solid phase in the case of a flat surface,  $\gamma_{sl}$  is the energy of the solid-liquid interface,  $V_m$  the solid molar volume, and  $r$  is the surface curvature. Neck region of two linked particles has  $r < 0$  and solubility is low compared to particle curvature that is  $r > 0$ . Hence, the neck growth occurs. The Ostwald process is based on bigger  $r$  and consequently lower solubility of the bigger particles compared to the smaller ones [41].

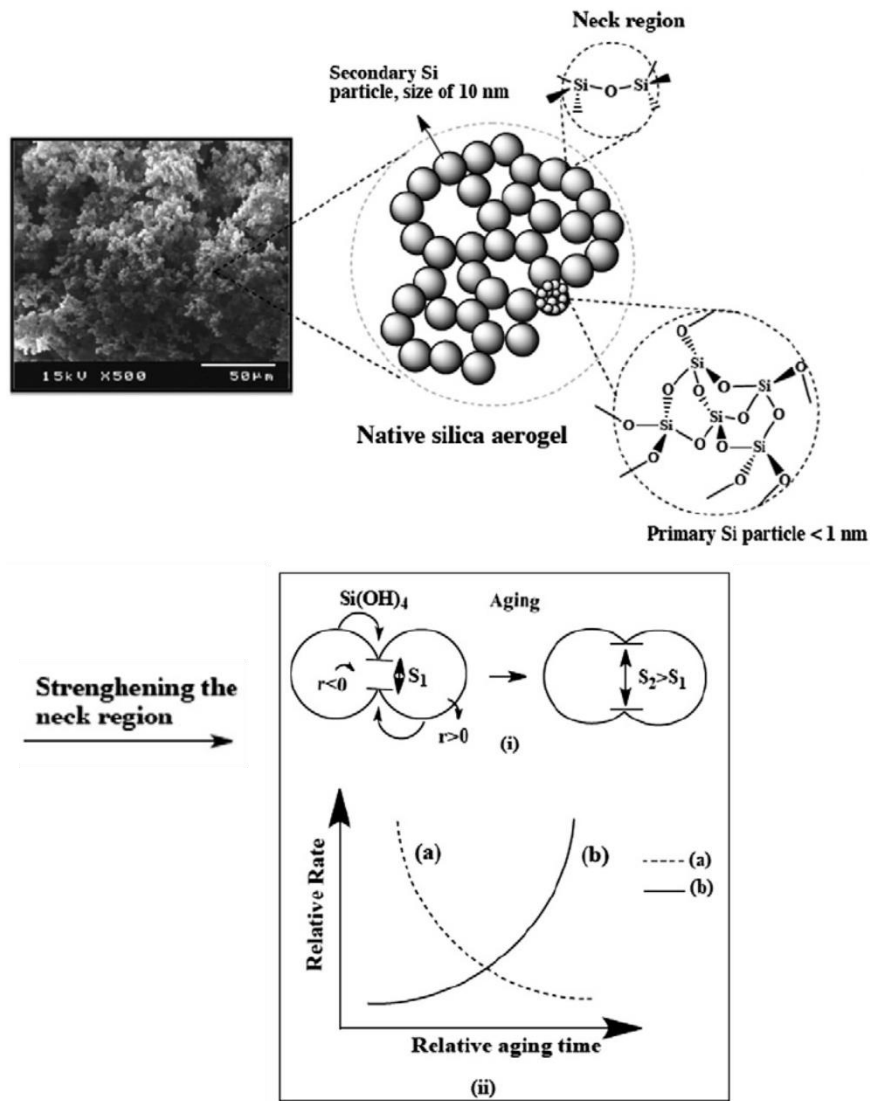


Figure 2.12: Primary and secondary silica aerogel particles; a) rate of neck growth, and b) rate of Ostwald mechanism, image taken from [12].

### 2.2.3.3 Drying

Young-Laplace equation describes the capillary pressure,  $P_{cap}$ , that arises during drying [42]:

$$P_{cap} = \frac{2\gamma \cos \theta}{r_{cap}} \quad (2.10)$$

where  $\gamma$  is the liquid surface tension,  $\theta$  is the contact angle and  $r_{cap}$  is the pore radius. If either surface tension is reduced or contact angle is increased, capillary forces are decreased. Also, bigger pores reduce the capillary pressure during drying. The liquid-vapour meniscus appears at the gel pore and gives rise to tension in the liquid and also a pressure on the pore walls. Capillary stresses cause the shrinkage of the final aerogel by allowing hydroxyl and alkoxy

groups to come closer (than they initially were) and form new siloxane bridges. This is possible due to flexibility of the silica network [34].

There are three common ways of drying the wet gel: evaporation, freeze-drying and supercritical drying [15].

In case of *evaporation (ambient drying- APD)*, strong capillary stresses cause the gel shrinkage and the obtained structure is named xerogel (see Figure 2.13a). The solvent is directly evaporated from the gel when liquid-gas transition takes place (see Figure 2.13b). Low surface tension (LST) solvent such as hexane, heptane, octane and nonane can attenuate capillary stresses, although not completely eliminating the effect. The surface tension increases slightly from hexane ( $\sim 18.4$  mN/m) to nonane ( $\sim 21.8$  mN/m) (water has  $\sim 73$  mN/m, respectively) [43].

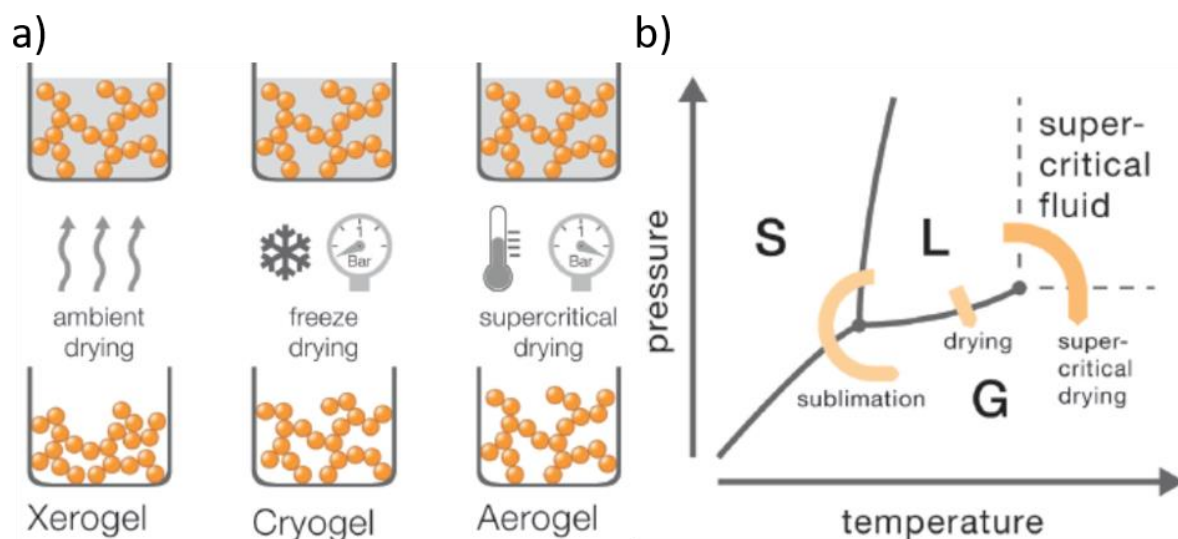


Figure 2.13: a) Drying of the wet gel and subsequent structures, and b) phase diagram of the drying solvent, image taken from [15].

The spring-back effect and hydrophobic aerogels can be achieved by either silylation ( $\equiv$  Si-X functionalisation) (see Figure 2.14) or usage of organosilane precursors (with Si-R groups). Both are based on reducing the number of Si-OH functionalities on the surface, which would otherwise lead to further unwanted condensation [12]. The spring-back effect appears when the gel (the internal surface of the gel) firstly shrinks due to capillary stress and then expands back owing to silyl groups that do not condensate [41]. Prakash et al successfully obtained an aerogel using the surface modification with trimethylchlorosilane (TMCS) [44]. The gelation was carried out from TEOS as a precursor, followed by gelation, aging and washing in ethanol,

after which ethanol was replaced with hexane. After that TMCS was added in order to modify the surface of the aerogel. In this way, spring-back effect prevents irreversible shrinkage [44]. Commonly used alcohols are not completely compatible with alkyltrialkoxysilanes (e.g. MTMS), which is less polar than alcohols. Therefore, surfactant can prevent macroscopic phase separation leading to formation of the cage structure and allow the homogeneous structure giving higher transparency of the final aerogel [45].

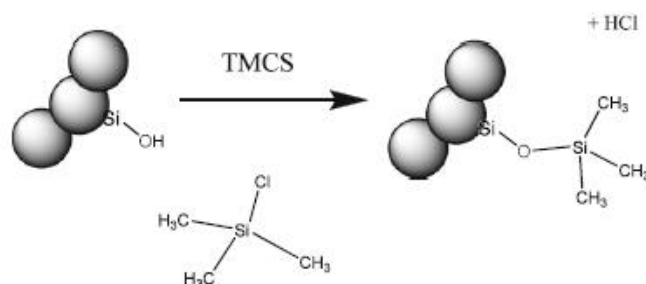


Figure 2.14: Silylation process with trimethylchlorosilane (TMCS), where grey spheres represent silica aerogel particles, image taken from [34].

Although the capillary stresses are overcome, *freeze-drying* gives damaged aerogel network known as cryogel, especially when water is used as a solvent (see Figure 2.13a). During the process, gel is first frozen and solvent transforms to its crystal structure. After that, the solvent is removed by sublimation (when the pressure is decreased) (see Figure 2.13b) [15].

Finally, *supercritical drying (SCD)* gives rise to completely preserved skeleton (aerogel) (see Figure 2.13a and b). Supercritical drying can be divided into two groups: high-temperature supercritical drying (also called H<sub>2</sub>O) in alcohol and low-temperature supercritical drying (COLD) in CO<sub>2</sub>. In case of the COLD process, liquid in the gel is replaced by either liquid or supercritical CO<sub>2</sub> [34]. The COLD method is cheaper due to lower temperature and safer due to non-flammable carbon dioxide [12]. The temperature and the pressure are elevated forming a supercritical fluid. Subsequently, the pressure is reduced under constant temperature so that phase transition occurs without boundary involved. Supercritical drying eliminates both capillary and crystallization forces. Also, it is important to bear in mind what temperatures and pressures are suitable for both material and solvent, so that supercritical conditions required for the solvent are not harsh for the material [15].

The sol-gel chemistry can affect the final aerogel structure and properties. Studies on variation of pH of the waterglass (WG) sol on the final properties of the silica aerogel such as surface

area, pore volume, average pore diameter and bulk density showed that when pH=4 or 5, the hydrolysis is faster than condensation and good aerogel was obtained [46]. However, for pH=6 and 7, condensation is fast and silica particles agglomerate giving rise to decrease in surface area and pore size, and higher bulk density. Additionally, higher pH of the sol decreased the transmittance of the aerogel due to inhomogeneous structure and bigger silica particles [46].

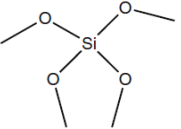
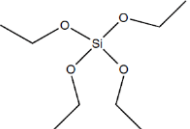
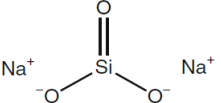
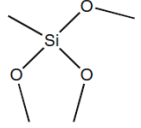
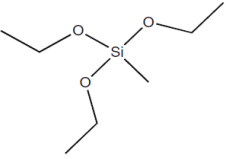
Different aging and drying parameters can also influence the properties of the final aerogels. For example, the best results for an aerogel aging in mother solution (TEOS) were found for up to 48 h and 80 vol% TEOS in isopropanol (IPA), where average pore size, pore volume and surface area increased, while shrinkage and bulk density decreased compared to shorter time and lower concentration of TEOS [42]. In another study, TEOS-based silica aerogels were aged up to 24 h and at temperatures up to 75 °C [47]. At APD, surface area decreases, although remained higher than about 800 m<sup>2</sup>/g, while pore size and volume increase with increased time and temperature of aging for TEOS-based aerogel due to coarsening of the structure [47]. At the same time bulk density decreases with prolong time and higher temperature of aging because the stronger silica network can resist the capillary forces [47]. SCD inherently does not introduce capillary stress, so TEOS and WG prepared with SCD with varying aging parameters does not change the bulk density of the final aerogel, although the surface area follows the same decrease trend [47].

#### *2.2.4 Comparison of different precursors, solvents and modifiers*

Table 2.2 shows the most commonly used precursors, their general properties and the advantages and disadvantages that they imply for the potential use of silica aerogels as host material for optical applications such as solar scattering. As mentioned above (Section 2.1) combination of large-scale production and optimal properties, such as good transparency, low density and hydrophobicity, are essential. The mechanical properties and monolithicity are not the concern in this work since the aerogels for solar scattering are aimed to be used as aerosols in the atmosphere. TMOS, TEOS and WG precursors give transparent, hydrophilic and lower density aerogels compared to methyltrimethoxysilane (MTMS) and methyltriethoxysilane (MTES) precursors that produce opaque and hydrophobic aerogels with higher density [48]. TMOS has the highest optical transparency [49], but causes blindness and it is expensive [50]. MTMS and MTES lead to hydrophobic aerogels without further surface modification, but are opaque and expensive [48, 51], and not the first choice for the intended optical application. TEOS and WG are the most cost-effective and suitable for industrial

production, with WG being four times cheaper [19]. In case of MTMS or MTES are used as precursor, the final aerogel gains in regards to hydrophobicity, but loses transparency, because of the phase separation. Compared to TMOS and TEOS where Si is coordinated by four O-R groups, MTMS and MTES have one R groups and three O-R groups attached to Si. Since Si-R does not take part in the hydrolysis reaction, this leads to a decrease in chain bonding and hence more empty space within the network. Furthermore, because of this MTMS and MTES aerogels are also flexible and hydrophobic [12].

Table 2.2: Most common silica aerogel precursors and the final aerogel properties

Precursor	Structure formula	Transparency	Hydrophobicity	Mechanical Properties	Density, g/cm <sup>3</sup>	Pros	Cons
Tetramethoxysilane (TMOS)		Transparent	Hydrophilic	Hard, brittle	<0.1	Highly transparent, light	Expensive, may cause blindness, hydrophilic
Tetraethoxysilane (TEOS)		Transparent	Hydrophilic	Hard, brittle	<0.1	Low cost, light	Hydrophilic
Sodium Silicate (water glass)		Transparent	Hydrophilic	Hard, brittle	<0.1	Low-cost, light	Semi-transparent, hydrophilic
Methyltrimethoxysilane (MTMS)		Opaque	Hydrophobic	Flexible, soft	>0.1	Hydrophobic	Expensive, opaque
Methyltriethoxysilane (MTES)		Opaque	Hydrophobic	Flexible, soft	>0.1	Hydrophobic	Expensive, opaque

Traditionally, silica aerogel with WG were produced utilizing ion-exchange step, where sodium  $\text{Na}^+$  ions are replaced with  $\text{H}^+$  ions [50]. Schwertfeger et al [52] used WG with hexamethyldisiloxane (HMDSO) and TMCS to produce an ambient pressure dried silica aerogel. HMDSO is added after aging for solvent exchange and as drying solvent. In this process, solvent exchange and surface modification occur at the same time based on the immiscibility of hydrophobic HMDSO and water/HCl phase (see Figure 2.15). Silylation occurs by attaching  $-\text{Si}(\text{CH}_3)_3$  groups from the TMCS in the HMDSO layer which grows during the process. In this way, the surface is modified and the water is pushed out from the pores and decanted. After that, Lee et al [53] improved the process by using IPA (isopropylalcohol) and hexane solution instead of the more expensive option (HMDSO) as a solvent. IPA with both polar and nonpolar groups helps the phase separation between water and hexane [19]. Also, a hydrophobic aerogel was reported from modification with ethanol/TMCS/heptane solution [41]. Bangi et al [54] used tartaric acid during synthesis excluding the use of ion-exchange. However, before modification with methanol/TMCS/hexane, washing is needed in order to remove salts (sodium tartarate) produced from the reaction of WG and the acid. Picking up on that, Pooter et al [19] further modified the synthesis of silica aerogels integrating ion-exchange, solvent exchange and modification into a single step with HMDSO as solvent and  $\text{HNO}_3$  as catalyst, after which the organogel was decanted from the aqueous phase. Similarly, Zhao et al [20] obtained a powdered silica aerogel in about 2 h using WG, hexane, hexamethyldisilazane (HMDZ),  $\text{HNO}_3$  and IPA (see Figure 2.15b). The possibility of obtaining a silica aerogel in such a short time and with low-cost WG and production process has immense impact on commercial production of cost-effective WG-based silica aerogel. The use of either HMDSO or HMDZ with  $\text{HNO}_3$  as a catalyst results in no HCl as a by-product, which is very corrosive and not suitable for industrial production [19]. Additionally, Han et al [18] and Liu et al [55] have also reported a low-cost process with using TMCS, but not as a surface modifier starting from WG, TEOS and MTMS. Although this approach also uses TMCS for drying, TMCS does not modify the surface and it is hydrophilic after drying. TMCS reacts with pore water to obtain trimethylsilanol (TMS) and HCl, that is then combined with sodium bicarbonate solution to yield NaCl, water and carbon dioxide (see Figure 2.15c). Carbon dioxide that is formed during the process opposes the capillary pressure and prevents the structure collapsing during drying. The undesirable by-product HCl of general surface modification is eliminated and NaCl can be washed away [18]. Similarly, Lu et al [56] obtained a granulated

TEOS-based aerogel with ammonium bicarbonate ( $\text{NH}_4\text{HCO}_3$ ) that gives rise to  $\text{CO}_2$  and  $\text{NH}_3$  gases during heating.

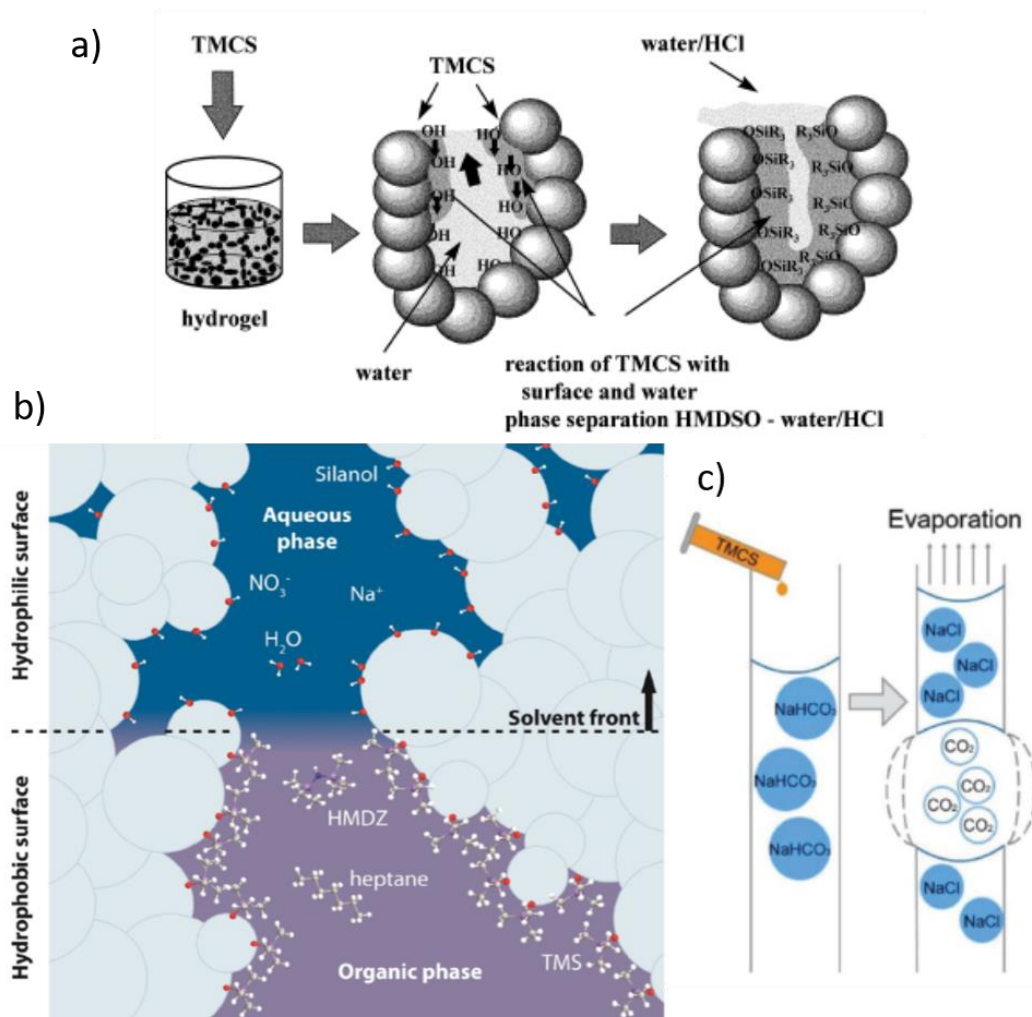


Figure 2.15: a) and b) Phase separation and surface modification, images taken from [20, 52], respectively, and c) APD with sodium bicarbonate, image taken from [18].

In addition to commonly used precursors, literature reports some other precursors that lead to transparent silica aerogel which is suitable for solar scattering application. Parale et al [57] studied tetrapropoxysilane (TPOS)-based and TMCS modified silica aerogel that showed good properties such as high surface area, low density and good transparency. Polyethoxydisiloxane (PEDS) silica precursor, which is basically polymerized TEOS, has long been known for superior transparency compared to TMOS and TEOS studied by Wagh et al [49]. When compared TMOS, TEOS and PEDS using SCD, PEDS shows the highest surface area and porosity, the lowest bulk density and the highest transparency of the three, with values

of 1100 m<sup>2</sup>/g, 97 %, 98 kg/m<sup>3</sup> and 93 % (at 900 nm wavelength), respectively. The price of PEDS is a limiting factor for use on the larger scale [40].

Another way to achieve hydrophobicity and retain transparency is to use co-precursor-based aerogels such as MTMS/TMOS and MTES/TEOS and MTMS/WG. The use of MTMS/TMOS aerogel is limited to high cost precursors and hazardous TMOS, although good properties have been reported [58]. Pisal et al [51] managed to synthesise a MTES/TEOS aerogel with 50:50 precursor ratio that compromised between good surface area, hydrophobicity and transparency. For example, when the ration shifted towards more MTMS, the final aerogel had better surface area and hydrophobicity, but transparency decreased to 87 % (at wavelength 700 nm). Pan et al [59] studied MTMS/WG, among good hydrophobicity, surface area and density, transparency was not on that level reported for MTES/TEOS. Nah et al [60] compared different methoxysilane agents for surface modification, where dimethyldimethoxysilane (DMDMS) is suggested to be good silylating agent such as commonly used TMCS and HMDZ.

#### *2.2.5 Optical application of the doped silica aerogel*

Silica aerogel can be used for doping with various nanoparticles, while the optical properties of the nanoparticles in the final aerogel remain [15]. Doped-silica aerogels have been used for optoelectronics and to study photoluminescence. Regarding precursors for these optical applications, TMOS and TEOS have been used [61, 62]. The doping materials aimed for the optical application are quantum dots and dyes [15]. The composite structures made of silica aerogels with different carbon nanostructures in the form of nanotubes, nanofibers, and graphene have also been developed [16]. Nanodiamond-doped silica aerogel was prepared in order to study decay time of photoluminescence of the nitrogen-vacancy (NV) colour centre in nanodiamonds in silica aerogel [63]. Furthermore, silica aerogels have a potential to be used in space engineering due to attenuation of harmful UVA and UVB radiation (280-400 nm) [13] and another study showed that it does not degrade under UV exposure [14]. Zhou et al have fabricated silica aerogel doped with carbon quantum dots, where rigid silica matrix prevent agglomeration of carbon dots in the solid state, avoiding photoluminescence quenching [62].

In this work TEOS is chosen as low-cost precursor leading to highly transparent silica aerogels (see Chapter 5 and Chapter 6). Also, it is aimed to study the optical properties before considering other aspects of an optimal solar scattering material.

### 2.3 Diamonds

Carbon can be found in four different forms, from 0-dimensional to 3-dimensional material [64]:

- 1) 0-D or fullerene
- 2) 1-D or nanotube
- 3) 2-D or graphene
- 4) 3-D or diamond

All these forms are based on  $sp^2$  and  $sp^3$  hybridization of carbon atoms (see Figure 2.16). Fullerene ( $C_{60}$ ) is made out of 60 atoms, which give rise to 12 pentagons and 20 hexagons, eventually forming an icosahedron. Carbon nanotube, as well as graphene, is  $sp^2$  hybridized. Multiple layered graphene is known as graphite. The strong covalent bonds are present within the plane while van der Waals forces bond graphite layers [64]. The main difference between diamond and graphite that the hybridization of diamond is  $sp^3$ , while graphite has  $sp^2$  hybridization with three  $\sigma$  and one  $\pi$  bond [65]. These  $\pi$  orbitals are delocalized and contain electrons with high mobility making graphite a good electrical conductor [66].

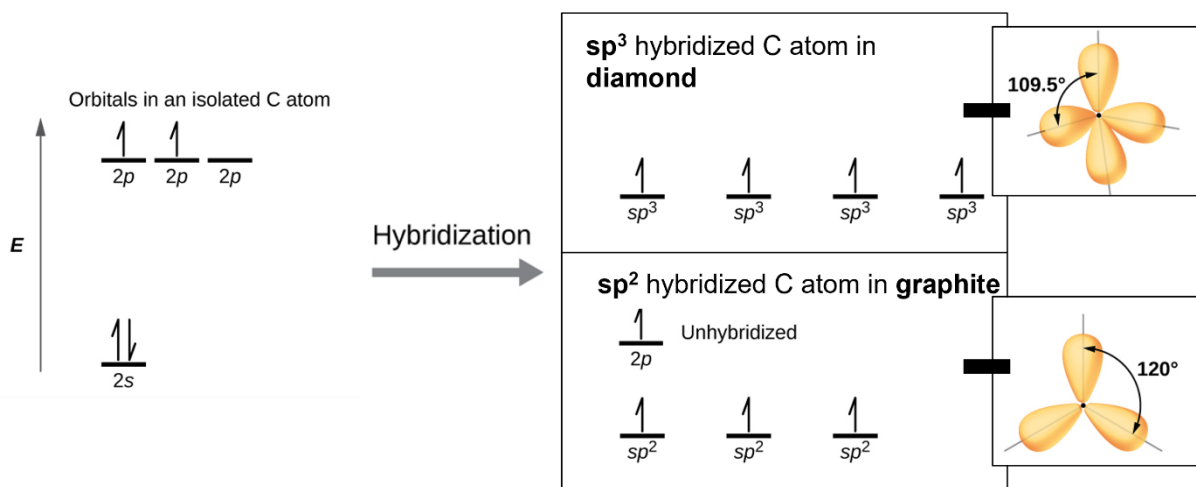
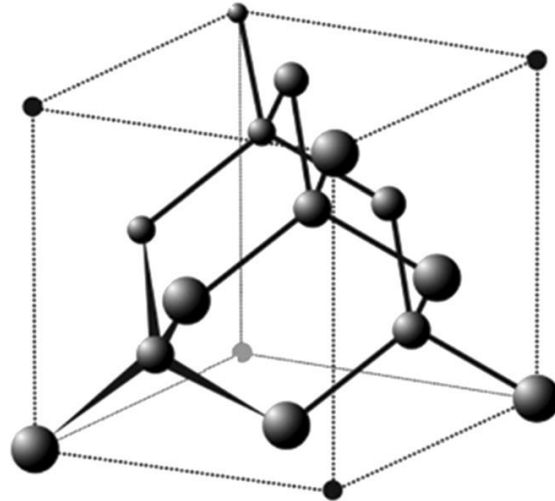


Figure 2.16: Diamond and graphite hybridization, image taken from [67].

As mentioned above, diamond consists of  $sp^3$  hybridized carbon atoms with a coordination number of 4, forming a tetrahedron (see Figure 2.17). Indeed, diamond owes its properties to the strong covalent bonding of carbon atoms. The primitive unit cell is a face-centred cubic (FCC) lattice with a 2 atom basis. From one atom at a lattice point the second atom is located at  $[111]a/4$ , where  $a$  is the lattice constant. The packing fraction is 34 % [64].



*Figure 2.17: Diamond unit cell, image taken from [68].*

Remarkable properties of bulk diamond such as electrical resistivity, chemical stability, corrosion resistance, biocompatibility, hardness, Young's modulus, low thermal expansion coefficient and excellent optical properties are also translated to nanodiamonds [11]. The high thermal conductivity of diamond at room temperature (25 W/(cmK)) makes diamond extremely resistant to thermal shock, outperforming silver and copper by a factor of five [69].

### *2.3.1 Optical properties of diamond*

The symmetry of covalent bonds present in diamond contributes to no interactions of light (with lattice vibrations) in the infrared (one-phonon region). Transparency region of diamond covers the spectrum range from 225 nm (UV) to microwaves. On the other hand, higher order IR absorption is present from 2.5-6  $\mu\text{m}$  ( $1700\text{-}4000\text{ cm}^{-1}$ )- multiple phonon absorption causes weak dipole [69]. One diamond Raman mode is present at  $1332.4\text{ cm}^{-1}$  ( $7.505\text{ }\mu\text{m}$ ). Diamond exhibits high refractive index (standard  $n=2.41$  at 589.29 nm-yellow) in visible with high dispersion and no dispersion in IR [70]. UV light is absorbed below 225 nm (5.50 eV) that matches the indirect bandgap of diamond [69].

The most important optical property of diamond for geoengineering applications, and therefore for this work, is its ability to scatter of light [69]. Diamond is chosen because of its high refractive index, along with other convenient properties such as the absence of IR absorption [8] and non-toxicity [11].

### *2.3.2 Diamond synthesis*

Natural diamonds mainly get to the Earth's surface by magma or molten rock [64]. They are originally produced at depth of 150 km in Earth's mantle, where extreme pressures (45–60 kbar) and temperatures (900–1300 °) exist. When magma travels towards the surface, it passes through the zone where diamond is present in a stable form, picking them up to the surface [64]. The other scenario is that diamond is brought up from the subduction zone when rocks are raised again to the surface [64]. At the Earth's surface, conditions are in favour of graphite rather than diamond formation, but once produced, the temperature is needed to be ~ 600 °C in order for diamond to burn (be decomposed to carbon dioxide). Also, the graphitization temperature in vacuum is ~ 1500 °C [69]). They were firstly mined in India, Brazil and then in Hopetown, South Africa [64], while the main mining fields today are in Russia, Botswana, Congo, Australia and Canada [71].

The high pressure high temperature method for producing synthetic diamond was first discovered in 1955 [72]. After that, in 1971, the process was modified by using the temperature gradient as the driving force for the crystal growth [72]. Synthetic detonation nanodiamonds were discovered in attempts to study the synthesis of diamond by shock-wave compression of non-diamond carbon materials (1960s-1980s) [73]. Chemical vapour deposition (CVD) method was introduced for fabricating diamond film on various substrates in 1980s [69].

Figure 2.18 shows the stability conditions (pressure and temperature) of graphite and diamond [64]. HPHT methods imitate the natural diamond synthesis. The precursor for HPHT is graphite that is transformed into diamond. When the catalyst is used in HPHT synthesis, diamond can be produced at lower pressures and temperatures compared to the conventional HPHT synthesis. This method is mainly used for diamond application in machining tools such as drill bits and abrasives. Detonation synthesis is based on explosion of carbon source precursors under extreme conditions in absence of oxygen, leading to

nanodiamond formation [74]. Amazing diamond properties are passed to nanodiamonds which allow them to have wide range of applications (e.g. they can be used in chromatography, magnetic resonance imaging, etc., while the doped diamond can be even used for electrochemistry, batteries and capacitors) [74]. CVD process uses pressures lower than atmospheric and temperatures up to about 1000-1400 K, with gas as a precursor. The CVD of diamond is used for producing optical coatings and elements [64], and heat spreaders for electronic devices [69, 75].

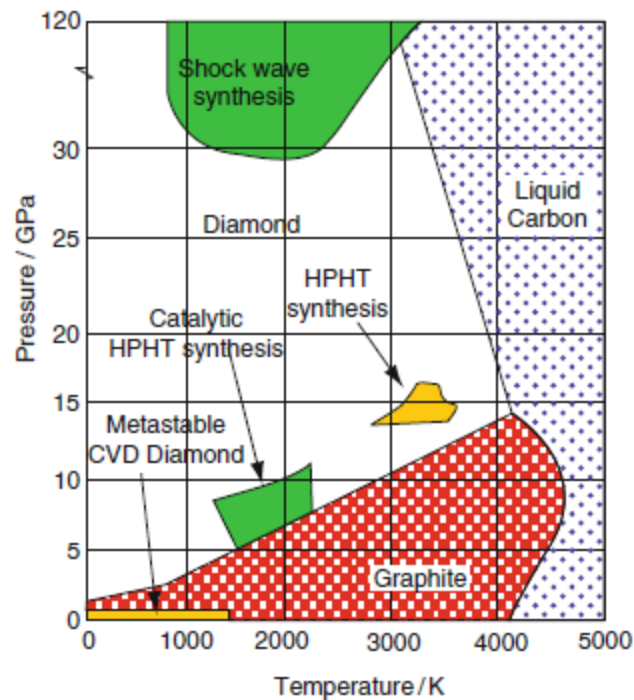


Figure 2.18: Phase diagram: diamond and graphite stability zones, image taken from [64].

### 2.3.2.1 High pressure high temperature

Figure 2.19 shows the HPHT setup (see Figure 2.19a) with HPHT cell (see Figure 2.19b). Two pistons are used in order to produce the pressure conditions for diamond formation, while heating element next to the pressure transmitting medium provide the required temperature. Growth cell contains hot (upper) and cold (lower) region. Carbon source (graphite) is placed in the hot region, while diamond seeds are put on the bottom of the cell, and the cell is coated with ceramic pad [72]. The solvent-catalyst system (Fe,Co, Ni), nitrogen getters (Ti, Al) and inhibitors (Cu prevents TiC formation) are in between the two regions [76].

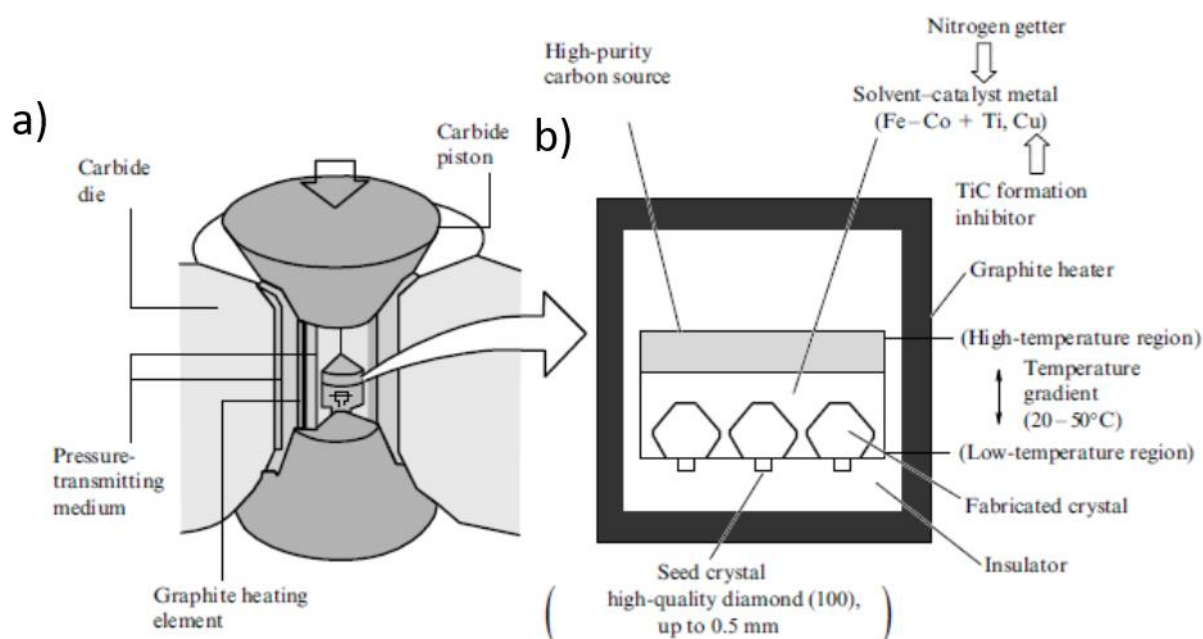


Figure 2.19: HPHT synthesis: a) HPHT setup, and b) the HPHT cell, image taken from [72].

The temperature is in the range of 1600-1700 K, while the pressure is  $\sim 6$  GPa. As mentioned above, the temperature gradient method is used for the HPHT synthesis. The process occurs by the dissociation of graphite and due to temperature difference diamond is formed at the bottom of the cell [72]. P-T conditions control the crystal shape. For example, the shape changes from cube to octahedral (and in between), with an increasing temperature [77]. HPHT microdiamonds are the subject of Chapter 4 and Chapter 5 of this thesis. In Chapter 4 both raw and 1-undecene-functionalized HPHT microdiamonds are characterized. Raw HPHT microdiamonds are doped to silica aerogel in Chapter 5 and characterized, and for the first time the optical reflectance of the pure microdiamond powder and microdiamond/silica aerogel composite is measured.

### 2.3.2.2 Detonation synthesis

The usual precursors for detonation synthesis are TNT (2-methyl-1,3,5-trinitrobenzene) and RDX (1,3,5-trinitroperhydro-1,3,5-triazine) (see Figure 2.20a) which are explosives with negative oxygen balance [74]. Coolants are also needed for the process, hence detonation is performed in presence of gases such as  $N_2$ , Ar,  $CO_2$ , or solid or liquid  $H_2O$  [74]. Shock-wave (zone I) induced by the precursor explosion leads to their decomposition (zone II) due to high temperature and pressure (see Figure 2.20b and c). Zone III indicates completion of the primary carbon clusters, while zone IV represents expansion of the primary clusters and

formation of the secondary particles (V) in the liquid droplets (VI). Also, crystallization and growth take place and nanodiamond are formed (VII). After that, pressure and temperature are further decreased (beyond diamond-graphite line) which is now suitable for graphite products instead of diamond (see Figure 2.20b). At the end of the detonation process, the product is collected from the detonation chamber (including the chamber walls) [74].

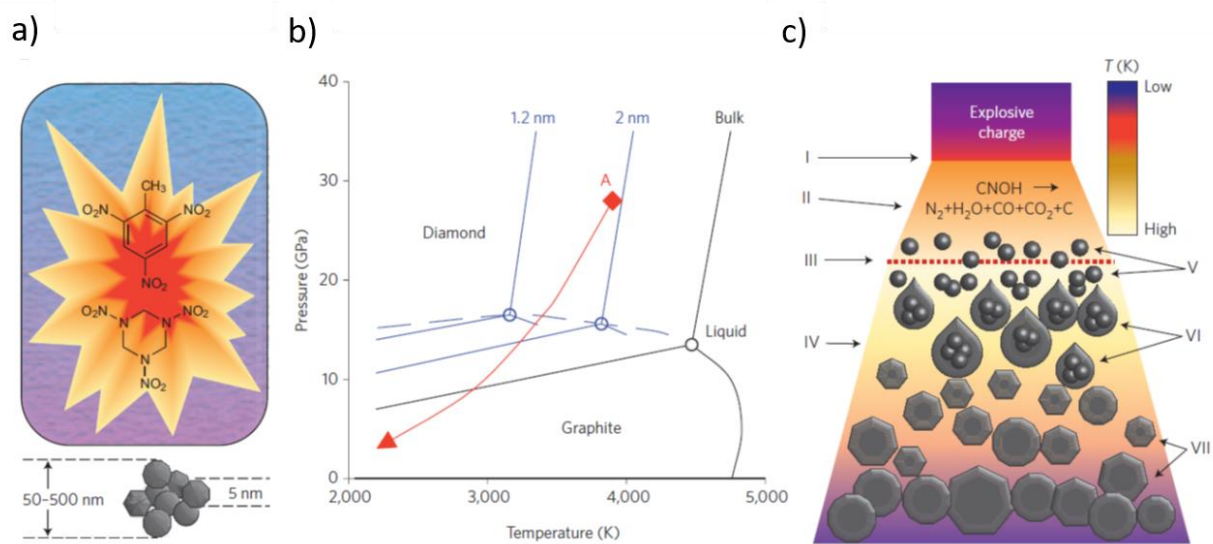


Figure 2.20: Detonation synthesis: a) detonation precursors and nanodiamond product, b) reaction path, and c) the following resulting structure, image taken from [74].

Detonation process has certain advantages over other synthesis methods such as a small size of obtained nanodiamonds (average particle size is 4-5 nm) and a narrow size distribution (majority of particles are between 2 and 20 nm) [78]. According to Kruger et al primary particles form: core aggregates (100-200 nm), then intermediate aggregates (2-3  $\mu\text{m}$ ) and agglomerates (20-30  $\mu\text{m}$ ) [79]. Also, detonation nanodiamonds (DNDs) are readily available in tons per year [73]. Alongside the agglomerates, the detonation product (soot) also consists of non-diamond carbon and metal impurities. The diamond core is surrounded with other types of non-diamond carbon structures such as amorphous carbon, carbon onions, fullerenic shells and graphite ribbons [80]. The high diamond content corresponds to the high content of the  $\text{sp}^3$  carbon, while  $\text{sp}^2$  carbon gives the black colour to the raw detonation powder (see Figure 2.21) [80]. Both agglomerates and non-diamond products obtained in the synthesis disable the potential application of nanodiamonds [81]. Here lies the main disadvantage of detonation synthesis over the HPHT process, where the defects are present in lower concentrations [82].

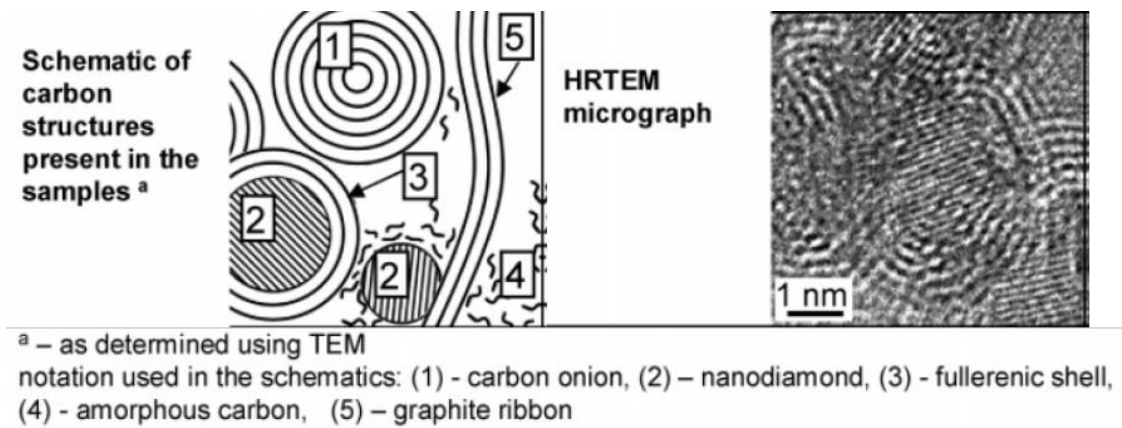


Figure 2.21: Detonation nanodiamond structure, image taken from [80].

#### 2.3.2.2.1 Purification and functionalization of detonation nanodiamonds

Conventionally, strong acids (sulfuric, nitric and hydrochloric) are used for DND oxidation, which not only purifies the nanodiamonds from graphitic and metal impurities, but also terminates the nanodiamonds surface with oxygen groups [83]. Acid purification is costly and hazardous, and also could be ineffective for removing all  $sp^2$  content, leading to up to  $\sim 80\%$  of  $sp^3$  [80]. Osswald et al have shown that 5 h air oxidation at 425 °C decreases the amount of  $sp^2$  carbon on diamond surface, recovering the primary nanodiamonds particles (5 nm) with  $\sim 95\%$   $sp^3$  content [80]. Graphitization-oxidation heat treatment performed at 1000 °C in nitrogen, followed by 450 °C in air, can improve the de-agglomeration to a certain point although resulting in a rise in bigger agglomerates (10-50 nm) [84]. Ackermann et al demonstrated that ozone treatment can successfully oxidize the diamond surface [85].

Most common termination of nanodiamonds is with carboxyl (COOH) and carbonyl groups (ketones, aldehydes, etc) originating from purification by oxidizing acids and in air, where  $sp^2$  bonds tend to react more easily than  $sp^3$  [83]. Metal inclusions also are removed by acids. Furthermore, hydroxylated, hydrogenated and aminated NDs have been reported [83]. Especially for the biological application, many molecules have been attached to the diamond surface via either non-covalent or covalent bond [83, 86].

#### 2.3.2.2.2 De-agglomeration of detonation nanodiamonds

Many research groups have dedicated their work to investigating nanodiamond colloidal stability. The key to de-agglomeration lies in increasing the repulsive forces between

nanodiamonds [87]. This has been done by reducing the size of the nanodiamond agglomerates and/or changing the particle surface [87].

Although core nanodiamonds agglomerates (100-200 nm) cannot be separated by simple sonication or ball milling, combination of beads milling and sonication (bead-assisted sonic disintegration-BASD) can decrease the agglomerate size down to 5-10 nm particles size [88]. Also, bead-assisted ball milling (zirconia beads) gave rise to smaller than 10 nm [89]. Similarly, dry media has been used alongside ball milling (steel grinding balls) to crush down the agglomerates. Salt (NaCl)- or sugar (sucrose)-assisted ball milling [90] obtained stable colloid, where 1-2 primary particles formed stable colloid particles smaller than 10 nm. The advantage of this process is that is easy to remove the milling media by simply rinsing, in contrast to ball milling with zirconia that leaves residue and it is more difficult to get rid of. Metal contamination from the steel balls can be overcome by salt-assisted ultrasonic de-aggregation (SAUD) [91] that also leads to similar results (~ 5-10 nm particle size). Detonation nanodiamonds were air annealed at 425 °C (2 h) before the sonication treatment. The DND size was in the 50-1000 nm range before the de-agglomeration treatment [91].

#### *2.3.2.3 Detonation nanodiamonds and high pressure high temperature diamonds comparison*

Nanodiamonds are commercially produced either by detonation synthesis, or by grinding the microdiamond powders obtained by the HPHT process [82, 92]. Detonation nanodiamonds and HPHT nanodiamonds have similar structure, but different size and surface properties. HPHT nanodiamonds do not tend to agglomerate strongly, while detonation diamonds form tight agglomerates. Table 2.3 shows comparison between HPHT and DNDs. The detonation nanodiamonds are smaller in size with the primary particles of about 4-5 nm, compared to about 10-20 nm of HPHT nanodiamonds [82, 93]. The main shortcoming of detonation synthesis is that the primary detonation nanodiamonds particles form tight agglomerates (up to 500 nm), that often interfere with many potential applications of detonation nanodiamonds such as fluorescence quenching [93]. Similarly, ceramic/metal impurities contaminate the HPHT diamonds and further purification after the milling process is needed [94]. Additionally, stress produced during the milling and graphitization leads to fluorescence quenching [94]. There have been attempts to overcome this. The detonation explosion performed on HPHT microdiamonds (20 and 150  $\mu\text{m}$ ) gave rise to particles between ~ 400-800 nm [94]. This method has been proposed as it is a potentially less expensive and less time-

consuming alternative to the milling of HPHT microdiamonds to obtain nanodiamonds without the contamination from milling [94]. Additionally, small HPHT diamonds (1 nm in size) have been obtained by controlled annealing at 500 °C, followed by centrifugation, where not only the removal of the graphitic shell was accomplished, but also the etching of diamond led to a decrease in the size of the nanodiamonds obtained [82].

*Table 2.3: Comparison of HPHT and DND particles.*

Diamond type	Particle size	Carbon hybridization	Advantages	Disadvantages	Geoengineering
HPHT	10-20 nm	sp <sup>3</sup>	sp <sup>2</sup> carbon-free surface	Need for grinding	In general transparent, except the absorption - due to substitutional nitrogen impurities
DND	4-5 nm	sp <sup>3</sup> /sp <sup>2</sup>	Smaller size	Need for purification, de-agglomeration	Absorbs in the UV/Vis

### 2.3.3 Colloids

Zeta potential is often stated in the literature as a measure of colloid stability. It is defined as a potential that is formed on the surface of a particle in a colloidal dispersion. The electrical double layer is formed around the particle. The potential at the slipping plane is known as Zeta potential. In general, if the magnitude of the zeta potential exceeds  $\pm 30$  mV, it is assumed that the colloid is stable and that particles in the colloid will not agglomerate based on the sufficiently strong repulsive forces between the particles [95].

The negative Zeta potential of nanodiamonds is due to the carboxyl and hydroxyl groups present on the particle surface. Those functional groups can be de-protonated, which causes a negative charge on the surface and a proton is transferred to the surrounding medium. It also means that if there are more particles in the solution, the pH would be reduced, because the concentration of  $H^+$  would increase [96].

On the other hand, positive Zeta potential is reported on less occasions and various explanations aiming to understand the origin of the positive charge have been proposed in the literature [96]. Amino functional groups ( $NH_2$ ) can be protonated in the acidic environment to yield  $NH_3^+$  [97]. Amino groups are obtained either with wet chemistry (reaction with amino-source) [98] or by heating the chlorinated diamond in gaseous ammonia [83].

Other papers suggest that the existence of surface  $sp^2$  carbon plays an important role for the positive Zeta potential of nanodiamonds. Namely, the graphitic shell on top of the diamond core is necessary to accommodate electron polarization between the core and the shell, where an electron is transferred to the graphitic layer [99].

Oxygen-free Lewis base sites have been related to the positive Zeta potential according to [96] (see Figure 2.22). In aqueous solution,  $H^+$  ions interact with the surface of the particle. The graphitic carbon is formed on the nanodiamond surface by vacuum annealing (1000 °C), which also results in the oxygen groups disappearing from the same surface (creating oxygen free sites) [96]. The experiment is further performed by annealing in hydrogen (500 °C) to allow hydrogen termination of the surface so the oxygen cannot re-adsorb [96]. It is also shown that with the increasing concentration of nanodiamonds, the pH becomes more basic, because the  $H^+$  are removed from the solution by the Lewis base sites [96]. Similarly,  $H_3O^+$  ions can be adsorbed on the graphitic planes giving a positive Zeta potential [100].

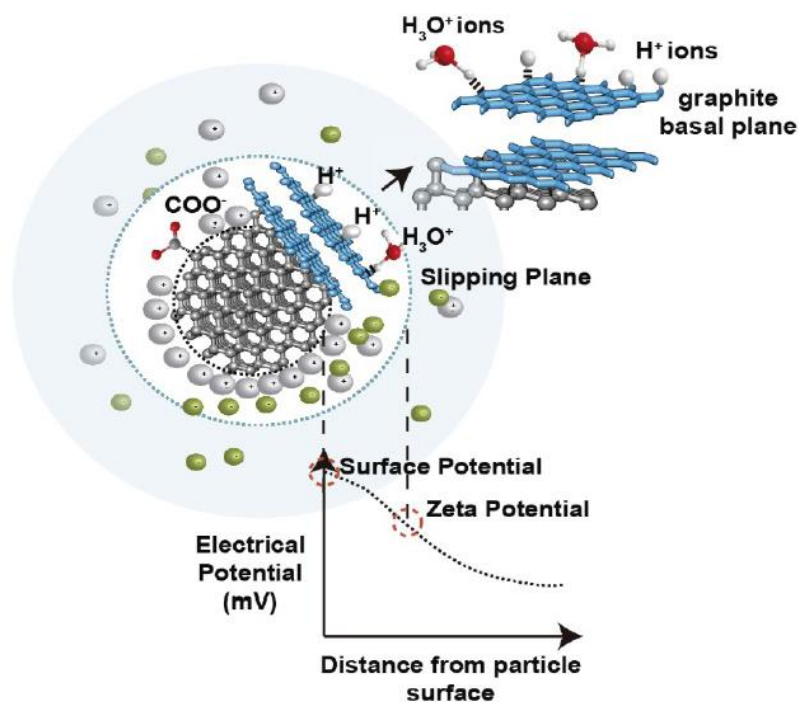


Figure 2.22: Diamond particle surrounded by graphitic carbon, image taken from [96].

Petit [99] has proposed a mechanism known as an oxygen hole doping, where nanodiamonds are heated in a vacuum at a temperature of about 750 °C. During annealing in vacuum the physically (weakly) adsorbed O<sub>2</sub> would desorb leaving the sp<sup>2</sup> carbon on the surface (this is provided with temperatures below 700 °C). In other words, the content of oxygen on the surface will decrease, while the sp<sup>2</sup> content will increase with the increasing temperature. At 750 °C, the molecular oxygen will attach on the surface as an endoperoxide group [99]. The chemisorption of the molecular oxygen is enabled by the aforementioned spontaneous polarization [99]. Furthermore, in the acidic medium the endoperoxide group is protonated (hole in the π orbital is formed) giving rise to a positive potential [99]. With more alkaline pH, Zeta potential decreases because the endoperoxide group is in the neutral state [99].

After synthesis and de-agglomeration, positive nanodiamonds can be employed in colloids in order to fit the needs for various application such as device seeding [101]. The amazing thermal conductivity of diamond (2000 W/mK at 300 K) is often utilized in semi-conductive devices such as high electron mobility transistors (HEMTs) for use in radio frequency applications [101]. One example are GaN devices, where diamond has a role as a heat spreader [101]. Although a single crystal diamond has shown to fulfil the application very well,

the single crystal fabrication cost limits further investigation into the diamond use in GaN devices. When it comes to reducing the cost of the diamond, the polycrystalline diamond seems like a logical option [101]. Yet it is difficult to compete with the properties of a single crystal, since the material with low thermal conductivity, usually silicon nitride, is usually utilised to adhere diamond layer to GaN [75, 101]. Also, it has been reported that different surface termination, as well as different diamond seed sizes, influences the growth of diamond [101, 102].

Particularly interesting to this thesis is the behaviour of the nanodiamond particles terminated with hydrogen atoms (ND-H) in colloid, upon addition of acid. When the concentration of HCl acid added to the colloid is high, the colloid becomes unstable [95]. This has been attributed to the Coulomb depletion effect, which is a common feature in colloids in the presence of a high concentration of counter ions ( $\text{Cl}^-$ ) [95]. That counter charge is adsorbed from the nanoparticle surface and gives rise to the depletion zone between the nanoparticles adjacent to each other [95]. The dominant repulsive forces between counter charge over the nanoparticles repulsive forces cause aforementioned depletion zone and ultimately lead to the agglomeration of nanoparticles although the Zeta potential is greater than 30 mV [95].

The results of the analysis of detonation nanodiamonds with positive Zeta potential and an original concentration of 4 wt% of nanodiamonds in deionized (DI) water (from NanoCarbon Institute, Japan) are presented in Chapter 6. Furthermore, the dilution of 1 wt% of nanodiamonds is compared to the original colloid. There have been reports on a similar, 5 wt% colloid obtained from the NanoCarbon Institute with positive Zeta potential obtained by zirconia beads milling [103]. Furthermore, they came up with rather interesting observation that the nanodiamonds agglomerate upon dilution [23, 98]. The 5 wt% and 0.3 wt% colloids were compared to one another and the dynamic light scattering (DLS) data shows that the primary nanodiamond particles ( $\sim 3$  nm) agglomerated in case of 0.3 wt% dilution [23, 98]. Also, soft gel is formed when the nanodiamond concentration is above 8 wt%, which can be similarly reversed to a stable colloid by adding DI water [103]. In this thesis, the stability of nanodiamond colloids (4 wt% original and 1 wt% diluted) are measured using DLS and Zeta potential and compared over a period of time (6 days) (Chapter 6). Understanding the stability of colloids is useful for device seeding [101]. Furthermore, detonation nanodiamonds are

added to the silica aerogel before gelation and the properties of the nanodiamond-doped silica aerogel such as loading of nanoparticles in aerogel and surface area and bulk density of the doped aerogel are studied in Chapter 6.

## Chapter 3 Methodology

*In this chapter, experimental procedures, theory behind the characterization techniques and parameters used, were presented. Experimental procedures for the functionalization of the HPHT microdiamonds with 1-undecene chains, preparation of different detonation nanodiamond colloid dilutions, as well as preparation of HPHT microdiamond- and detonation nanodiamond-doped silica aerogels, were described. Assessing the microdiamond size and shape before and after the treatment was achieved by SEM and TEM. SEM and TEM were also used to observe the structure of pure and micro- and nanodiamond-doped silica aerogels. XRD was used to observe crystallinity and purity of microdiamonds, as well as to obtain diamond content in doped silica aerogels. Additionally, presence of graphitic carbon in microdiamond powders was investigated by Raman scattering spectroscopy. FTIR and NMR spectroscopy examined the surface and surface groups of microdiamonds, while DLS was used to get nano- and microdiamond particle sizes. Surface groups of pure and doped silica aerogels were detected using FTIR. The study of dilution of the original 4 % nanodiamond colloid and stability of nanodiamonds in the colloids was carried out using Zeta potential and pH measurement. Also, nanodiamonds were imaged using HRTEM and SAED was used to identify nanodiamonds. In order to observe the presence of graphitic carbon, EELS spectrum and UV/Vis absorption spectroscopy were used. BET and BJH theories gave surface area and pore size distribution values for pure and micro- and nanodiamond-doped silica aerogels. UV/Vis reflectance measurement and fall speed were obtained for the raw microdiamond powder, pure and raw microdiamond-doped silica aerogel, giving the insights on optical properties of prepared samples and their sedimentation speed when dispersed in the atmosphere, respectively.*

### 3.1 Materials and methods

#### 3.1.1 Materials

Raw diamond powder (in size range 0-2  $\mu\text{m}$ , prepared by HPHT, was supplied by Element6), 1-undecene (97 %, Alfa Aesar), IPA (99 %, Sigma Aldrich), zirconia/silica beads (0.1 mm, BioSpec Products), ethanol (absolute, Fisher), TEOS (98 %, Sigma Aldrich), ammonium hydroxide-NH<sub>4</sub>OH (28-30 %, Sigma-Aldrich), ammonium fluoride-NH<sub>4</sub>F (98%, Sigma-Aldrich), and hexane (95 %, Sigma Aldrich) were used in the experiments. DI water was obtained from

Barnstead™ Nanopure™ (Thermo Scientific) for purification with 18.2 MΩ.cm resistivity. The nanodiamond colloid (4 wt%) for this work was provided by NanoCarbon Institute (Japan).

### *3.1.2 Microdiamond functionalization treatment*

The shaking and functionalization treatment of HPHT microdiamonds was adapted from [81], initially used to de-agglomerate and functionalize detonation nanodiamonds with 1-undecene. Raw microdiamond (0.2 g) was mixed with zirconia/silica beads (1 g), 1-undecene (1 ml) and isopropanol (0.5 ml) in a polypropylene vial. The vial is then placed in the shaker (BioSpec Products), where the mixture is shaken for ~ 2 h, with 2 minute break after every 2 minutes of shaking in order to cool down the mixture and avoid 1-undecene polymerization. After that, diamond solution was washed with ethanol and decanted from the beads. Upon drying at room temperature for a week, 1-undecene modified diamond powder was scrapped from the bottom of the vial and collected. Both raw and treated diamond powders had a brown colour. The samples were labelled as a raw microdiamond for the starting microdiamond powder, and 1-undecene-microdiamond for the treated microdiamond powder.

### *3.1.3 Raw microdiamond-doped aerogels*

The silica aerogel samples in this work were prepared according to the adopted procedure from the literature [104] that was used for doping silica aerogels with nickel nanoparticles (NiNPs). Here, silica aerogel was doped with raw microdiamonds (0-2 μm) instead of NiNPs. In short, as-received HPHT microdiamond powder, was added to the mixture solution before gelation, so that the diamond particle concentration in the aerogel precursor was 500 ppm, 700 ppm and 900 ppm (by weight). TEOS was used as a precursor, along with ethanol, and deionised water at a molar ratio of 2:38:39, respectively. Firstly, diamonds were ultrasonicated for 2 (500 ppm) and 4 minutes (700 ppm and 900 ppm) in DI water using Ultrasonic homogenizer Sonopuls HD 3200 from Bandelin. After that, the diamond solution was added to the TEOS, ethanol, and catalyst (molar ratio is  $\text{NH}_4\text{OH}:\text{NH}_4\text{F}:\text{H}_2\text{O}=8:1:111$ ). In terms of the pure aerogel, DI water, TEOS, ethanol, and catalyst, without the addition of diamond, were mixed. After the precursor solution and diamond mixture (30 ml) was sufficiently mixed it was subsequently transferred to a mould and left for about 10 minutes to facilitate gelation. After the hydrogel was obtained, the mould was removed and ethanol was added for aging. After

24 hours, ethanol was exchanged for hexane (500 ml) in the solvent exchange step, by pouring out ethanol and adding hexane, followed by another two hexane exchanges. After the third hexane exchange, the gel was left on a hot plate at 60 °C for 48 h followed by 3 h at 100 °C to dry, after which the aerogel was collected.

The sample labelling is presented in Table 3.1. Two different amounts of catalyst were used to prepare pure silica aerogels. The pristine silica aerogel with 0.5 ml of catalyst was labelled as 'pure silica aerogel' and the doped silica aerogel which contained 500 ppm of the raw microdiamond powder was referred to as '500 R' (prepared with 0.5 ml catalyst as well as the pure silica aerogel). Pure silica aerogel with 0.6 ml of catalyst is used as a reference for 700 R and 900 R aerogels, that were synthesized with the same amount of catalyst. In order to obtain the homogeneous aerogel without sedimentation of diamond particles, the longer sonication time was used with higher concentration of diamonds, as well as higher amount of catalyst to speed up the gelation process. 900 ppm of diamond particles in aerogels was chosen for the optical measurements (Chapter 5.7) because this was the highest achievable concentration of diamonds in aerogels, without sedimentation during gelation process. The pure silica aerogels were transparent, while the doped aerogels appeared milky white. Figure 3.1a and b, c, and d show pure silica aerogel and raw microdiamond-doped silica aerogels, respectively. The final concentrations of microdiamonds in silica aerogels were obtained by XRD (Chapter 5.4).

Table 3.1: Pure and microdiamond-doped silica aerogels with diamond concentration in the precursor and amount of catalyst used to obtain the gel.

Sample	Pure silica aerogel	Pure silica aerogel	500 ppm raw diamond/ silica aerogel	700 ppm raw diamond/ silica aerogel	900 ppm raw diamond/ silica aerogel
Sample code	Pure silica	Pure (0.6 ml cat)	500 R	700 R	900 R
Catalyst amount, ml	0.5	0.6	0.5	0.6	0.6
Diamond conc, ppm	/	/	500	700	900

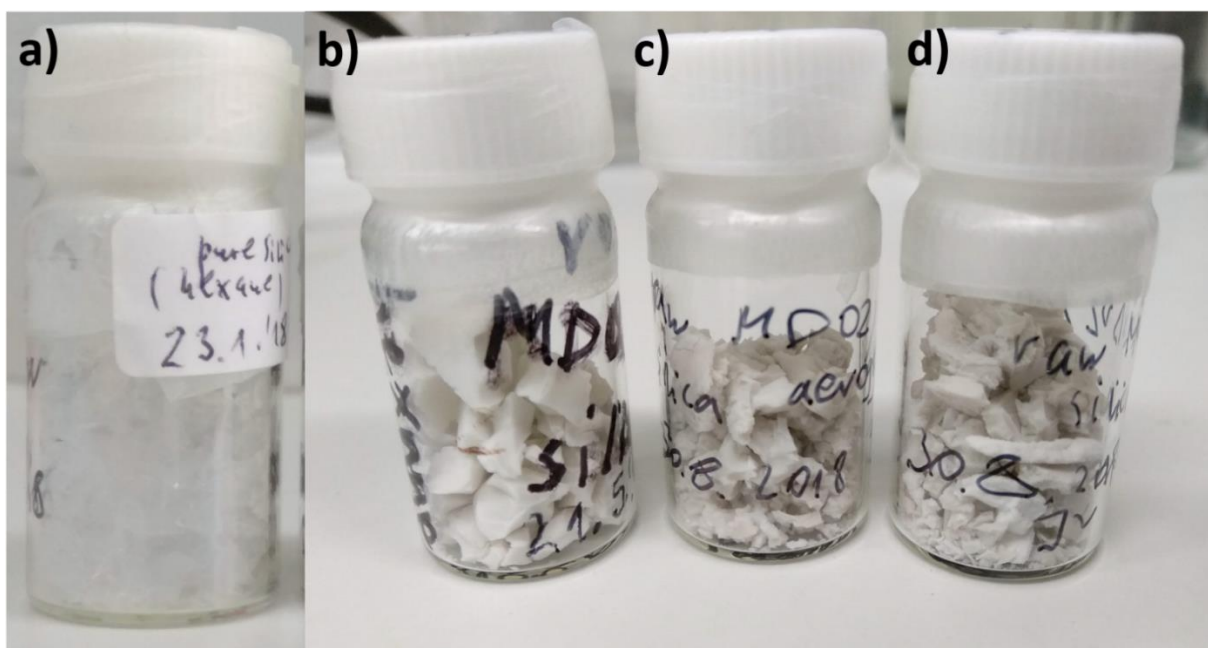


Figure 3.1: a) pure silica aerogel, b) 500 ppm, c) 700 ppm, and d) 900 ppm raw microdiamond-doped aerogel.

### 3.1.4 Nanodiamond colloids

Two samples were examined: 1) the original colloid solution (4 wt%) of nanodiamonds, and 2) 1 wt% colloid solution prepared by adding deionised water to the original solution.

### 3.1.5 Nanodiamond-doped aerogels synthesis

Nanodiamond-doped silica aerogel was prepared using the procedure similar as described in Chapter 3.1.3. In this case, original concentration of 4 wt% (40000 ppm) of nanodiamonds in DI water (see Figure 3.2a) was added to ethanol and TEOS in the precursor solution, so that the final concentration of nanodiamonds in the precursor was 8000 ppm. The catalyst was added (0.5 ml) and the doped aerogel was prepared by gelation, followed by aging, solvent exchange and drying. Figure 3.2b shows nanodiamond-doped silica aerogel. The pure silica aerogel with 0.5 ml was repeated as a reference aerogel for nanodiamond-doped silica aerogel. The final concentration of nanodiamonds in silica aerogel was obtained by XRD (Chapter 6.3.2).

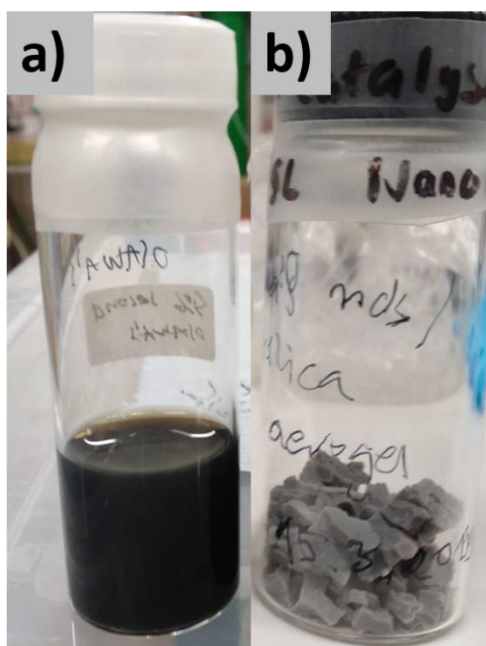


Figure 3.2: a) 4 wt% nanodiamond colloid, and b) final nanodiamond-doped silica aerogel.

## 3.2 Interaction of the electron beam with the matter

Upon interaction of the incident electron beam with a sample, scattering of electrons and emission of photons take place. Scattering can be either elastic or inelastic, while photon emission occurs following absorption of the primary electron beam and excitation of an atom

to a higher energy state. Those emissions include [105]: characteristic X-ray radiation when an electron from the core shell is ejected and the vacancy is filled with another core electron from the higher energy state, or continuum X-rays (Bremsstrahlung), when the primary beam is inelastically scattered, Auger electron, in case a core electron fills the vacancy and the outer shell electron is ejected. In case a vacancy is formed in the valence band, the emission is known as cathodoluminescence (secondary fluorescence), and the emitted photons have the energy of the visible electromagnetic spectrum. Secondary fluorescence occurs when any of the previous emissions become the primary source of the excitation. The depth within specimen from where the discussed photons and electrons are emitted from the sample are presented in Figure 3.3a, along with the possible interaction pathways on an atomic level presented in Figure 3.3b. Later on, some of these interactions will be used for characterization of the prepared samples, and will be therefore closely described [105].

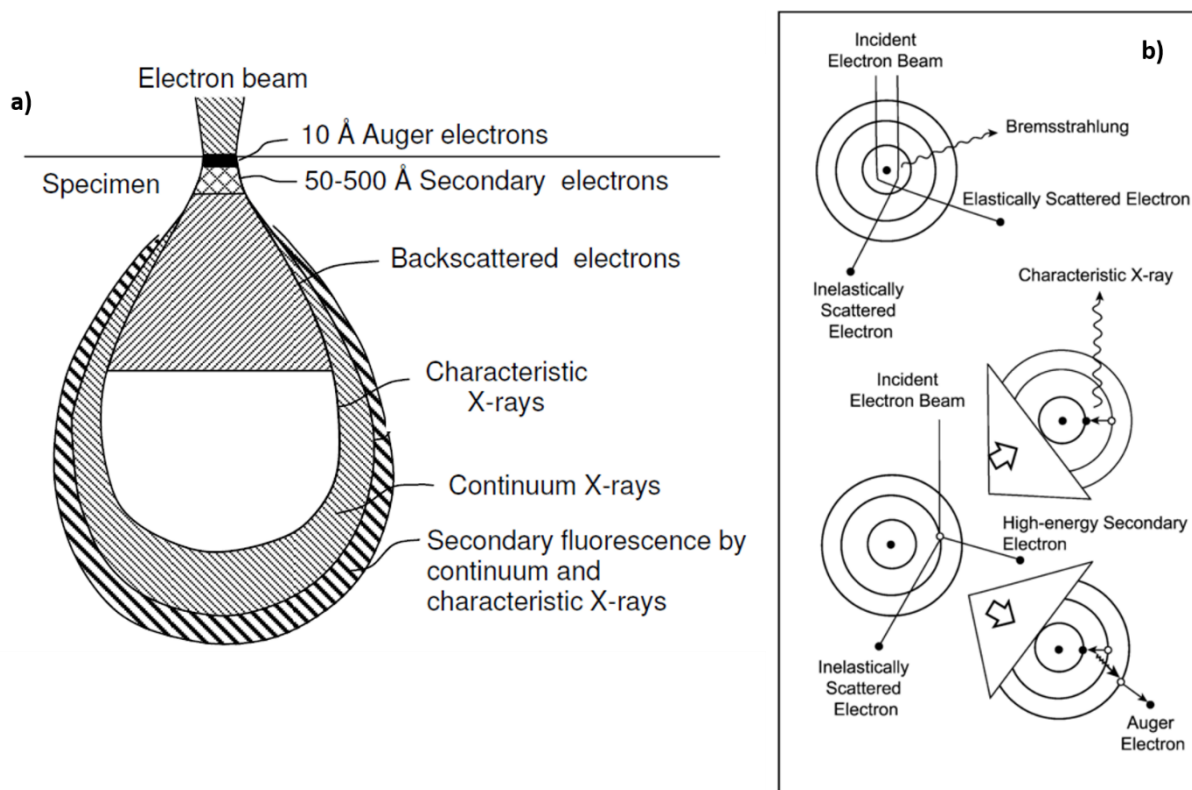


Figure 3.3: Schematic representation of the, a) interaction of the incident beam with a sample, image taken from [105], and b) closer look at atomic level scattering and photon emission upon absorption of the incident beam, image taken from [106].

### *3.2.1 Scanning electron microscopy*

The SEM is utilized for observing and comparing the shape and size of microdiamonds before and after the treatment, as well as observing the surface of the aerogel samples. SEM provides details on morphology and topography only on the localized measured area of the sample. SEM was performed using JEOL JSM-5300LV for the raw and treated microdiamond powders (Chapter 4.1), as well as for the pure silica aerogel in form of a fine powder (Chapter 5.1), in order to observe the diamond particle size and shape before and after the treatment and particle size of a silica aerogel after crushing the obtained aerogel with mortar and pestle. An accelerating voltage of 10 kV was used. High resolution SEM analysis of pure aerogel and raw microdiamond/silica aerogel (Chapter 5.1) was conducted by FEI/Philips XL-30 Field Emission ESEM using a 10 kV accelerating voltage. Prior to imaging, silica aerogel samples were Au coated using BIO-RAD Microscience division SC500 sputter coater.

#### **Principles of operation**

The SEM apparatus contains electron gun, electromagnetic lens system, scanning coils, sample on the sample stage and the imaging system (see Figure 3.4). SEM uses electron gun (thermionic) in order to generate primary electrons. Thermionic gun generates electrons by heating the W or LaB<sub>6</sub> filament, while field emission gun (FEG) generates electrons using the electric field. The value of acceleration voltage is usually up to 30 kV. Electromagnetic lenses system consists of condenser lenses and objective lens and have a role of adjusting the size and focusing the primary generated beam (electron probe). Two or three condenser lenses are usually utilized. Scanning coils allow raster scanning of the sample surface [107].

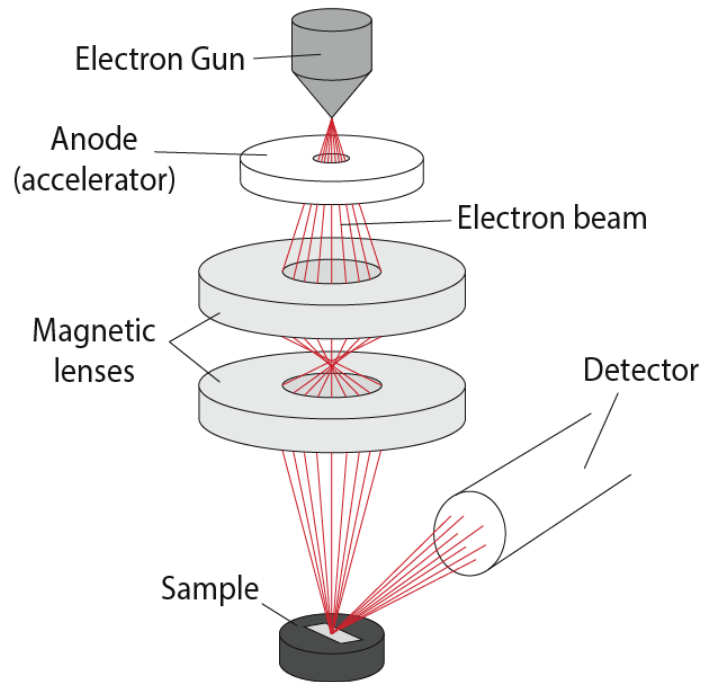


Figure 3.4: Schematic representation of SEM instrument, image taken from [108].

Based on the type of interactions between the bulk sample and the incident electron beam, two categories of electrons are detected: secondary electrons (SE) and backscattered electrons (BSE). Secondary electrons are formed from inelastic scattering of the primary electron beam off the sample, and the resulting secondary electrons are scattered through an angle smaller than  $90^\circ$ . The sample absorbs primary electrons that pass their kinetic energy to electrons in the sample. Some of those electrons will have enough energy to leave the sample (SE). Photomultiplier tube (PMT) is used to detect SE. When primary electrons leave the sample with no or little primary energy loss they are labelled as backscattered electrons and are deflected from the material with an angle that is greater than  $90^\circ$ . Either scintillator-PMT system or solid-state detector are used for BSE [107].

Figure 3.5 represents the kinetic energies of SE and BSE and their relation to kinetic energy of primary electrons  $E_0$ , as well as showing that SE are more likely to occur. Typically, SE are generated at about 50 nm depth, while BSE come from 1  $\mu\text{m}$  depth of the sample [107].

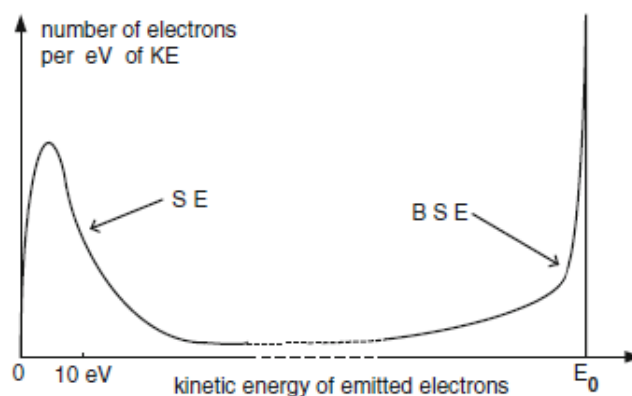


Figure 3.5: The difference in kinetic energy, as well as number distribution, between secondary and backscattered electrons, image taken from [107].

High vacuum is usually needed for SEM imaging in order to avoid interaction of other present molecules with both the primary electron beam and resulting electrons from the sample. In case of electrically insulating samples, coating with a conductive material such as gold or carbon is performed before imaging. Also, surface charging can be avoided by using low vacuum where gas molecules dissipate the negatively charged surface [107].

### 3.2.2 Transmission electron microscopy

The TEM was used to image microdiamonds as well as to observe their doping of silica aerogel. Hitachi HT7800 was used to obtain TEM images of the raw and treated microdiamond powders (Chapter 4.2), and pure aerogel and raw microdiamond-doped silica samples (Chapter 5.2), with a 100 kV accelerating voltage. High resolution transmission electron microscopy (HRTEM) analysis of nanodiamonds (Chapter 6.1.1) and nanodiamond-doped silica aerogel (Chapter 6.3.1) was performed using JEOL 2200FS Ultra high resolution (1Å) with inbuilt Gatan Microscopy Suite® (GMS) software and accelerating voltage of 200 kV. HRTEM was used to image nanodiamonds and their doping to silica aerogel. Additionally, selected area electron diffraction (SAED) and electron energy loss spectroscopy (EELS) were performed for nanodiamond sample for diamond phase identification and for diamond and graphitic carbon detection (Chapter 6.1.2 and 6.1.3, respectively). Samples for TEM and HRTEM were prepared on lacey carbon films on a 300 copper mesh grids. Microdiamond powders and powdered aerogels were dispersed in ethanol and solutions were pipetted on the grid and air-dried. In case of nanodiamond colloids, the original 4 wt% sample was diluted to 0.004

wt% (1:1000) with DI water in order to get good particle distribution on the grid. HRTEM microscopy was performed at York JEOL Nanocentre, University of York.

### **Principles of operation**

The transmission electron microscope (see Figure 3.6) consists of three main elements: The illumination system, the specimen stage and the imaging system [109].

1. Electron source generates an electron beam and then electric field accelerates these electrons (100-300 kV) parallel to the optical axis, through the potential difference established between the cathode and the anode. In general, the anode and the column setup are held at a ground potential, while the cathode is set at a high negative potential. The anode allows the above electrons to pass through, but only if they are not absorbed by the anode. Only 1 % of the electrons generated by the cathode goes through the anode hole and form the TEM beam for analysis. After that, electron beam passes through condenser lens system. There are usually two or more condenser lenses [109].

2. Before entering the vacuum in the TEM column, the sample is inserted in a chamber-airlock. This way the vacuum in the main column is not affected. Specimen itself needs to be thin so that electron beam can pass through it [109].

3. The imaging system contains objective (usually two) and projector (usually four or five) lenses, that have a role of magnifying the image, and the detector (fluorescent screen or a charge-coupled device (CCD)). Two types of imaging can be used, the image and diffraction mode. In the diffraction mode, the image is formed in the back focal plane, while in the imaging mode it is formed in the image plane of the objective lens [109].

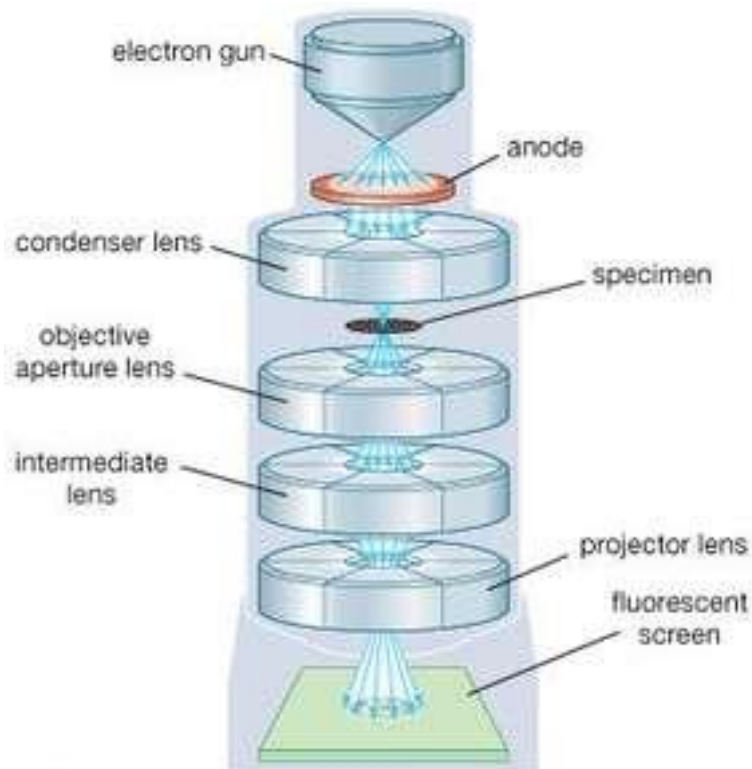


Figure 3.6: The transmission electron microscope, image taken from [110].

### 3.2.2.1 Selected area electron diffraction

Selected area electron diffraction (SAED) is based on the Bragg's law:

$$2d \sin \theta = n\lambda \quad (3.1)$$

which is well known as Bragg's law. The spacing between two adjacent planes is  $d$ , the incident angle is  $\theta$ , the wavelength of X-rays is  $\lambda$  and  $n$  is the order of reflection which must be an integer in order for Bragg's equation to be true [111].

Figure 3.7 shows the formation of the diffraction pattern of a crystalline sample. The incident electron beam is transmitted through the sample. The diffraction pattern consists of bright spot in the middle (from undiffracted electrons) and diffraction spots on the concentric rings (from diffracted electrons). Undiffracted incident beam and diffracted beam will form angle of  $2\theta_B$  and their distance on the diffraction pattern plane will be  $R$ .  $L$  is the camera length, which the distance between the sample and the recording screen [107].

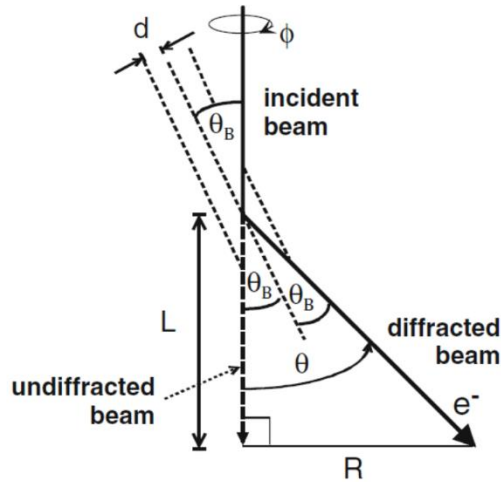


Figure 3.7: Formation of a diffraction pattern on a recording plane, image taken from [107].

From the Figure 3.7, for small diffractions it is true [107]:

$$R = L \tan \theta \approx L \theta \quad (3.2)$$

Also, the Bragg's law (equation (3.4)) can be written as:

$$\lambda = d \theta \quad (3.3)$$

By combining equations (3.5) and (3.6):

$$R d = L \lambda \quad (3.4)$$

Since  $L$  and  $\lambda$  are features characteristic for the instrument, spacing between the planes in the crystal lattice of the sample is  $1/R$ , where  $R$  is the radius of the pattern ring. In a single crystal each spot on the recording plane corresponds to the specific  $d$  spacing and atomic planes. In the case of polycrystalline or nanosized materials this gives rise to continuous ring formation rather than spot diffraction due to random orientations of grains/particles [107].

### 3.2.2.2 Electron energy loss spectroscopy

EELS is based on detection of the inelastically scattered incident electrons. EELS spectrum consists of three regions: zero-loss, plasmon and core-loss spectra (see Figure 3.8). Zero-loss is related to elastically scattered or unscattered primary electrons, while plasmons correspond to interactions between collective excitation of the valence or conduction electrons with the incident beam. The energy loss peak in the third range is characteristic for an element and its electronic state [112].

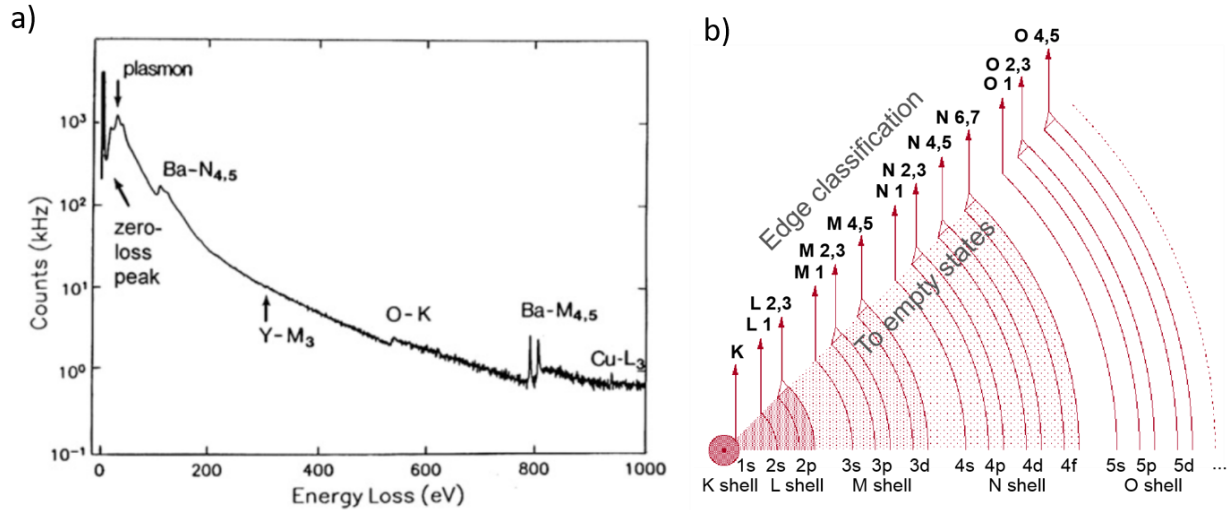


Figure 3.8: a) three EELS ranges for barium, yttrium, oxygen and copper, image taken from [107], and b) core shells, image taken from [112].

In the case of diamond and graphite, which are both carbon-based materials,  $\sigma$  hybridized and  $\pi$  non-hybridized orbitals can be observed. As mentioned in Chapter 2, diamond has four hybridized  $\sigma$  bonds ( $sp^3$  hybridization), while graphite has three hybridized  $\sigma$  bonds and one unhybridized  $\pi$  bond ( $sp^2$  hybridization). Antibonding  $\sigma^*$  and  $\pi^*$  orbitals are unoccupied orbitals with higher energies than bonding orbitals  $\sigma$  and  $\pi$  (see Figure 3.9). When an electron from a core shell absorbs the incident energy of electrons, which is K-shell (1s orbital) in diamond or graphite structure, an electron is promoted to the unoccupied antibonding states. That energy transition has specific energy and it can be used to identify the atom and atom bonding in the sample. Since  $\pi^*$  orbital is positioned at lower energy than  $\sigma^*$  orbital, the corresponding transition into  $\pi^*$  in the K-edge EELS spectrum is shifted to lower energies compared to the transition into  $\sigma^*$  [113].

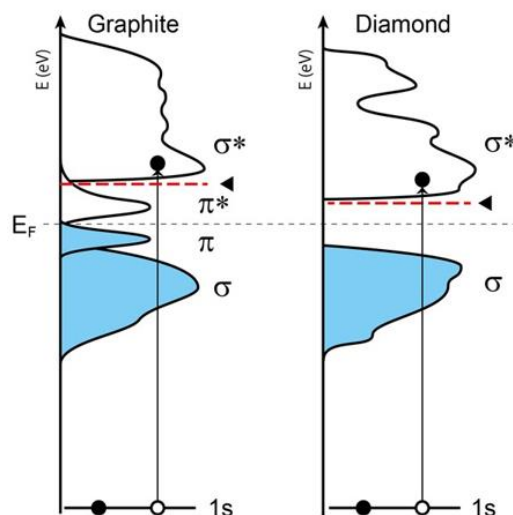


Figure 3.9: Graphite and diamond electronic structures, with bonding and antibonding orbitals, image taken from [113].

### 3.3 X-ray diffraction

XRD is used in this work in order to confirm the crystallinity and purity of the diamond particles and amorphous nature of silica aerogel, as well as to detect the presence and determine the percentage of microdiamonds and nanodiamonds in silica aerogels. XRD patterns of the raw and treated microdiamond powders (Chapter 4.5) and powdered pure and micro- and nanodiamond-doped silica aerogel composites (Chapter 5.4 and Chapter 6.3.2) were obtained by a PANalytical X'Pert Pro diffractometer (with Cu  $\lambda=1.540 \text{ \AA}$ ). Qualitative analysis used for phase identification was done with  $2\theta$  range  $10\text{-}110^\circ$ , step size  $0.03^\circ$  and  $4 \text{ s step}^{-1}$ , while quantitative analysis for obtaining the wt% of diamond in silica aerogels with  $2\theta$  range  $5\text{-}120^\circ$ , step size  $0.03^\circ$  and  $8 \text{ s step}^{-1}$ . The spectra were fitted using HighScore Plus software. The quantitative analysis was performed using Rietveld refinement, where doped-silica aerogels were mixed with silicon internal standard (90 % crystallinity) in ratio sample:standard=90:10 wt%). International Centre for Diffraction Data (ICDD) reference 00-006-0675 was used to identify cubic diamond lattice.

### Principles of operation

- a) **X-ray photons generation:** Collision of high-speed electrons (accelerated from W filament by 30 kV) with a material (Cu target) give rise to X-ray photons (Figure 3.10a) that then initially strike the sample. In that case, both white radiation (which is

removed) and fixed radiation occurs. Broad white radiation is obtained when initial highly accelerated electrons are slowed down during interaction with the Cu material without knocking out electrons. The principle of the X-ray generation is based on ionization of the Cu 1s or K shell electron.  $K_{\alpha}$  occurs in case of 2p to 1s orbital transition with the monochromatic radiation at  $1.5418 \text{ \AA}$ , while  $K_{\beta}$  is produced when an electron from 3p occupies the 1s level at  $1.3922 \text{ \AA}$ .  $K_{\alpha}$  is a doublet and it is more frequent (has higher probability) than  $K_{\beta}$  (Figure 3.10b) [111].

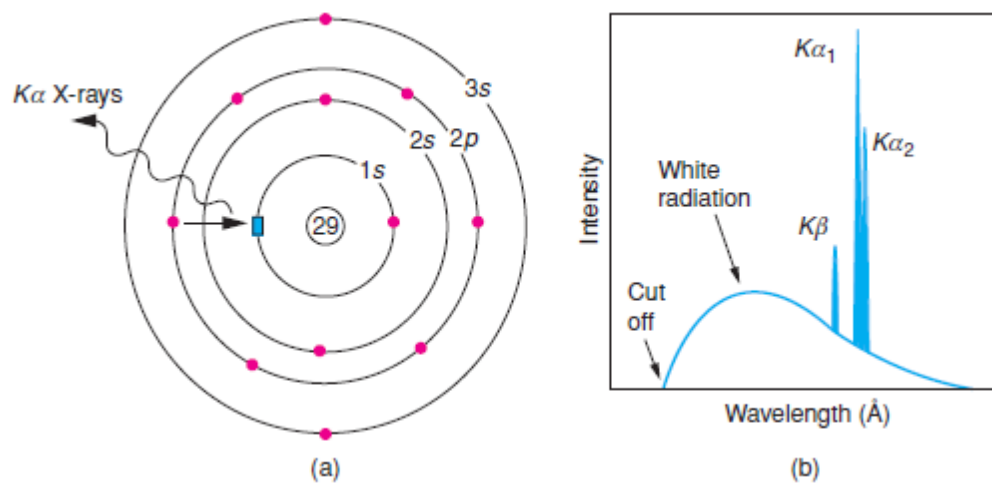


Figure 3.10: a) Cu X-ray formation, and b) Cu X-ray emission spectrum, image taken from [111].

The X-ray tube is protected with Pb, which absorb the X-ray radiation and provides a safe environment around it (see Figure 3.11). The X-ray tube also has Be windows which allows X-rays to escape the chamber and reach the sample for characterization. For obtaining  $K_{\alpha}$  radiation alone and removing  $K_{\beta}$ , Ni is found to be a good filter in case of Cu target [111].

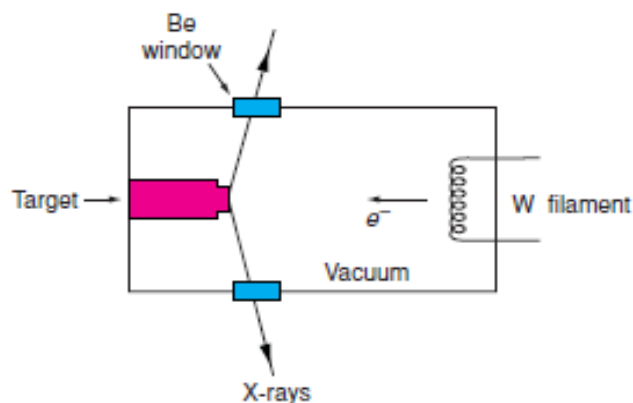


Figure 3.11: X-ray tube, image taken from [111].

**b) Instrumentation:** Bragg's law (equation (3.1)) needs to be fulfilled in order to obtain a signal from a sample. X-ray source, sample stage and X-ray detector are placed on the goniometer where X-ray source and X-ray detector rotate in the way so the X-ray source has an angle of  $\theta$  towards the sample and  $2\theta$  towards the detector (see Figure 3.12). This means that Bragg's angle is changed with rotation but the difference between the two stays the same. In this way, only the beams with the Bragg's diffraction angle are collected. The obtained diffractogram is plotted as intensity against  $2\theta$  [111].

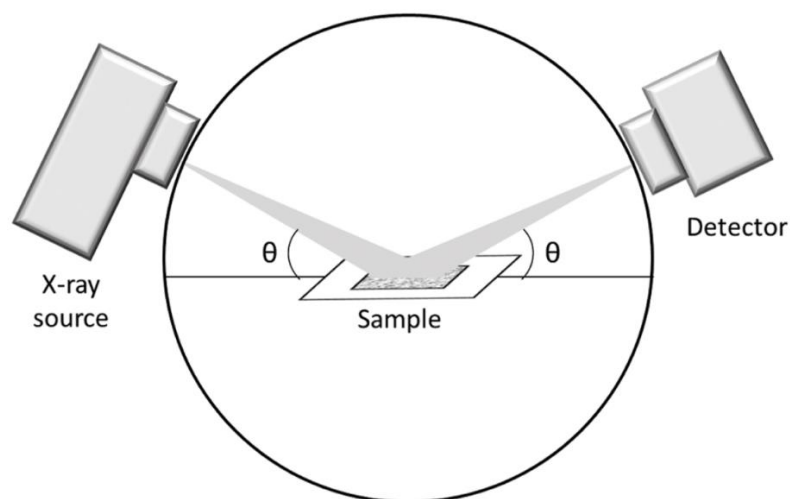


Figure 3.12: Schematic representation of a goniometer, image taken from [114].

### 3.4 Optical Spectroscopies

Optical spectroscopies are used to observe the interaction between electromagnetic radiation and sample. The optical spectrophotometers work with UV, Vis and IR part of the

electromagnetic spectrum. A typical spectrophotometer contains a light source, a monochromator, a sample and a detector (see Figure 3.13). The monochromator consists of an entrance and exit slit for the light beam and a dispersive element in between the two slits. The dispersive element can be either a prism or a diffraction grating, which have a role of dispersing a polychromatic light coming from the light source into a monochromatic light. Rotation of the dispersive element allows different wavelengths to pass through the exit slit. Also, in case of the lower cost spectrophotometers, filters are used to select a specific wavelength [115].

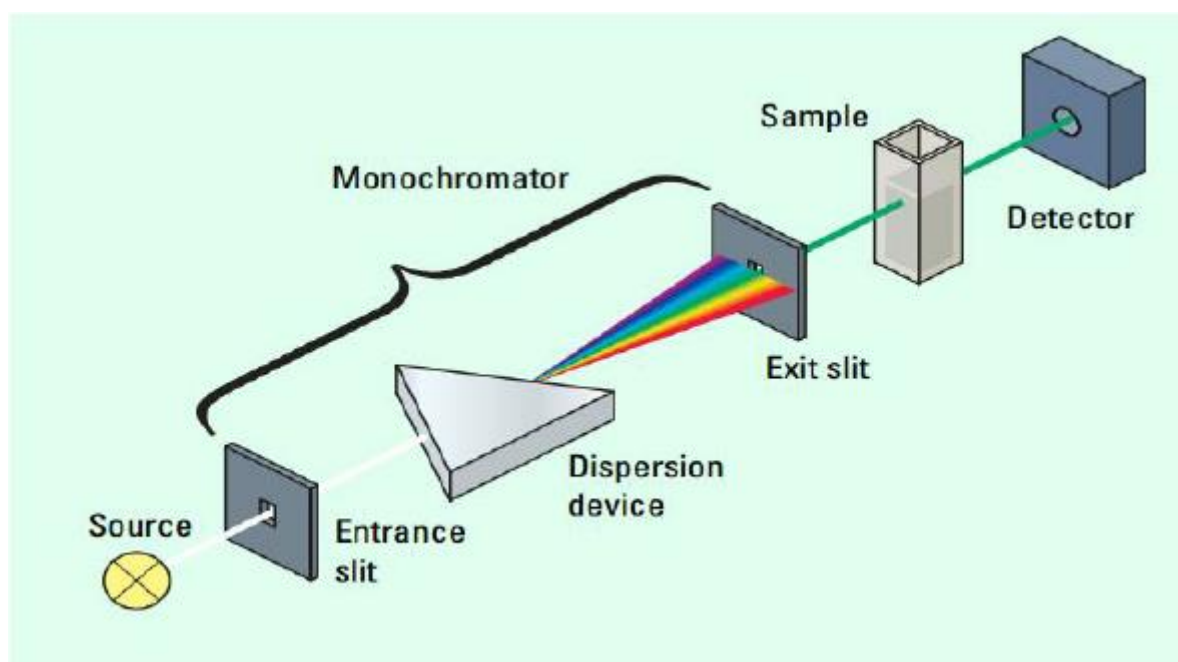


Figure 3.13: Spectrophotometer design, image taken from [116].

### 3.4.1 UV/Visible absorption spectroscopy

UV/Vis absorption is used to measure absorption of nanodiamond particles in the wavelength range that is relevant to solar engineering in term of incoming radiation wavelengths. Original (4 wt%) and diluted (1 wt%) nanodiamond colloids (prepared according Chapter 3.1.4), as well as diluted nanodiamond colloids to 0.2 wt%, 0.25 wt% and 0.3 wt% were measured using Jenway 7315 UV/Visible spectrophotometer in the range 200-1000 nm with 1 nm resolution. Data are presented in Chapter 6.2.1.

## Principles of operation

UV/Vis dispersive spectrophotometer and its components are shown in Figure 3.14. The monochromator disperses the light from the light source (Xenon lamp), which then reaches the sample. The photo diode detector collects the transmitted light. The transmittance is taken as  $T = I/I_0$ , which is the ratio of the transmitted to incident light. Absorbance,  $A$ , can be calculated according to the Beer Lambert law [115]:

$$A = -\log_{10}(T) \Rightarrow A = 2 - \log_{10}(\% T) \quad (3.5)$$

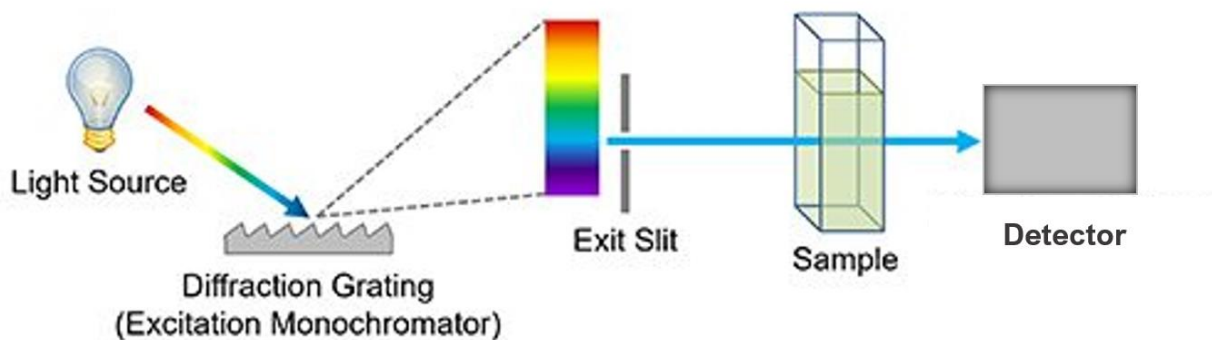


Figure 3.14: Typical UV/Vis dispersive spectrophotometer, image taken from [117].

### 3.4.2 UV/Visible/Near-infrared reflectance spectroscopy

UV/Vis/NIR reflectance can be a useful technique to observe how much of the incident light is reflected from the samples. In solar engineering, it is analogue to back-scattered light as discussed in the Chapter 2. The diffuse reflectance was done by spectrophotometer (Shimadzu SolidSpec-3700 UV-Vis-NIR, 290-2600 nm) using UVProbe software at Northumbria University. The instrument incorporates three detectors as follows: a PMT, InGaAs, and PbS detectors. A slow scan speed and a 20 nm slit width were used during detection. A thin film of fine pure aerogel powder, as well as the pure microdiamond powder and powdered microdiamond-doped composite, were deposited in the cavity of the glass slide and then covered with a glass cover slip prior to the optical measurements being conducted. Detector switch 870 nm and 1650 nm, while diffraction gratings change at 720 nm, which can be noticed in the reflectance spectra of all samples. The spectrophotometer uses double beam mode which allows more accurate measurement. Halogen and deuterium lamps are used as light source. Data are presented in Chapter 5.7.

## Principles of operation

An integrating sphere with a reference and a measurement light are shown in Figure 3.15, as well as a sample and a standard white board. The double beam system consists of a reference and a measurement photon beam, which enables more accurate measurement because the light source fluctuations are compensated for. Barium sulfate coating of the inside of the integrating sphere allows high reflectance of the sphere walls. The standard white board is taken as a reference material as it has high reflectance of the incident light. The reflectance off the sphere walls and the standard white board are taken to have a value of 100 % reflectance. If the incident beam angle is different than  $0^\circ$ , specular reflectance can be measured along with diffuse reflectance. The baseline correction is first recorded without a sample, after which the sample is mounted and the sample reflectance is measured. The detectors are connected to the integrating sphere and optical chopper enables alternating measurement of the reference material and the sample with the samples staying at the same position [118].

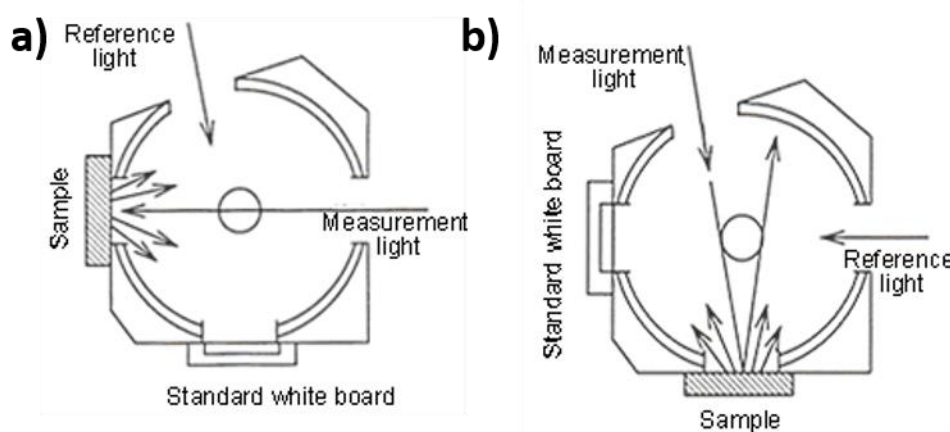


Figure 3.15: Diffuse reflection with integrating sphere: a) without, and b) with specular reflection, image taken from [119].

### 3.4.3 Raman scattering spectroscopy

Hybridization of the diamond particles ( $sp^3$ ) before and after the shaking treatment was investigated by Raman scattering spectroscopy. Raw and treated microdiamonds (Chapter 4.4) were scanned in order to detect any impurities or graphitic  $sp^2$  carbon introduced during the diamond treatment. LabRAM HR800 with a 514.5 nm Ar green laser was used to measure the Raman spectra ( $100-2000\text{ cm}^{-1}$ ) of the diamond powder with 5 s

acquisition time and 3 accumulations, resolution  $3.5 \text{ cm}^{-1}$ . Diamond particles were deposited on silicon wafers from the ethanol suspensions.

### **Principles of operation**

Raman scattering is a technique that measures the shift or change in frequency from incident,  $\nu_0$ , to resulting frequency,  $\nu$  (see Figure 3.16). The incident laser frequency ( $\nu_0$ ) is in the near IR, visible, or near UV, and the resulting signal is collected at  $90^\circ$  angle to  $\nu_0$  [120]. In case of normal Raman scattering three events can occur upon material's interaction with a monochromatic light. Firstly, Rayleigh scattering that is elastic, so the incident beam does not lose its energy. Raman Stokes scattering occurs when the resulting frequency is lower than  $\nu_0$ , while Raman anti-Stokes scattering is obtained in case of the enhanced resulting frequency compared to the  $\nu_0$ . The general Raman frequency for inelastic scattering is:

$$\nu = \nu_0 \pm \nu_m \quad (3.6)$$

Where  $\nu_m$  is Raman shift that either adds to  $\nu_0$  (anti-Stokes) or subtracts from  $\nu_0$  (Stokes) [120].

Stokes scattering signal is stronger and hence more commonly recorded since the population in the zero vibrational state is more populated than the first vibrational state of the electronic ground state [120].

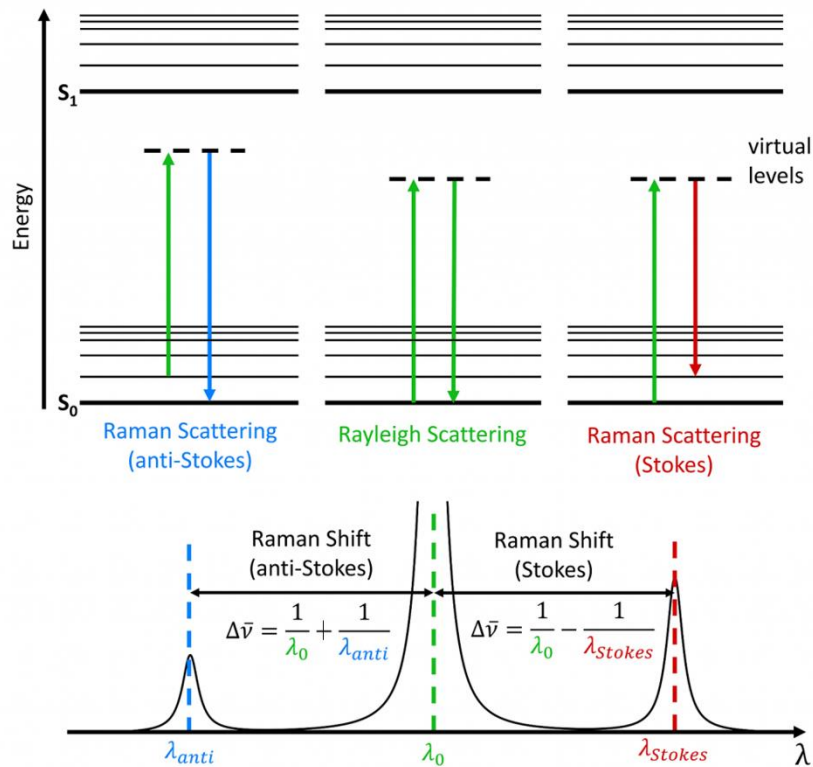


Figure 3.16: Raman scattering, image taken from [121].

The light source in Raman spectrometer is a laser (see Figure 3.17). The Raman shift does not depend on the light source wavelength. The detection system is CCD spectrograph. Before reaching the diffraction grating, the beam passes through filters, so only the Stokes scattering or desired wavelengths are measured [117].

Diamond does not possess an intrinsic bulk electric polarisation, and only change in polarizability can arise. In diamond Raman spectrum, sharp peak appears at  $1332 \text{ cm}^{-1}$ , and hence this is considered a good technique for diamond quantitative and qualitative analysis [122].

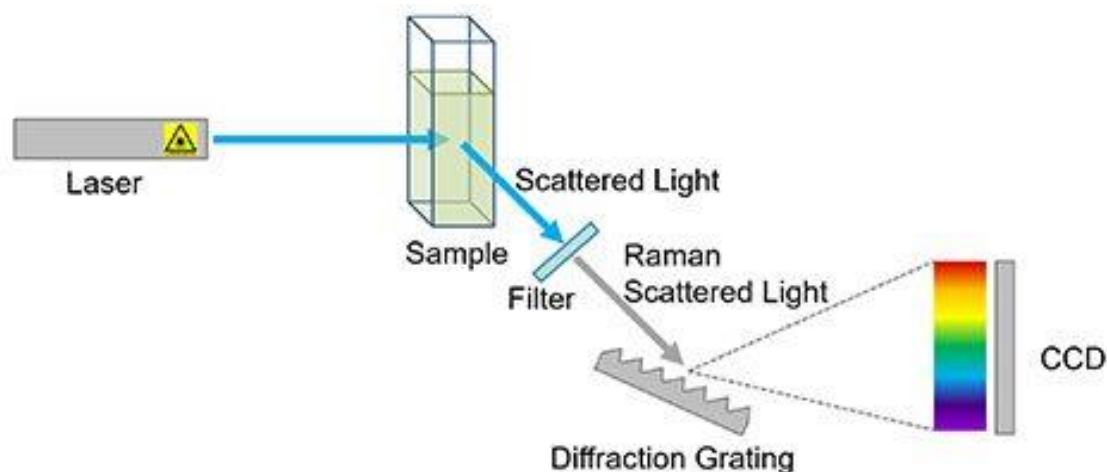


Figure 3.17: Typical Raman spectrometer, image taken from [117].

#### 3.4.4 Fourier transform infrared spectroscopy

FTIR spectroscopy was done aiming to investigate the surface and the presence of the surface groups on the raw and the treated microdiamond powders (Chapter 4.6). Also, identification of silica aerogel structure was recorded for the pure and microdiamond-doped silica aerogels (Chapter 5.3). Powdered aerogels and microdiamond powders were placed on the ATR diamond using IRAffinity-1s Spectrophotometer (Shimadzu), with  $4\text{ cm}^{-1}$  resolution, 100 scans, in the range  $500\text{-}4000\text{ cm}^{-1}$ , using absorbance mode for diamonds or transmittance mode for silica aerogels.

#### Principles of operation

The main part of the FTIR spectrometer is the Michelson interferometer. An IR source, which is a single wavelength ( $\lambda$ ), reaches a beam splitter in the interferometer (see Figure 3.18). Here, 50 % of the incident light gets reflected towards the fixed mirror, and another 50 % gets transmitted towards the movable mirror. The movable mirror can change its position forward and backwards. Beams from both mirrors then partially go back to the source and partially towards the sample and the detector, so that these two beams combine together again. The difference in covered distance (optical path difference- OPD) is labelled as  $\delta$ . In case  $\delta = 0$ , the beams had travelled the equal paths and they are in phase and interfere constructively. Conversely, when  $\delta = \lambda/2$ , then the signal vanishes completely as the interference is destructive. The resulting interferogram is a cosine function [123]:

$$I(\delta) = B(\nu) \cos 2\pi \frac{\delta}{\lambda} \quad (3.7)$$

where  $I$  is intensity of the signal at the detector and  $B$  is the source brightness [123].

From here, it is possible to obtain a spectrum (absorbance or transmittance) by using Fourier transform. Transmittance is detected and absorbance can be plotted against frequency following Beer Lambert law (see Chapter 3.4.1, equation (3.8)) [124].

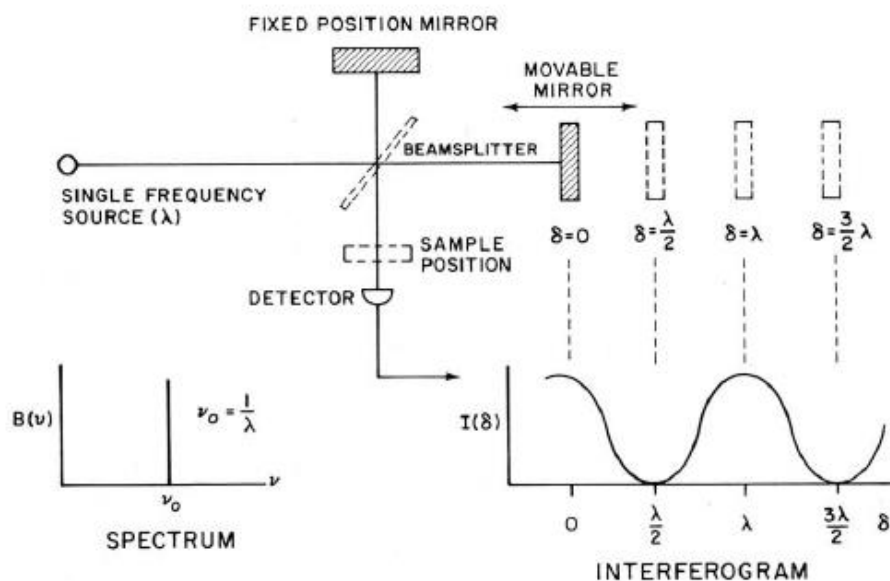


Figure 3.18: Schematic representation of FTIR spectrometer, image taken from [123].

Another approach of getting a FTIR spectrum is by using an attenuated total reflectance (ATR), known as ATR-FTIR. It does not require sample preparation. The ATR crystal is a material with a high refractive index such as zinc selenide (ZnSe), germanium (Ge) or diamond. The IR beam passes through the ATR crystal as an evanescent wave based on the total internal reflection until reaching the detector. If the sample absorbs IR then it would make changes to the signal as it becomes attenuated. Figure 3.19 shows the incoming beam, sample, ATR crystal, penetration depth ( $d_p$ ) (usually about  $2 \mu\text{m}$ ), critical angle for internal total reflection ( $\theta$ ) and the refracted beam. The refractive index of the ATR crystal must be higher than that of a measured sample [125].

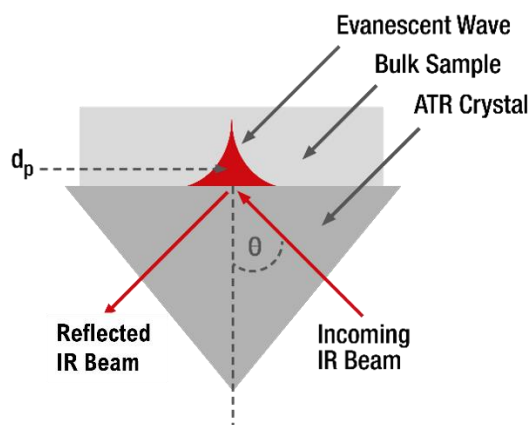


Figure 3.19: ATR crystal with evanescent wave, penetration depth,  $d_p$ , and critical angle  $\theta$ , image taken from [125].

### 3.5 Nuclear magnetic resonance spectroscopy

NMR obtains the structural information of carbon and hydrogen bonding in the measured sample. Solid-state NMR measurement was recorded for the raw and treated microdiamond powders (Chapter 4.7.1 and 4.7.2), while the solution-state NMR was performed for the 1-undecene solution (Chapter 4.7.3). Solution-state  $^{13}\text{C}(^1\text{H})$  NMR spectrum of the 1-undecene was recorded on a Bruker Avance III HD 700 MHz NMR Spectrometer equipped with a TCI Prodigy™ Cryoprobe. The  $^{13}\text{C}$  operating frequency was 176.07 MHz and the sample was measured at 298 K in deuterated chloroform ( $\text{CDCl}_3$ ). Solid-state  $^{13}\text{C}(^1\text{H})$  NMR spectra were recorded on a Bruker Avance III HD 500 MHz NMR spectrometer operating at 125.78 MHz. Spectra were obtained using cross-polarisation and relaxation delay of 4 s. The magic-angle spinning (MAS) experiment was done for carbon atoms with spin rates of 6 kHz. Chemical shifts are quoted in ppm relative to tetramethylsilane.

#### Principles of operation

NMR spectroscopy operates in the range 3-30 000 MHz of radio waves and it is used to observe magnetic transitions within magnetic energy levels of nuclei in molecules. Isotopes with either odd mass number or/and odd atomic number,  $I$ , have net nuclear spin and are NMR active. Proton NMR ( $^1\text{H}$  NMR) and carbon-13 NMR ( $^{13}\text{C}$  NMR) with half-integer nuclear spin ( $1/2$ ) are widely used to characterize organic compounds. Regarding the carbon isotopes, its most abundant  $^{12}\text{C}$  (98.9 % in nature) is undetectable by NMR having the nuclear spin of

zero. Carbon isotope  $^{13}\text{C}$  exhibiting about 1.1 % abundance in nature results in weak signal compared to  $^1\text{H}$  NMR [115].

This spectroscopic method is based on alignment (either parallel or antiparallel) of magnetic nuclei in the presence of an external magnetic field. While the nuclei oriented parallel or aligned with the field will have  $+1/2$  spin ( $\alpha$  spin state), the ones oriented antiparallel or aligned against the field will have  $-1/2$  spin ( $\beta$  spin state). Also,  $\beta$  spin state is higher in energy. The transition frequency,  $\nu$ , is [115]:

$$\nu = \frac{\gamma H_0}{2\pi} \quad (3.8)$$

where  $H_0$  is the applied magnetic field, and  $\gamma$  is the gyromagnetic ratio (nuclear constant), with relations to magnetic moment,  $\mu$ , as:

$$\gamma = \frac{2\pi\mu}{hI} \quad (3.9)$$

where  $h$  is Planck's constant. This leads to:

$$\nu = \frac{2\mu H_0}{h} \Rightarrow h\nu = \Delta E = 2\mu H_0 \quad (3.10)$$

showing that  $\Delta E$  (energy between  $\alpha$  and  $\beta$  states) increases with stronger  $H_0$ .

The transition frequency,  $\nu$ , is also called precessional frequency since the rotating axis of the spinning nucleus forms a precessional orbit perpendicular to applied field,  $H_0$ . Also, the magnetic transition is known as flipping of the nucleus due to flipping to the perpendicular direction of the applied field. This occurs using the field oscillator. Therefore, when the rotating magnetic field and precessional frequency are resonant, the transition from the lower to higher magnetic state happens [115].

Shielding and de-shielding happens depending on whether the H atom is close to an electronegative atom. In the case of de-shielding, the electronegative atom attracts electrons around H atom and decreases the magnetic field that those electrons would generate shifting the signal downfield. Alternatively, the signal position moves upfield towards the reference (zero) because it is more difficult to pick up the signal where surrounding atom increases the electron density and perturbs the proton signal [115].

In NMR spectroscopy, usually tetramethylsilane (TMS) is used as reference because it is chemically inert and has higher upfield absorption than other peaks recorded due to protons being shielded by Si atoms. The spectrum is plotted as parts per million  $\delta$  compared to the zero position of TMS [115].

The magnet generates the magnetic field, while the sweep generator is used in order to vary the magnetic field (see Figure 3.20). The sample is placed in the glass tube and irradiated by the radio frequency obtained from the oscillator. Sample holder is spun to ensure the magnetic field is applied homogeneously. When  $\Delta E$  and the incident frequency are resonant for the given  $H_0$ , the transition  $\alpha$  to  $\beta$  spin state takes place generating electric current in the radio frequency receiver when the magnet flips back to previous position. The receiver sends the electric signal to the detector where it is amplified and recorded as the intensity against the value of the chemical shift [115].

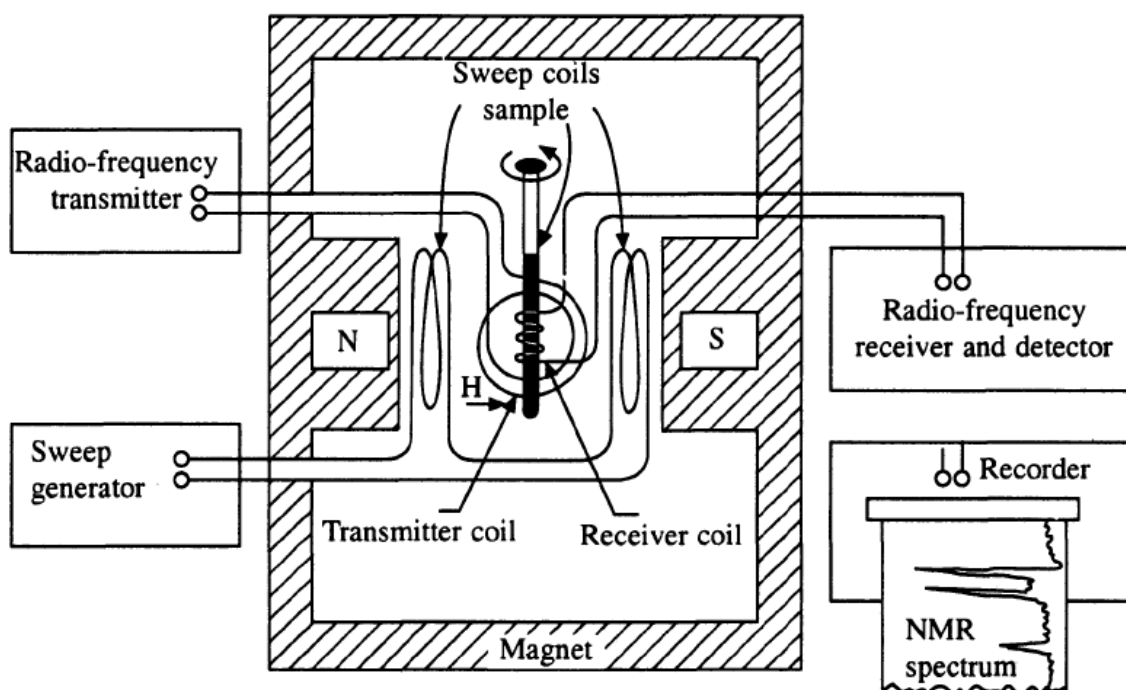


Figure 3.20: Schematic representation of an NMR spectrometer, image taken from [115].

In order to decrease the effect of anisotropy during the measurement of solid samples and enhance the signal, either magic-angle spinning (MAS) or cross-polarization (CP) is used. With MAS technique, a nucleus is spun at the magic angle ( $54.74^\circ$ ) with radio frequency. Also, CP is based on energy transfer from the excited and more abundant nuclei (protons) to the less

abundant nuclei (carbon 13). Therefore, the signal enhancement from protons is used in case protons are present in the sample.

### 3.6 Dynamic light scattering

Particle size distribution, as well as the Zeta potential, is measured using DLS theory. The size of the raw and treated microdiamonds (Chapter 4.3) and nanodiamonds (Chapter 6.2.3) was assessed by DLS using Zetasizer Nano ZS (Malvern Instruments). The microdiamond powders were dispersed in DI water, while original (4 wt%) and diluted (1 wt%) nanodiamond colloid (obtained from NanoCarbon Institute (Japan)) were measured as prepared, the DLS size measurement was conducted at 25 °C with a 175° scattering angle. The number of measurements was set to 3 with each measurement taking up to 30 runs. The Zeta potential and pH of the nanodiamond colloids for both 4 wt% and 1 wt% were measured (Chapter 6.2.2), where Zeta potential was an average of 3 measurements. DLS size measurement, Zeta potential and pH are measured within 24 h on day 1 and day 6 after opening the original 4 wt% stock bottle, and the diluted (1 wt%) colloid was prepared on each day from the stock bottle of the original colloid.

#### **Principles of operation**

The dynamic light scattering is used to determine the particle size distribution present in the sample. The main principle is based on illumination of the particles with a laser and recording the scattered light. Movement of the particles suspended in the liquid occur due to the random collision of the particles with liquid molecules which is known as the Brownian motion. Also, smaller particles move quicker than large particles. The light from the particles is scattered in all directions and the intensity of the measured light depends on the interference (constructive or destructive). For constructive interference, the maximum intensity of the light is recorded, while in the maximum destructive interference lead to the signal being cancelled out [126].

Due to Brownian motion, the intensity of the signal fluctuates in a single point. The correlation between two signals at different times will be more or less the same. Strong correlation is taken as 1 and no correlation as 0. For example, two signals will be correlated if the time between their collections is very short (nano- or microseconds). With an increasing time between two signals, the correlation between them will decrease. Eventually, it takes 1 to

tens of milliseconds for correlation to diminish to zero, where the signals are not related to each other anymore (see Figure 3.21).

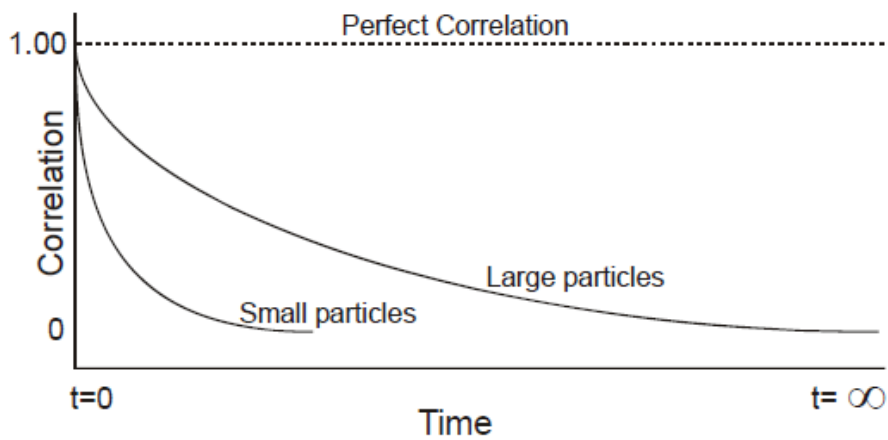


Figure 3.21: The correlation function for small and large particles, image taken from [126].

The DLS measurement gives a particle size distribution plot and Z-average particle size ( $D_z$ ) [127]:

$$D_z = \frac{\sum S_i}{\sum \frac{S_i}{D_i}} \quad (3.11)$$

which is the harmonic mean and where  $D_i$  and  $S_i$  are diameter and intensity of the scattered light for particle  $i$ , respectively. In case the polydispersity index (PDI), which is the parameter of measurement reliability, is in the range 0.1-0.5, Z-average is commonly used. However, Z-average is not reliable for polymodal distribution with PDI greater than 0.5 [126]), then mean particle size from the distribution plot is used.

The instrument (see Figure 3.22) consists of laser source (1)- Zetasizer Nano ZS uses HeNe laser (632.8 nm) and backscatter detection (3). Backscatter 175° detection is usually preferred over 90° because of the higher probability of collecting a beam due to shorter distance and avoiding the passage through the whole sample. The sample is held in a cuvette (2), and after interaction with the sample, the resulting signal is collected. It is processed in a correlator and computer (5 and 6). Attenuator (4) has a role of attenuating the laser light in case the sample scatters light that is too intense for the detector [126].

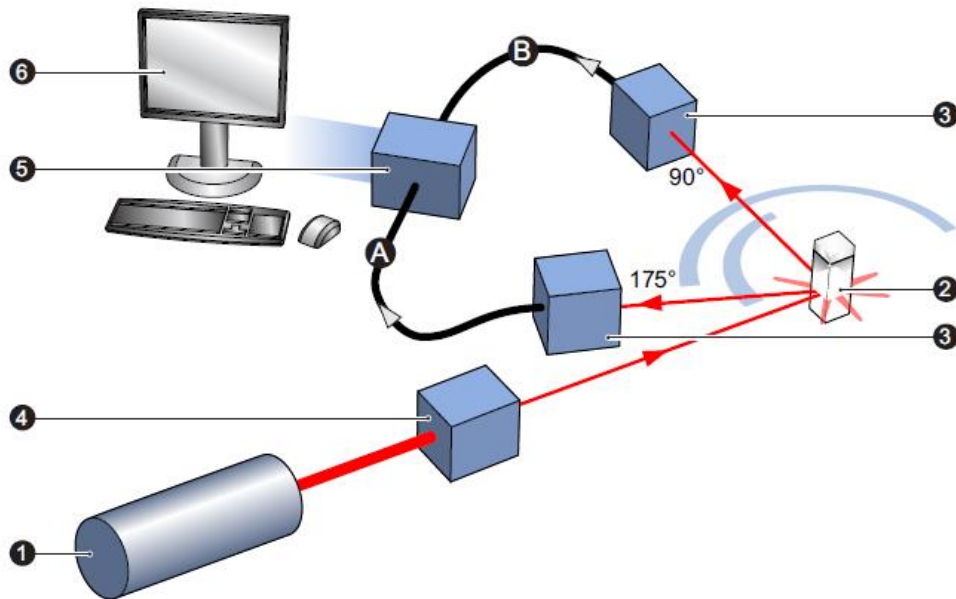


Figure 3.22: Schematic representation of Zetasizer, image taken from [126].

### 3.6.1 Zeta potential measurement

The charged particles move due to the applied electric field in the liquid. This phenomena is known as electrophoresis. The velocity of particles that are moving, and is induced by an electric field is electrophoretic mobility. A measurement cell (folded capillary cell) contains two opposite electrodes (see Figure 3.23). Potential difference is applied and the movement of the particles towards the opposite charge (electrode) occurs. Particles scatter the light from the laser source [128].

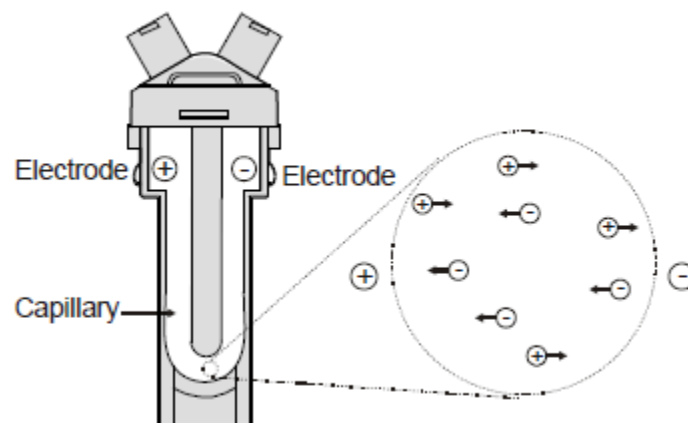


Figure 3.23: Folded capillary cell used for Zeta potential measurement, image taken from [126].

Using laser Doppler velocimetry (LDV), mobility of the particle can be related to frequency rate of the scattered light. The Doppler shift is the change in frequency of the scattered light from a moving particle. The scattered beam is combined with the reference beam (see Figure 3.24). The signal is fluctuating proportionally to the particle velocity [129].

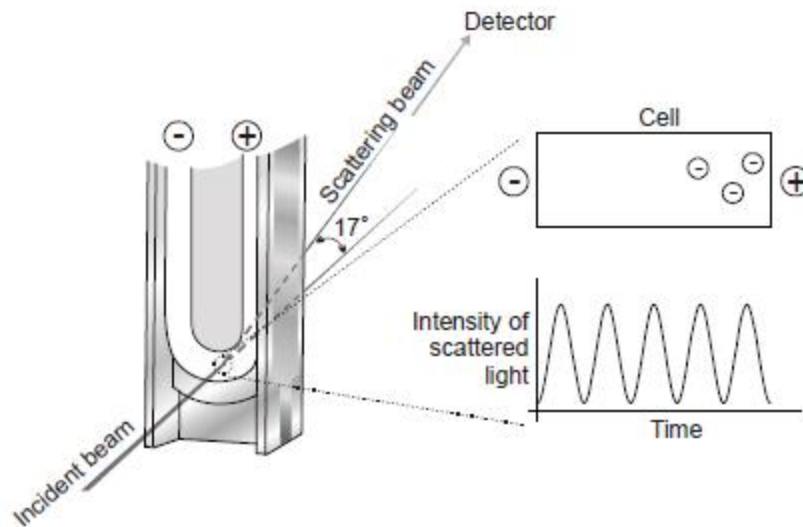


Figure 3.24: Signal generation, image taken from [126].

### 3.7 Brunauer-Emmett-Teller and Barrett-Joyner-Halenda theories

The specific surface area, pore size distribution and pore volume of the pure (0.5 cat) and raw microdiamond-doped silica aerogels (Chapter 5.5) were determined on a ThermoScientific Surfer system at Newcastle University, while the pure (0.6 cat) (Chapter 5.5), repeated pure (0.5 cat) and nanodiamond-doped silica aerogel (Chapter 6.3.3) were measured on a Micromeritics ASAP 2020 instrument at Warwick University at 77 K using nitrogen gas. The samples were outgassed under high vacuum at 200 °C for 12 h prior to the sorption measurements. The BET equation was used to calculate the specific surface area, while BJH method on the desorption branch of the isotherm was used to calculate the pore volume and pore size distribution. Bulk densities were measured as a ratio of the weight to volume followed by porosity calculations for all silica aerogels (Chapter 5.6 and Chapter 6.3.4).

#### Principles of theory

Brunauer et al defined five types of adsorption isotherms according to their experimental data in 1940 and later on in 1985 IUPAC [130] updated the classification by adding the sixth

isotherm (see Figure 3.25). Isotherms represent the amount of the adsorbed gas against the pressure of the gas at the constant temperature [131].

Type I isotherm is related to either microporous material or chemisorption (the Langmuir isotherm) (see Figure 3.25a). Type II and III isotherms correspond to either non-porous or macroporous material with strong or weak fluid-wall attractive forces, respectively. Type IV and V isotherms are modifications of type II and III isotherms for mesoporous materials, respectively. The difference between type II and IV, and III and V, is that type IV and type V isotherms exhibit hysteresis loop (difference in adsorption and desorption curves) associated with additional capillary condensation along with physical adsorption. Some materials with strong adsorption show type VI isotherm, with layer-like adsorption [130]. Figure 3.25b represents the area accessible to the measurement.

Type I, II and III isotherms are reversible. Type IV and V show hysteresis loop that is related to capillary condensation in mesopores. There are four types of hysteresis loops classified by IUPAC named H1, H2, H3 and H4 (see Figure 3.25c). H1 indicates regular porosity (with cylindrical-like pores) without interconnecting channels. On the other hand, pore size distribution and shape are not well-defined in case of H2. Presence of 'ink bottle' pores and interconnectivity are common features for H2. Slit-like pores obtained in the structure with plate-like particles give H3, while H4 indicates narrow slit pores (microporosity) [132, 133].

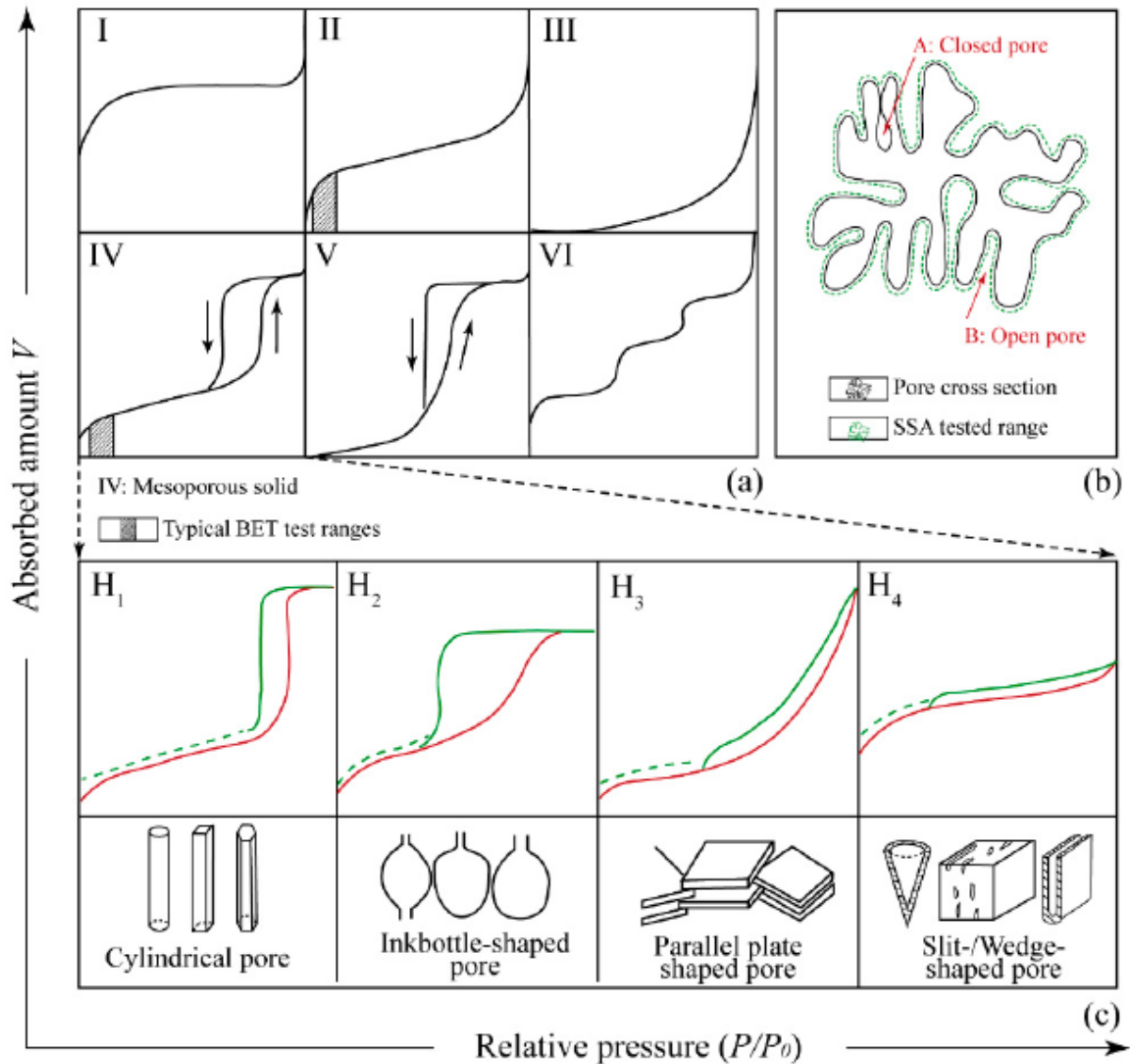


Figure 3.25: a) Six types of adsorption isotherms, b) surface area measurement range, and c) hysteresis loop types, image taken from [134].

**BET theory:** Langmuir's theory is based on chemisorption of a monolayer on the adsorbent surface and further layering does not occur. Brunauer et al derived the BET equation by generalizing Langmuir's theory to multimolecular adsorption:

$$\frac{p}{v(p_0 - p)} = \frac{1}{v_m c} + \frac{(c-1)}{v_m c} \frac{p}{p_0} \quad (3.12)$$

which is essentially  $\frac{p}{v(p_0 - p)}$  as y-axis against  $\frac{p}{p_0}$  as x-axis with  $\frac{1}{v_m c}$  as intercept and  $\frac{(c-1)}{v_m c}$  as slope of the plot (see Figure 3.26).  $p$  and  $p_0$  are applied and saturation

pressure, respectively,  $v$  the total volume of gas adsorbed,  $v_m$  the volume of adsorbate when monolayer is complete, and  $c$  is a constant.

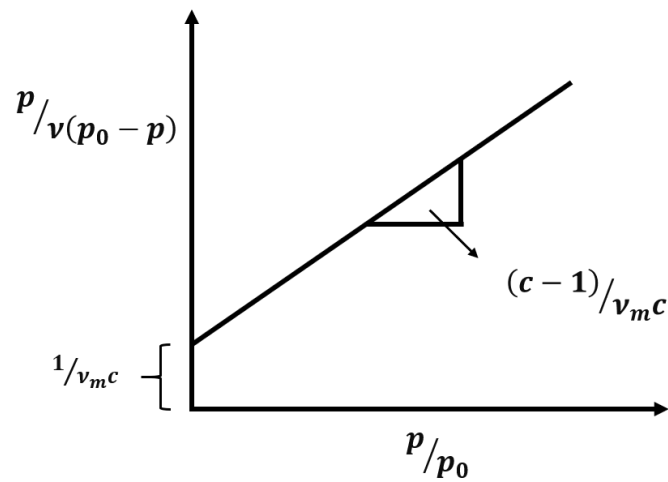


Figure 3.26: BET plot.

Brunauer et al has shown that the best match between experimental and theoretical data is in the 0.05-0.35 region of relative pressure,  $p/p_0$ , where the theoretical (BET) plots are linear [135].

Specific surface area,  $S_{BET}$  equals to surface area of adsorbent,  $A_s$ , divided by the mass of adsorbent ( $m$ ):

$$S_{BET} = \frac{A_s}{m} = \frac{n_m N_A A_0}{m} = \frac{v_m N_A A_0}{v_g m} \quad (3.13)$$

where  $n_m$  is the number of moles of adsorbate in a monolayer,  $N_A$  is Avogadro's number ( $6.022 \cdot 10^{23}$ / mol) and  $A_0$  is the cross-sectional area of the adsorbate molecule. In case of nitrogen as adsorbate,  $A_0$  is  $0.162 \text{ nm}^2$ .  $v_g$  is the molar volume of adsorbate.

**BJH theory:** It assumes that physical adsorption occurs on the pore walls and capillary condensation takes place in the 'inner capillary volume' [136].

This can be accomplished by introducing the following assumption: all capillaries are cylindrical and those with the same size behave the same during desorption. An average radius of  $\bar{r}_c$ , is between the radius value at upper and lower relative pressure (see Figure 3.27). In other words, the average capillary radius,  $\bar{r}_c$ , is average value of capillary radius before,  $r_{n-1}$ , and after,  $r_n$ , desorption. If  $\bar{r}_p$  is the radius of the pore, during the  $n$ -th step of

desorption (when  $(p/p_0)_n$  is applied),  $\Delta t_n$  will be the thickness of the physically adsorbed layer that is desorbed at the corresponding relative pressure. Also, during the  $n$ -th step of desorption, the thickness of the adsorbate layer is  $t_{\bar{r}}$  [136].

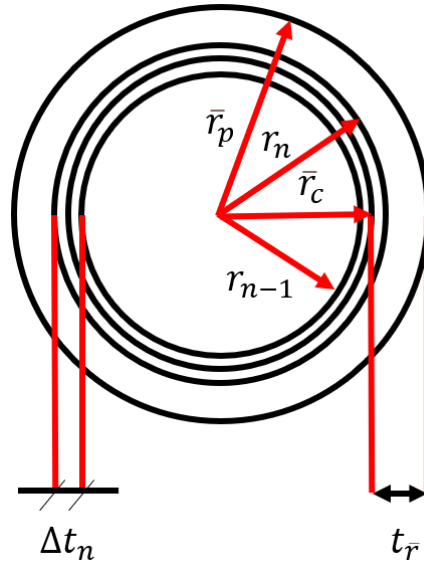


Figure 3.27: Relationship between the pore and the capillary radius, image taken from [136].

BJH theory uses Kelvin equation [136] to calculate the capillary radius,  $r_k$ :

$$RT \ln(p/p_0) = -2\gamma \frac{v_g}{r_k} \Rightarrow \log(p/p_0) = \frac{-2\gamma v_g}{2.303RT r_k} = \frac{-4.14}{r_k} \quad (3.14)$$

where  $\gamma$  is the liquid nitrogen surface tension.

The apparatus for surface analysis consists of two parts: degasser and analyser. During the degassing step, a blank burette is degassed first (with mass  $m_1$ ) and then a sample is added to the burette. The burette with the sample is sent to degassing at appropriate temperature to evaporate any moisture that sample took up, after which the mass of the tube with the degassed sample is measured ( $m_2$ ). It follows that the mass of the sample after degassing,  $m = m_2 - m_1$ . After that, burette with a sample is placed in the analyser and the nitrogen isotherm of sample is measured.

The density of diamond particles is taken to be  $3.51 \text{ g/cm}^3$  [8]. Silica aerogel has a skeletal density of  $2.65 \text{ g/cm}^3$  [137], which is the ratio of the mass per volume of the solid silica backbone. The bulk density of silica aerogels is calculated as the ratio of the mass per volume of the silica sample. Porosity of a silica aerogel was calculated using the formula below [41]:

$$P(\%) = \left(1 - \frac{\rho_b}{\rho_s}\right) 100 \quad (3.15)$$

where  $\rho_b$  and  $\rho_s$  are the bulk and skeletal density of the silica aerogel, respectively.

### 3.8 Fall speed

The fall speed is used in the Chapter 5.6 for assessing the time before sedimentation of the raw microdiamond powder, pure and microdiamond-doped silica aerogel when these particles are injected in air, according to the equation 2.5 in Chapter 2.1.4.

### 3.9 Conclusion

Chapter 3 contains details on materials used in this work along with the procedures carried out to treat the HPHT microdiamond powder and synthesize aerogels. Also, the principles behind the characterization methods of the prepared samples, as well as the conditions of the measurements, are briefly described. SEM and TEM were used for assessing the size and shape of diamond particles, while DLS was used to obtain information on particle sizes. Additionally, the surface of diamond particles was examined by FTIR and NMR spectroscopy, while Raman spectroscopy was used to detect graphite phase on diamond particles. Zeta-pH measurement was done in order to assess the stability of nanodiamond colloids. XRD was utilised to identify the presence of the diamond phase in the diamond-doped aerogels. Aerogels were also assessed by BET and BJH, skeletal and bulk density, and porosity measurements. The diffuse reflectance was used to characterize raw microdiamonds, pure aerogel and raw microdiamond-doped aerogel fine powders, while the fall speed was calculated in order to evaluate the diamond-doped silica aerogel composite for use as solar scatterers.

## Chapter 4 Raw and 1-undecene-treated microdiamonds

*Diamond particles are suggested [6, 8] to be very good solar scatterers and high quality of diamond would ensure the efficient utilization of optical properties. Also, diamond functionalization could be useful in various applications including the field of luminescence. In this chapter the results of the characterization of the raw and 1-undecene-treated HPHT microdiamond powders are presented with the aim to access the size and shape of diamond particles, as well as to investigate the surface and purity/contamination of the diamond powders including presence of  $sp^2$  graphitic carbon. The ultimate goal is to compare the two microdiamond powders and access whether the shaking treatment with beads could be used in order to functionalize diamond particles surface with alkyl groups. The following characterization techniques were used: SEM, TEM, DLS distribution, Raman scattering spectroscopy, XRD, FTIR and NMR spectroscopy.*

The raw microdiamond powder is used to dope silica aerogels in order to prepare a diamond-doped silica aerogel composite material for use in solar geoengineering and the results of the analysis of the final diamond-doped silica aerogel are presented in Chapter 5. The properties including optical properties of those composites will be shown and discussed with a goal to choose an optimal material for the application.

Furthermore, treatment of the microdiamonds could be useful for broader applications such as in order to enhance or tune the fluorescence of the fluorescent particles [22]. Octadecylamine-terminated nanodiamonds (ND-ODA) yielded blue fluorescence, which is related to the covalent bonding between nanodiamonds and ODA [138]. 1-undecyl-terminated nanodiamonds had narrower and blue shifted fluorescence compared to the unfunctionalized nanodiamonds [139]. It has been reported that Ge quantum dots (QDs) functionalized with 1-octadecene showed much higher quantum yield than unfunctionalized Ge QDs [22]. Also, Si QDs showed different lifetime of decay when the surface was terminated with alkyl and oxygen [22]. Hence, it is suggested the treatment of fluorescent diamonds, such as NV and NVN (nitrogen-vacancy-nitrogen) colour centres could further improve their optical properties. Moreover, silica aerogel has been reported to increase the lifetime of the decay of fluorescent nanodiamonds when used as a matrix for nanodiamonds [63].

Detonation nanodiamonds treated with 1-undecene with zirconia beads milling and soxhletation have been previously reported in Šiller's group [81], where nanodiamonds were de-agglomerated and functionalized by 1-undecene. In this chapter it is attempted to adapt the procedure to HPHT microdiamonds. HPHT diamond particles do not inherently agglomerate due to absence of graphitic carbon phase [83]. Nevertheless, functionalization of the microdiamond surface is examined.

#### 4.1 Scanning electron microscopy of microdiamonds

SEM (methodology described in Chapter 3.2.1) images of raw microdiamond powder are given in Figure 4.1, while 1-undecene-treated microdiamond powder (preparation method described in Chapter 3.1.2) is presented in Figure 4.2. Diamond particle size is up to  $\sim 1 \mu\text{m}$ . Both diamond powders contain irregular particles with sharp edges, which does not change with the treatment. These results also confirm that the raw diamond particles are within a size range of 0-2  $\mu\text{m}$ , as stated by the supplier Element6.

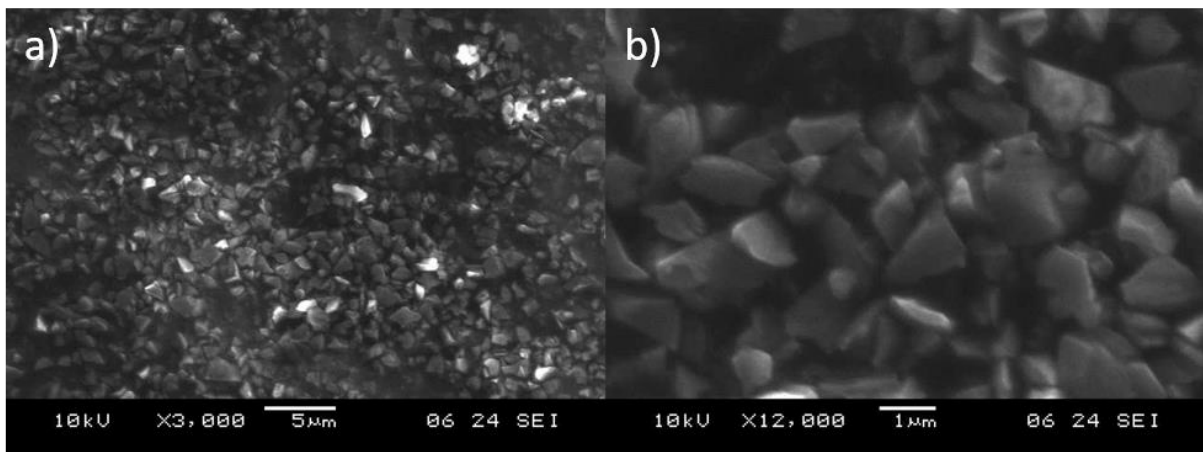
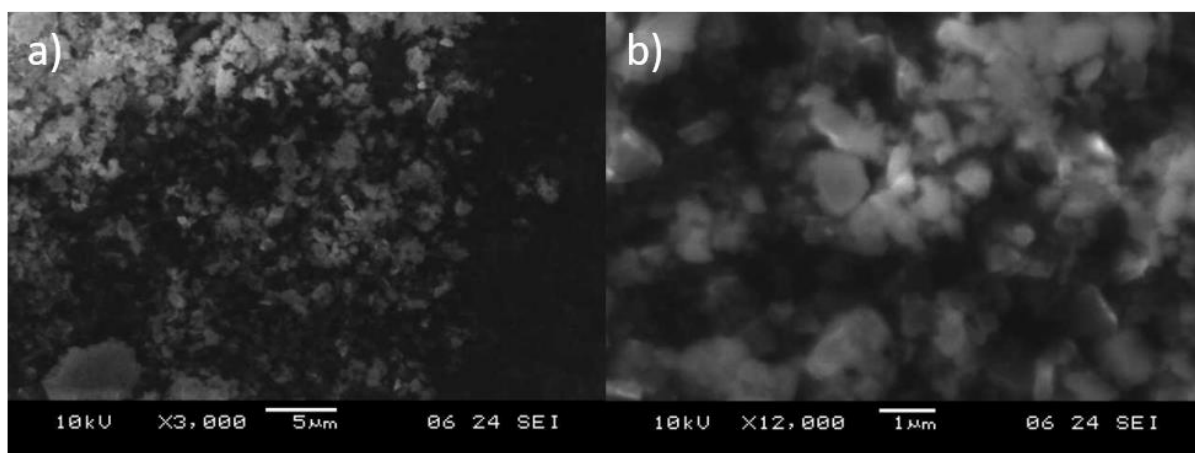


Figure 4.1: SEM image of raw microdiamond powder with scale bar: a) 5  $\mu\text{m}$ , and b) 1  $\mu\text{m}$ .



*Figure 4.2: SEM image of 1-undecene-treated microdiamond powder with scale bar: a) 5  $\mu\text{m}$ , and b) 1  $\mu\text{m}$ .*

#### 4.2 Transmission electron microscopy of microdiamonds

Similarly to SEM imaging, TEM (methodology described in Chapter 3.2.2) images shown in Figure 4.3 and Figure 4.4 are used to look closer at microdiamond particles before and after the treatment with 1-undecene (preparation method described in Chapter 3.1.2), respectively. Sharp edges of diamond along with irregular shape stay after the treatment, without any significant difference in diamond particle size before and after the treatment. The TEM images show the size of diamonds for both raw and treated microdiamond powder to be  $\sim 500$  nm, which is in agreement with SEM images. The particles have sharp edges in agreement with SEM, see for example Figure 4.1b.

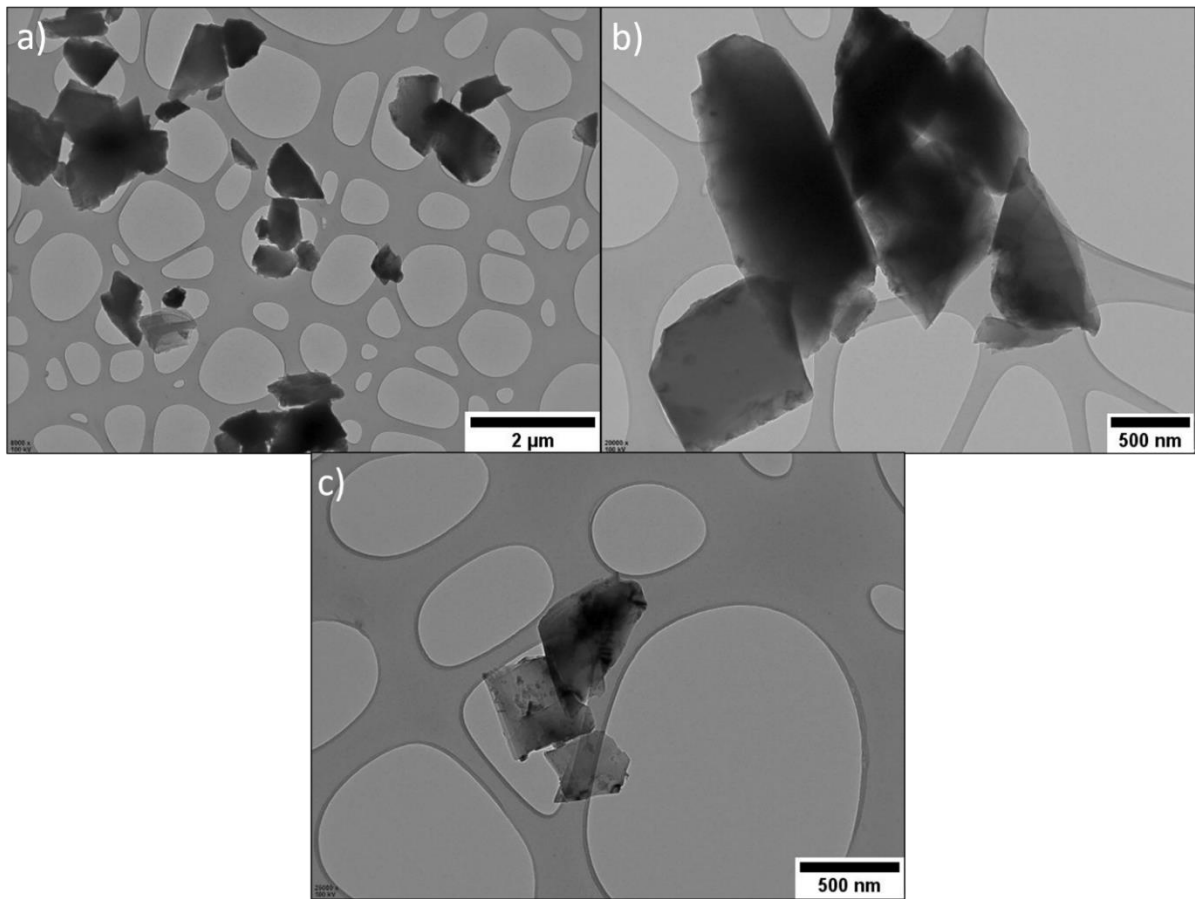


*Figure 4.3: TEM image of raw microdiamond particles with scale bar: a) 2 μm, b) 500 nm, and c) 500 nm.*

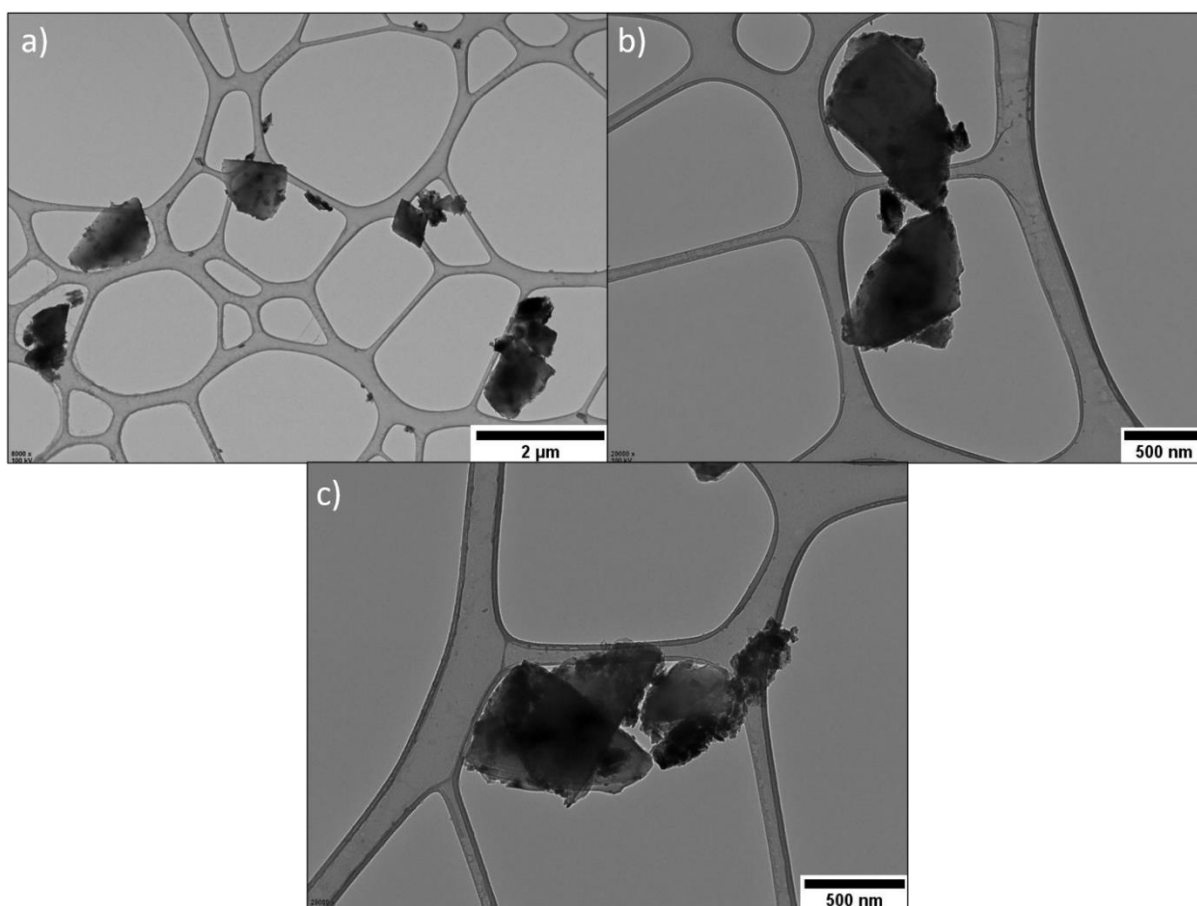


Figure 4.4: TEM image of 1-undecene-treated microdiamond particles with scale bar: a) 2  $\mu\text{m}$ , b) 500 nm, and c) 500 nm.

### 4.3 Dynamic light scattering of microdiamonds

Figure 4.5 shows the DLS particle size distribution (methodology described in Chapter 3.6) of both raw (in black) and treated (in red) microdiamond powder (preparation method described in Chapter 3.1.2). The number distribution peaks at 295 nm for the raw microdiamonds, while the maximum for the treated microdiamonds is at 255 nm. The Z-average decreases from  $552.1 \pm 7.3$  nm (raw diamond) to  $507.7 \pm 2.9$  nm (1-undecene diamond). This suggests that although the particles cover a broad size range from about 150-2000 nm, the great majority of the particles are below 1  $\mu\text{m}$ . This result also suggests that the bead shaking slightly decreased the particle size. It can be also noticed that the distribution of the particle size of the 1-undecene-treated microdiamond is narrower compared to the raw powder. It is assumed that the functionalization with 1-undecene chains terminates the surface of diamond and could stop polarization forces between some diamond particles.

Moreover, DLS distribution and Z-average are in agreement with SEM and TEM seen above (Chapter 4.1 and 4.2).

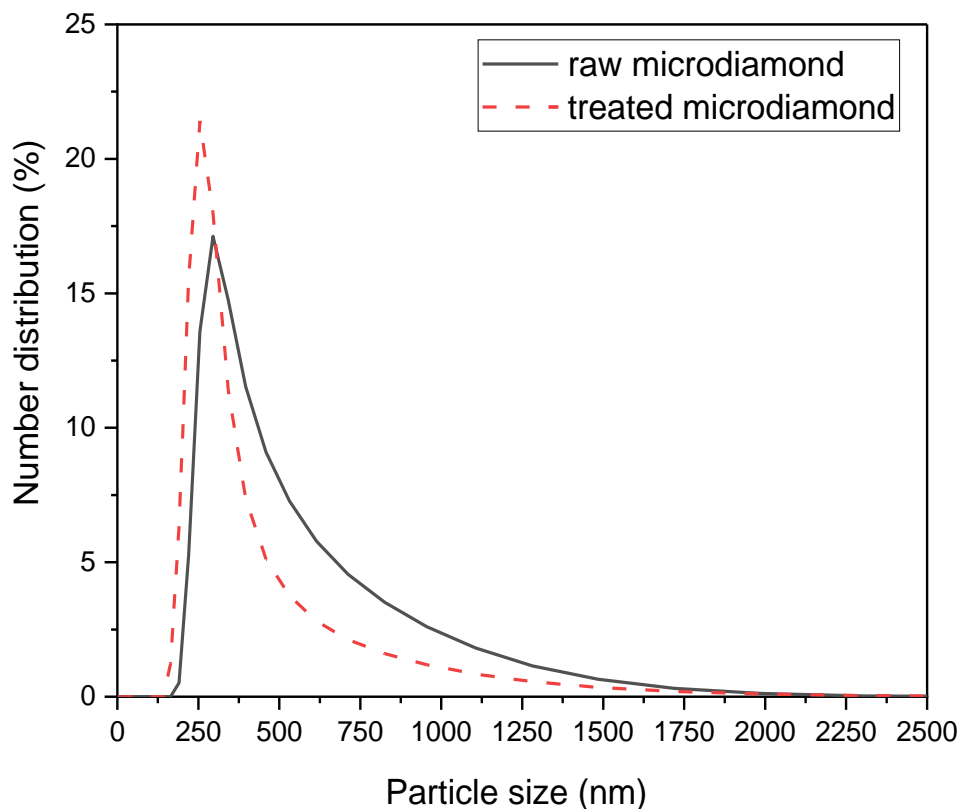


Figure 4.5: The DLS particles size distribution of raw diamond (black) and 1-undecene-treated diamond (red).

#### 4.4 Raman scattering spectroscopy of microdiamonds

Raman spectra for raw (in black) and treated (in red) microdiamond (preparation method described in Chapter 3.1.2) are represented in Figure 4.6 (methodology described in Chapter 3.4.3). The diamond feature related to the cubic phase appears at  $1332\text{ cm}^{-1}$  [140, 141]. Absence of the graphitic peaks at  $1350\text{ cm}^{-1}$  (D-band) and  $1590\text{ cm}^{-1}$  (G-band) [140] in both Raman spectra suggests that shaking with beads during the treatment does not give rise graphitic carbon on the surface of the diamond particles and shows that both diamond powders have a high level of purity. This is advantageous for use of diamond particles as solar scatterers, where UV/Vis radiation originating from the Sun is not absorbed by graphitic layers on diamond particles [142].

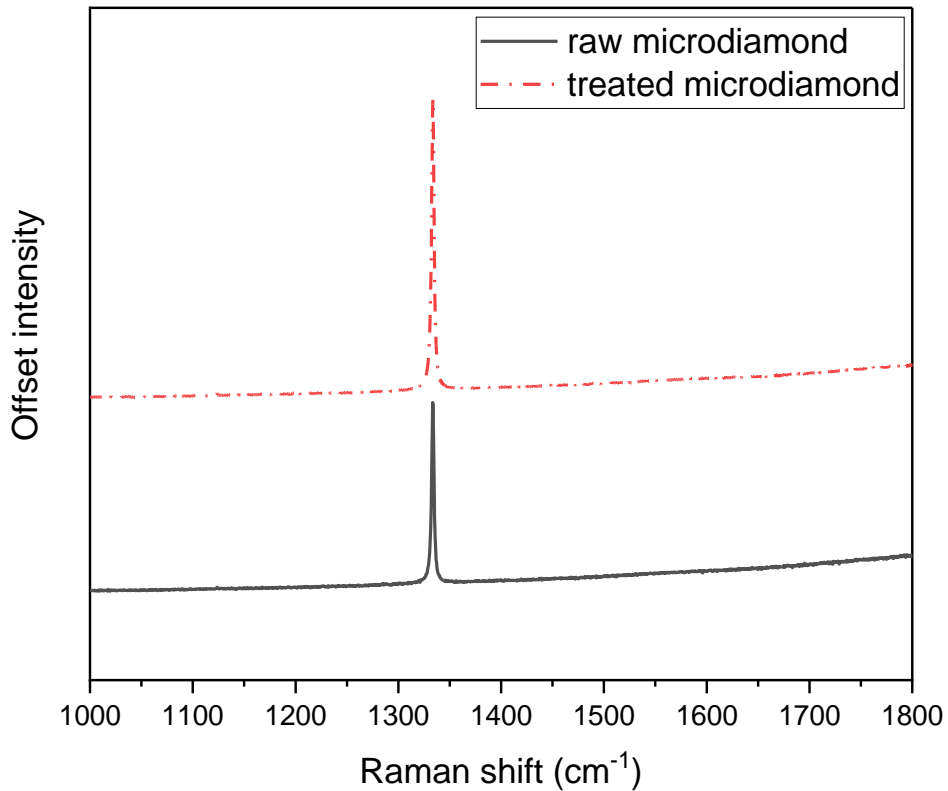


Figure 4.6: Raman spectrum of raw (black) and 1-undecene-treated microdiamond (red).

#### 4.5 X-ray diffraction of microdiamonds

Figure 4.7 presents the XRD (methodology described in Chapter 3.3) patterns of raw (in black) and treated (in red) (preparation method described in Chapter 3.1.2) microdiamonds, where the cubic diamond phase is identified with three crystallographic planes (111) at  $44^\circ$ , (220) at  $75.4^\circ$  and (311) at  $91.4^\circ$  [143]. The treated diamond powder XRD pattern has two additional peaks at  $\sim 28^\circ$ ,  $31^\circ$  and  $50^\circ$  that are related to the zirconium oxide, which is believed to originate from the bead during the shaking treatment. No graphitic peak (002) at  $2\theta = 27^\circ$  [144] confirms Raman measurements (Chapter 4.4) that shaking did not introduce significant graphitic carbon concentrations on the diamond particle surface (1-undecene-treated diamond).

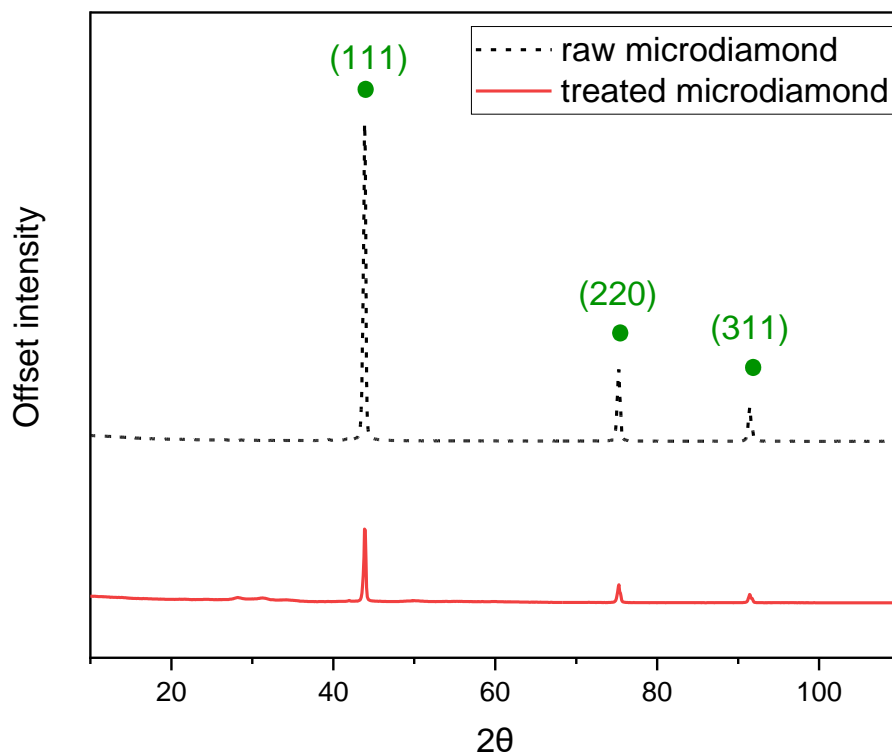


Figure 4.7: XRD patterns of raw (black) and 1-undecene-treated microdiamond (red).

#### 4.6 FTIR spectroscopy of microdiamonds

The FTIR (methodology described in Chapter 3.4.4) spectra of raw (in black) and the treated (in red) (preparation method described in Chapter 3.1.2) microdiamond powder is shown in Figure 4.8. The absorbance bands at 2958, 2923 and 2855  $\text{cm}^{-1}$  are related to the presence of  $-\text{CH}_x$  groups [145] in the spectrum of 1-undecene treated microdiamond, indicating the functionalization of the surface of the treated diamond. The bands present at  $\sim 3950$ - $3550 \text{ cm}^{-1}$  and  $\sim 1900$ - $1325 \text{ cm}^{-1}$  suggest water absorption as both powders take up moisture from the air. Also, the presence of characteristic bands for carbon dioxide ( $\sim 2300 \text{ cm}^{-1}$ ) is observed in the spectra.

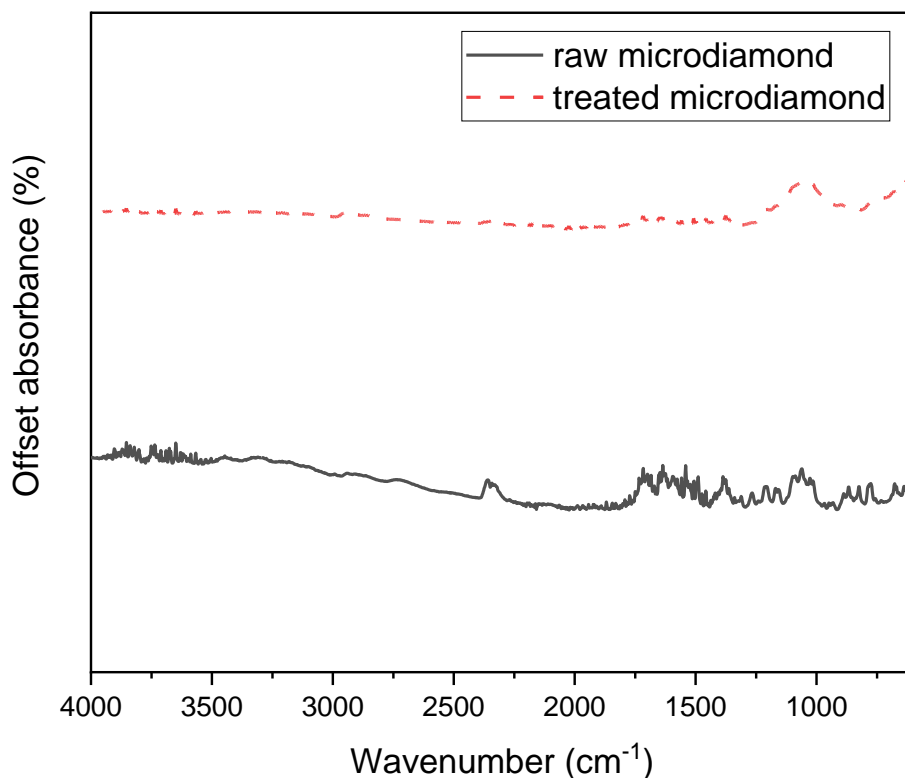


Figure 4.8: The FTIR of raw (black) and 1-undecene-treated microdiamond powder (red).

#### 4.7 Nuclear magnetic resonance spectroscopy of microdiamonds and 1-undecene solution

NMR experiment was described in Chapter 3.5 of this work, in order to examine the surface and the surface groups of microdiamond powders, as well as to look at the presence of  $sp^3$  and  $sp^2$  carbon in those samples. The raw and treated (preparation method described in Chapter 3.1.2) microdiamond powders and 1-undecene solution as a reference were recorded.

##### 4.7.1 Solid-state $^1H$ NMR data of microdiamonds

Figure 4.9 and Figure 4.10 show  $^1H$  NMR spectra of raw and treated microdiamond, respectively. Low signal to noise ratio in the spectrum of raw microdiamond indicates a low content of protons in the sample, while the peak at 1 ppm in case of treated microdiamond is related to the presence of alkyl groups [146].

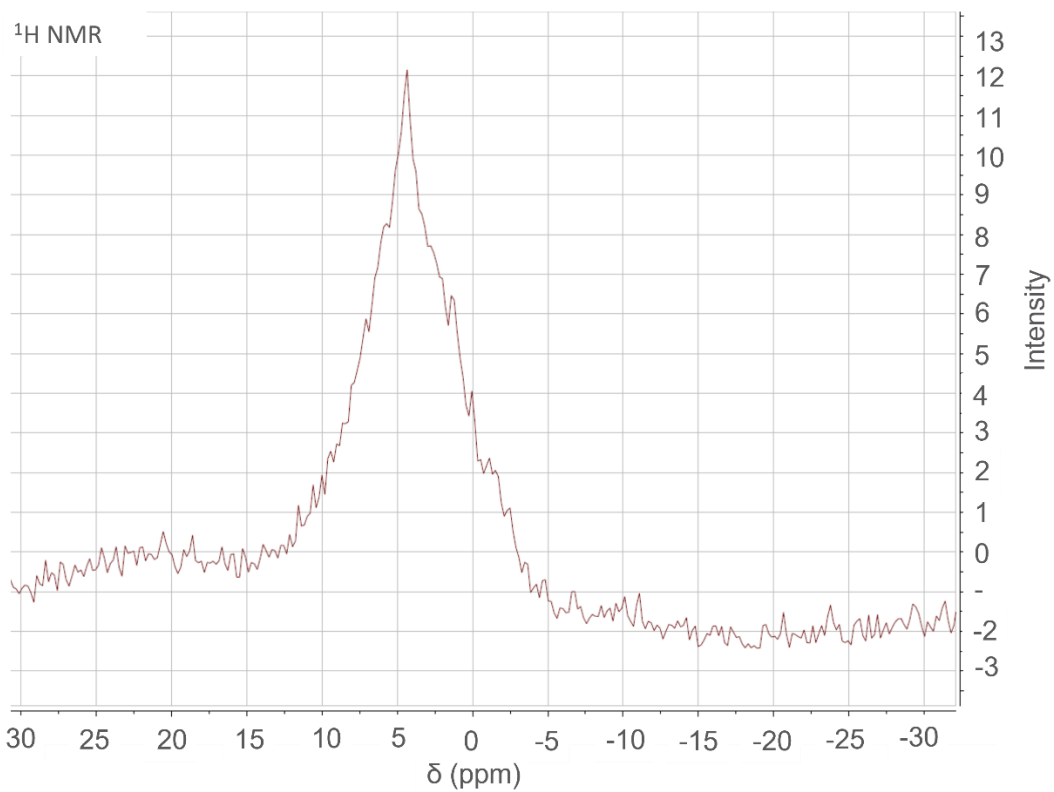


Figure 4.9: Solid-state  $^1\text{H}$  NMR spectrum of raw microdiamond.

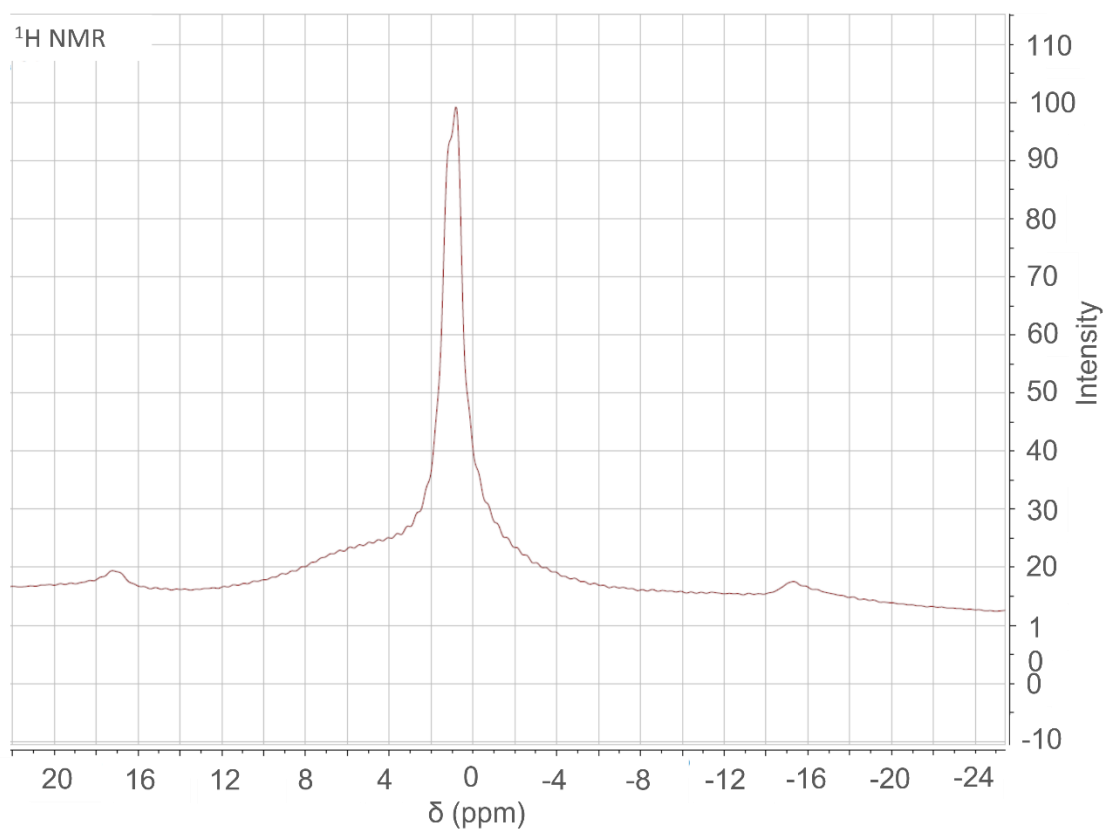


Figure 4.10: Solid-state  $^1\text{H}$  NMR spectrum of 1-undecene-treated microdiamond.

#### 4.7.2 Solid-state $^{13}\text{C}$ NMR data of microdiamonds

$^{13}\text{C}$  NMR spectra of raw and treated microdiamond were obtained using both cross-polarization (CP) and magic-angle spinning (MAS) techniques. In the case of raw microdiamonds, a low signal to noise ratio spectrum was observed for CP-MAS (see Figure 4.11), while a higher signal to noise ratio was noticed for MAS (see Figure 4.12). Both CP-MAS and MAS experiments for raw microdiamond showed a peak at 34 ppm consistent with  $\text{sp}^3$  hybridized carbon [146], only that a stronger signal was obtained in the MAS spectrum. It is proposed that a weak signal with CP-MAS is due to a very little proton on the surface of the raw microdiamond, also observed in the  $^1\text{H}$  NMR spectrum (see Figure 4.9).

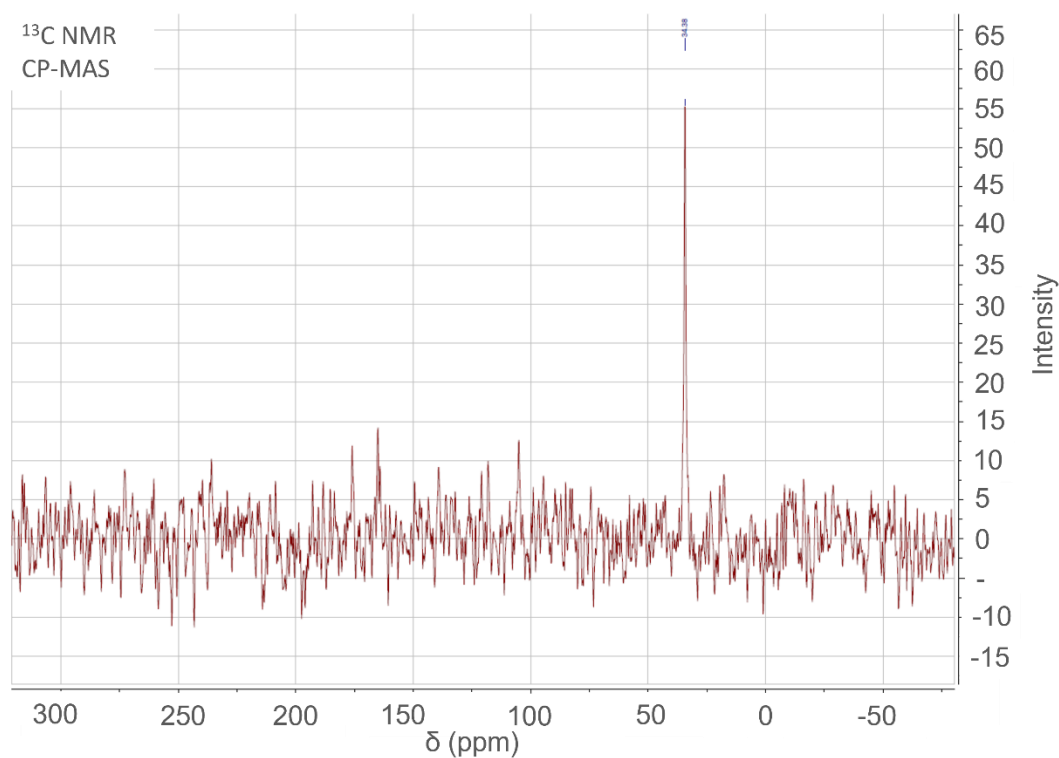


Figure 4.11: Solid-state  $^{13}\text{C}$  NMR CP-MAS spectrum of raw microdiamond.

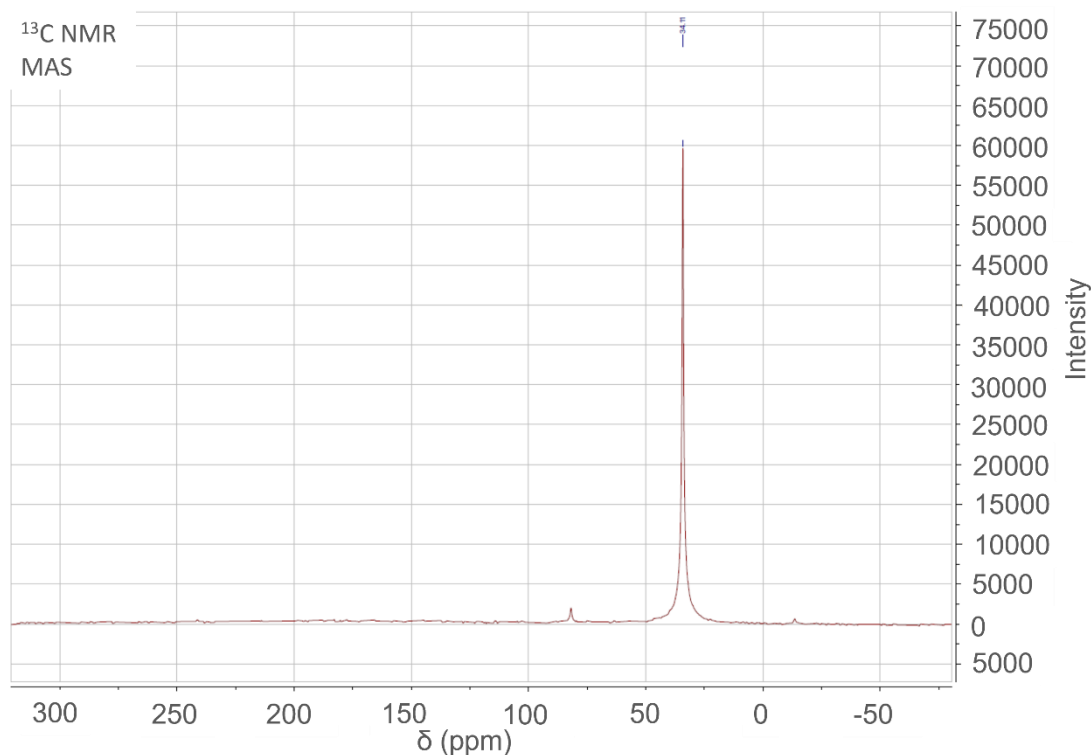


Figure 4.12: Solid-state  $^{13}\text{C}$  NMR MAS spectrum of raw microdiamond.

Similarly to  $^{13}\text{C}$  NMR spectra of raw diamond, treated microdiamond was measured using CP-MAS and MAS techniques (see Figure 4.13). In the CP-MAS of treated microdiamond (green spectrum) strong peaks at 21.3, 25.7 and 43.4 ppm indicate the presence of protons and are related to alkyl groups on the diamond surface [146]. Also, MAS spectrum of treated microdiamond (red) showed a strong signal at 34 ppm due to presence  $\text{sp}^3$  hybridized carbon [146]. In  $^{13}\text{C}$  NMR spectra of both raw and treated microdiamonds, no evidence of peaks at 120 ppm suggests the absence of  $\text{sp}^2$  hybridized graphitic carbon [146]. Hence, it is proposed that microdiamond treatment does not give rise to graphitic carbon.

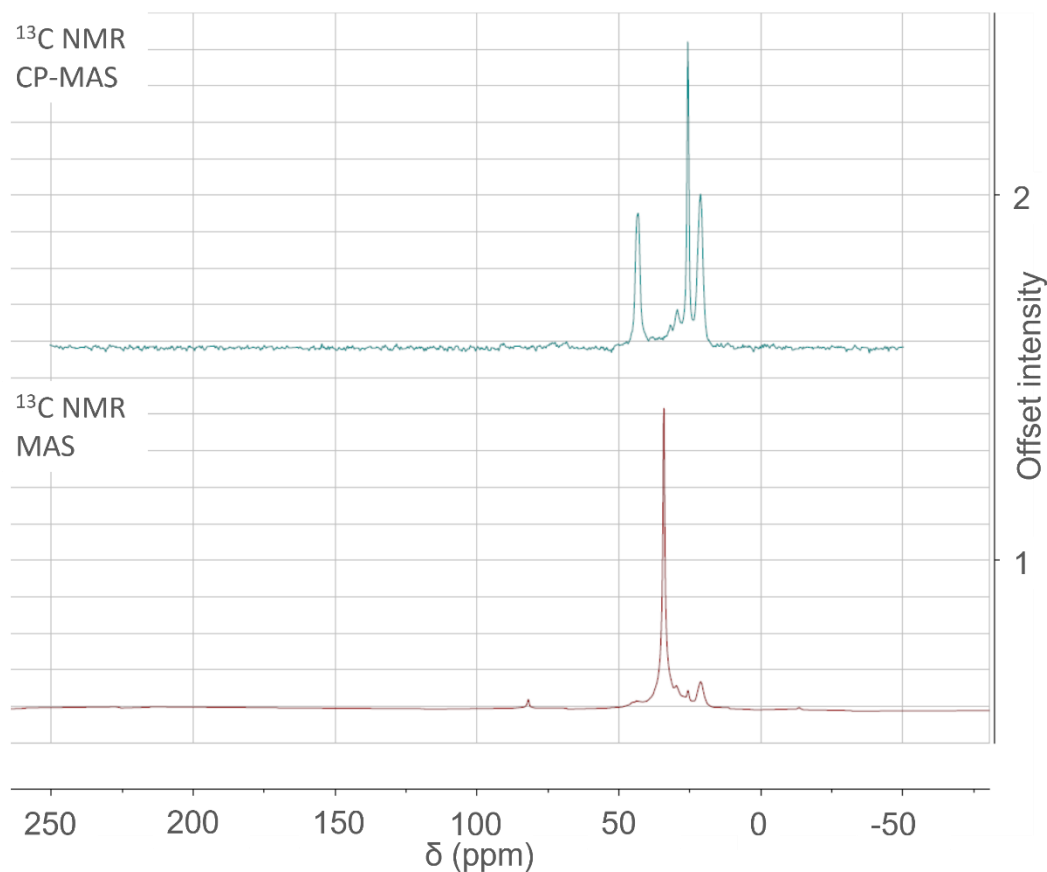


Figure 4.13: Solid-state  $^{13}\text{C}$  NMR CP-MAS (green) and MAS (red) spectra of 1-undecene-treated microdiamond.

#### 4.7.3 Solution-state $^{13}\text{C}$ NMR data of 1-undecene solution

$^{13}\text{C}$  NMR spectrum of 1-undecene ( $\text{C}_{11}\text{H}_{22}$ ) is presented in Figure 4.14. Peaks from 0 to 50 ppm are related to the presence of alkyl groups in the sample, while the two peaks at  $\sim 115$  and  $\sim 140$  ppm are due to alkene groups [146]. Triplet at  $\sim 77$  ppm corresponds to the solvent- $\text{CDCl}_3$ . Peaks at 115-140 ppm were not observed in the spectra of treated microdiamond (see Figure 4.13), indicating that the treatment of raw microdiamonds breaks down the double bonds. Also, it is suggested that since the solid-state NMR peaks are in general broader and may overlap, the solution-state NMR gave rise to more peaks in the 0-50 ppm range [115].

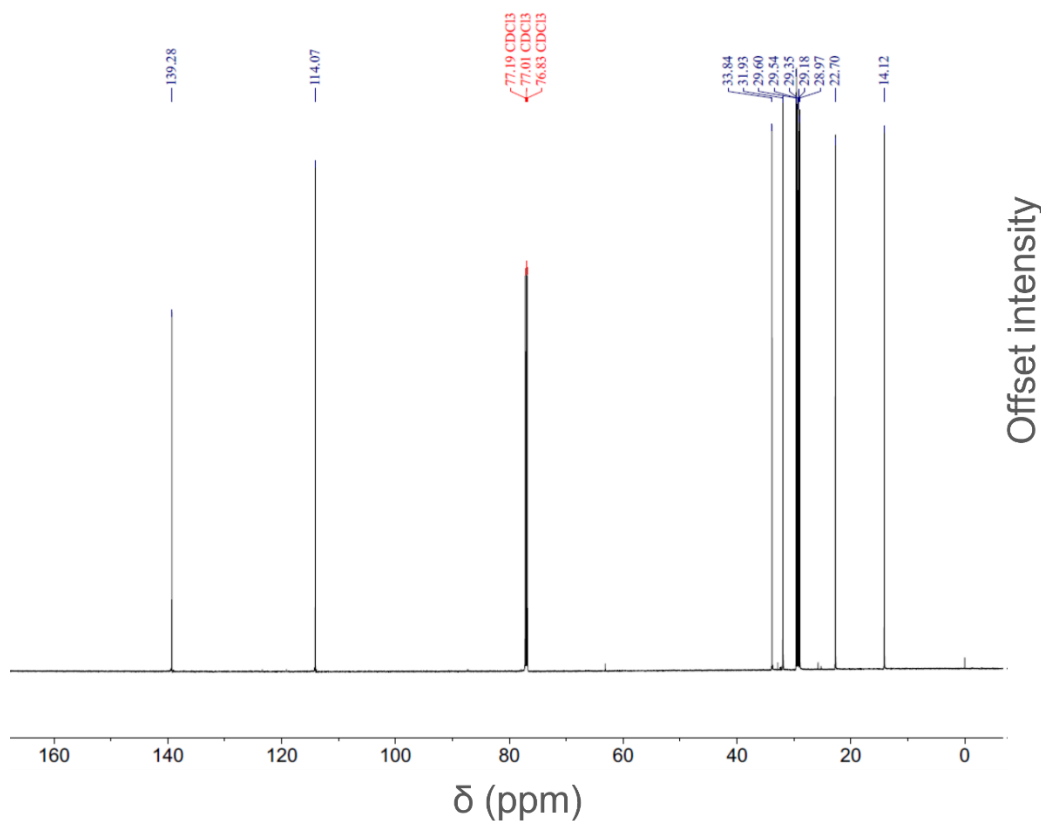


Figure 4.14: Solution-state  $^{13}\text{C}$  NMR spectrum of pure 1-undecene.

From NMR experiments it is concluded that the treatment of raw microdiamonds with 1-undecene and zirconia beads leads to disappearance of alkene related groups. It is suggested that after the double bond of 1-undecene is broken, alkyl groups ( $\text{CH}_x$ ) are attached to the surface of the treated microdiamonds and form chemical bonds. Furthermore, after the treatment of microdiamonds, graphitic carbon does not appear on the diamond surface.

#### 4.8 Conclusion

The shaking method used in this chapter has been modified from a method for de-agglomerating and functionalizing the surface of the detonation nanodiamonds. Since the diamonds in question in this chapter are micro-sized HPHT diamonds and hence no agglomerates, nor any big change in particle size was expected.

FTIR and NMR spectroscopies confirm the presence of hydrophobic alkyl surface groups in the treated microdiamond powder originating from the bead shaking in 1-undecene. SEM and TEM confirm that the diamond particle size and shape did not significantly change after the treatment of the raw diamond. Also, it is suggested that alkyl chains on the particle surface

could keep small particles separated from bigger particles. This could lead to narrower and slightly shifted DLS distribution to the smaller particle range, while confirming the average size of both diamond powders to be about 500 nm. The treated diamond powder contains small amount of impurities (zirconium oxide) introduced during the shaking (shown by XRD), but remain pure without a presence of  $sp^2$  graphitic carbon (confirmed by Raman scattering and NMR spectroscopy) or contamination similarly to the raw powder.

## Chapter 5 Diamond-doped silica aerogels

*This chapter shows the characterization of silica aerogel without and with diamond doping with raw microdiamonds characterized in Chapter 4. In this chapter, the study of silica aerogels is presented with the aim of showing the porosity and surface area, as well as the diamond doping and the effect of doping on silica aerogel properties. SEM, TEM, FTIR spectroscopy, XRD, BET surface area and BJH pore size distribution and reflectance measurement were used. The goal is to synthesize a diamond-doped silica aerogel that is highly porous and light to both accommodate diamond particles and stay in the atmosphere for a long time in order to reflect as much of the Sunlight as possible in the UV/Vis/NIR. At the same time, high transmittance in the IR intrinsic for diamond would allow non-absorbance of the IR coming back to space from the Earth.*

In this chapter the results of the reflectance measurements of diamond in silica aerogels are presented, encouraged by the aforementioned theoretical models suggesting potential use of these materials in solar geoengineering (as discussed in Chapter 2.1) [6]. Preparation of the pure and microdiamond-doped aerogels and characterization methods were described in Chapter 3. The current work focuses on bulk measurements of the prepared aerogel in a form of a granulated layer. By grinding and size selection of the diamond-doped silica aerogel solid atmospheric aerosols could be obtained, which could be used for solar scattering [5]. The obtained results from this work can be used as a starting point to evaluate the proposed novel composite material and offer insight for the possible further future improvements. The reflectance data of raw microdiamond powder, pure silica aerogel and 900 ppm raw microdiamond-doped silica aerogel presented in this chapter have been published [147]. Additionally, the publication included the characterization of raw microdiamond powder (presented in Chapter 4) and characterization of pure silica aerogel and 900 ppm raw microdiamond-doped silica aerogel (also presented in this chapter).

### 5.1 Scanning electron microscopy of silica aerogels

The SEM (methodology described in Chapter 3.2.1) image of the pure silica aerogel (preparation method described in Chapter 3.1.3) prepared as a fine powder is presented in Figure 5.1, where particles cover the wide range of sizes from some being smaller than 1  $\mu\text{m}$

to those bigger than 20  $\mu\text{m}$ . Films made of fine powder aerogels particles were also optically measured in Section 5.7.

Diamond particles in silica aerogels could not be observed by SEM, due to the fact that they were covered by silica aerogels. As such, the pure and diamond-doped silica aerogels both resembled one another. The SEM images of pure silica aerogel is presented in Figure 5.2, where a typical porous aerogel structure is observed.

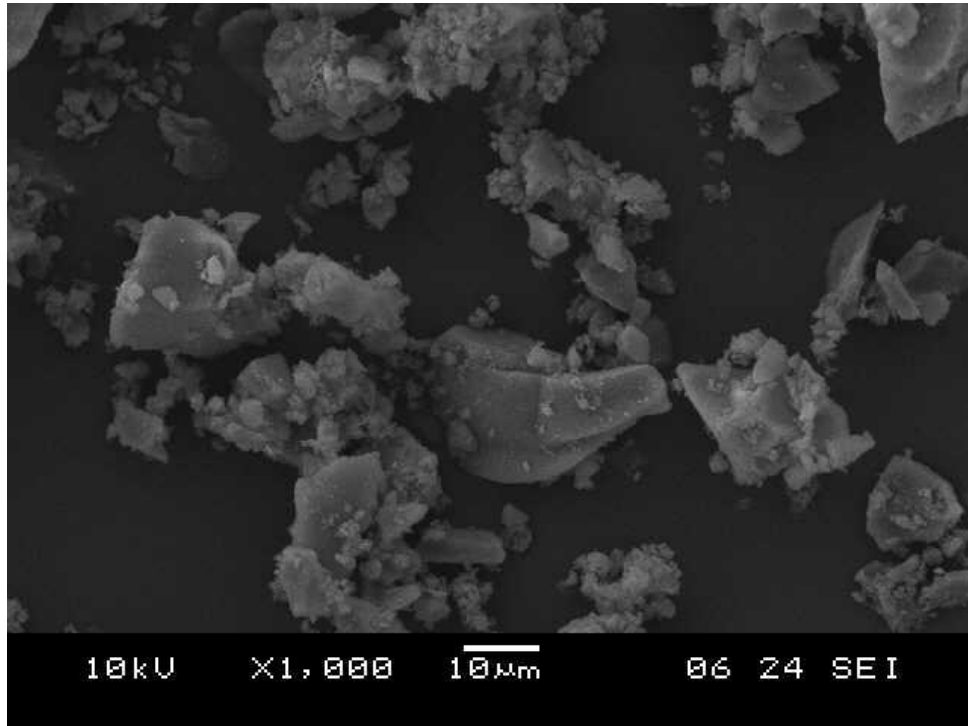


Figure 5.1: SEM image of silica aerogel (fine powder) with scale bar 10  $\mu\text{m}$ .

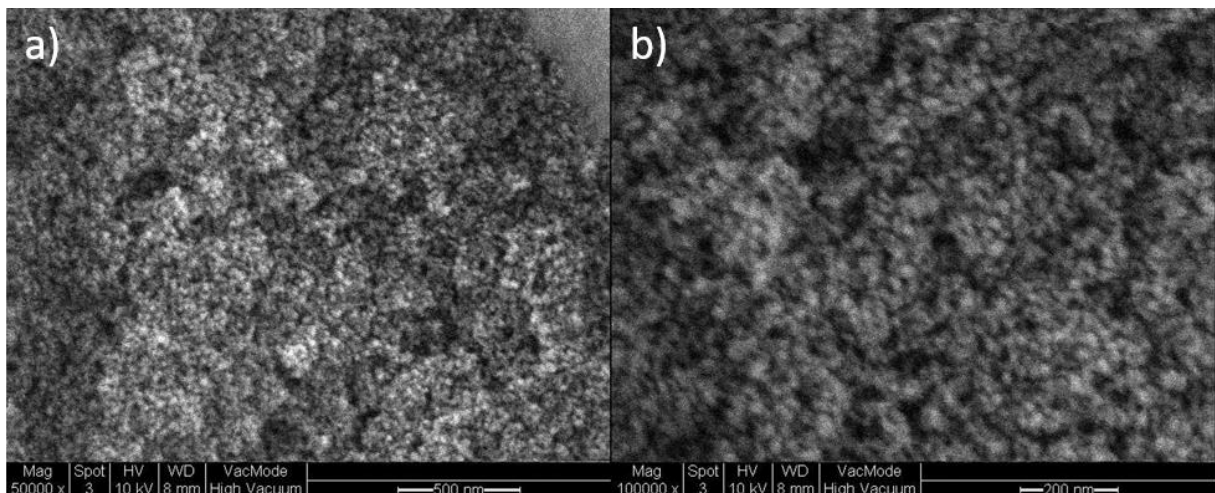


Figure 5.2: SEM image of pure silica aerogel with scale bar: a) 500 nm, and b) 200 nm.

## 5.2 Transmission electron microscopy of microdiamond-doped silica aerogel

The TEM (methodology described in Chapter 3.2.2) image of the pure silica aerogel (preparation method described in Chapter 3.1.3) (see Figure 5.3) is in agreement with SEM image of the pure silica in terms of high porosity and grape-like structure. The darker areas are due to the overlapping layers of silica particles which form the networking microstructure of the aerogel. The 900 ppm diamond-doping of silica aerogel (preparation method described in Chapter 3.1.3) was captured by TEM in Figure 5.4, which shows that the silica aerogel contains a diamond particle with a length of  $\sim 500$  nm. Diamond particles maintain their sharp edges, size, and irregular shape which is consistent with the diamond images prior to doping, as seen in Chapter 4 (Section 4.1 and 4.2). The influence of the incorporation of diamond on the nanoporosity of silica will be discussed in Sections 5.5 and 5.6 (Brunauer-Emmett-Teller (BET) and Barrett-Joyner-Halenda (BJH) analysis, and density calculations, respectively).

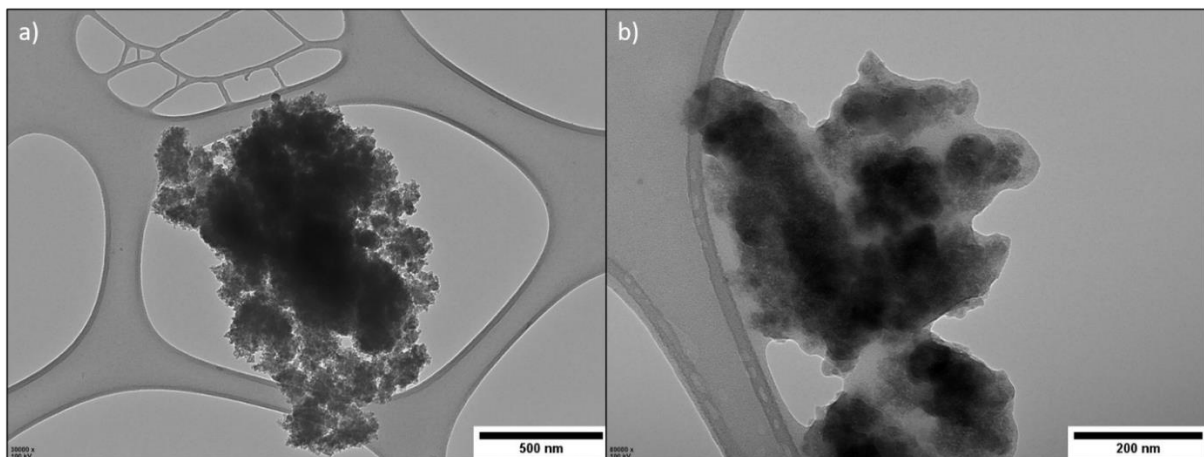
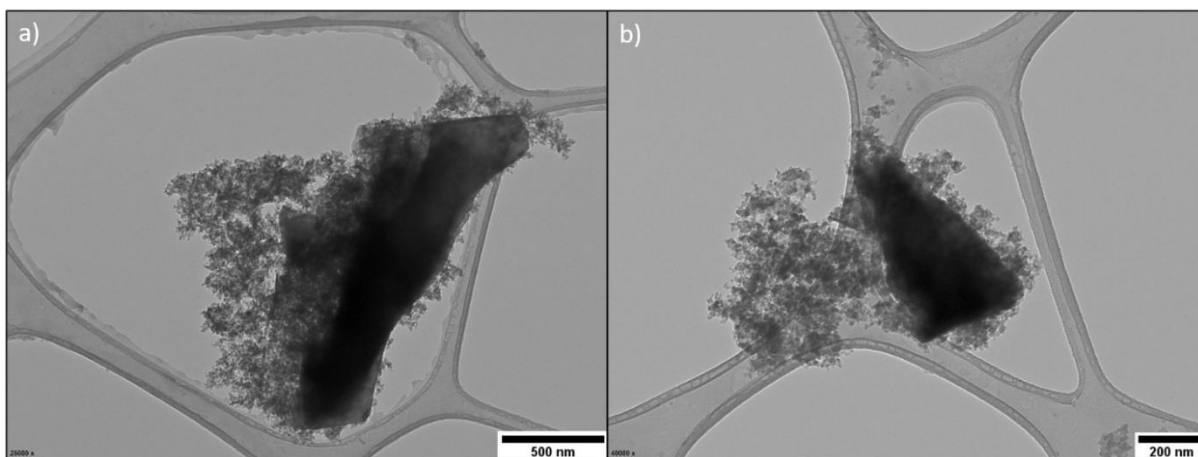


Figure 5.3: TEM image of pure silica aerogel with scale bar: a) 500 nm, and b) 200 nm.



*Figure 5.4: TEM image of 900 ppm raw-microdiamond/silica aerogel with scale bar: a) 500 nm, and b) 200 nm.*

### 5.3 FTIR spectroscopy of silica aerogels

There is no difference in FTIR (methodology described in Chapter 3.4.4) spectra between the pure and the 500, 700 and 900 ppm raw microdiamond-doped spectra (preparation method described in Chapter 3.1.3) (see Figure 5.5). All aerogels show distinctive silica aerogel bands [148]. Furthermore, the spectra are similar to the typical FTIR spectrum of hydrophilic silica aerogel [149]. A representative FTIR transmittance spectrum is shown in Figure 5.6. Water ( $\sim 1500\text{ cm}^{-1}$  and  $\sim 3500\text{ cm}^{-1}$ ) and carbon dioxide ( $\sim 2300\text{ cm}^{-1}$ ) originating from the ambient air, also appear in the spectrum. Bands at  $800\text{ cm}^{-1}$  and  $1075\text{ cm}^{-1}$  are related to the Si-O-Si symmetric and asymmetric vibrations [148], respectively. The presence of Si-OH groups on the surface is confirmed by the  $550\text{ cm}^{-1}$  and  $960\text{ cm}^{-1}$  bands [148].

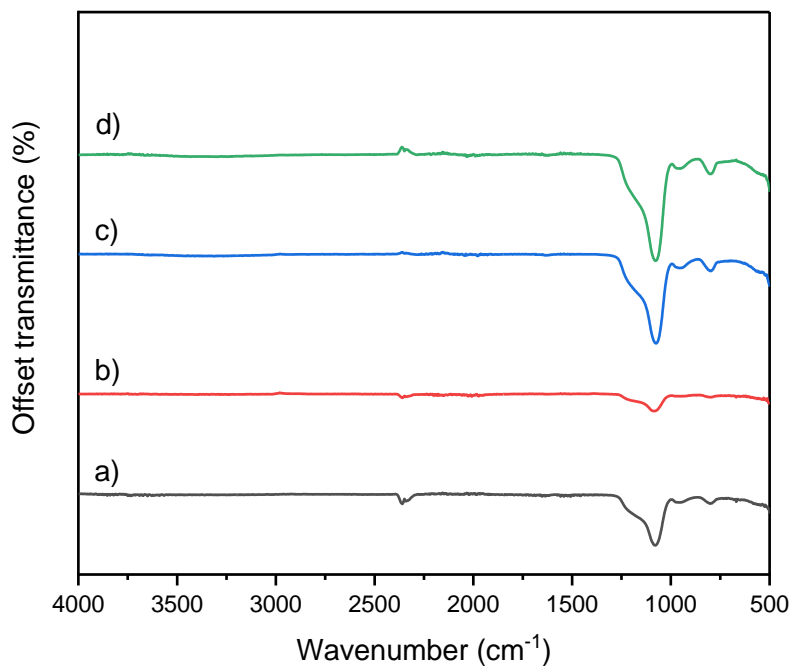


Figure 5.5: FTIR spectra of: a) pure, b) 500 ppm microdiamonds/silica, c) 700 ppm microdiamonds/silica, and d) 900 ppm microdiamonds/silica aerogel.

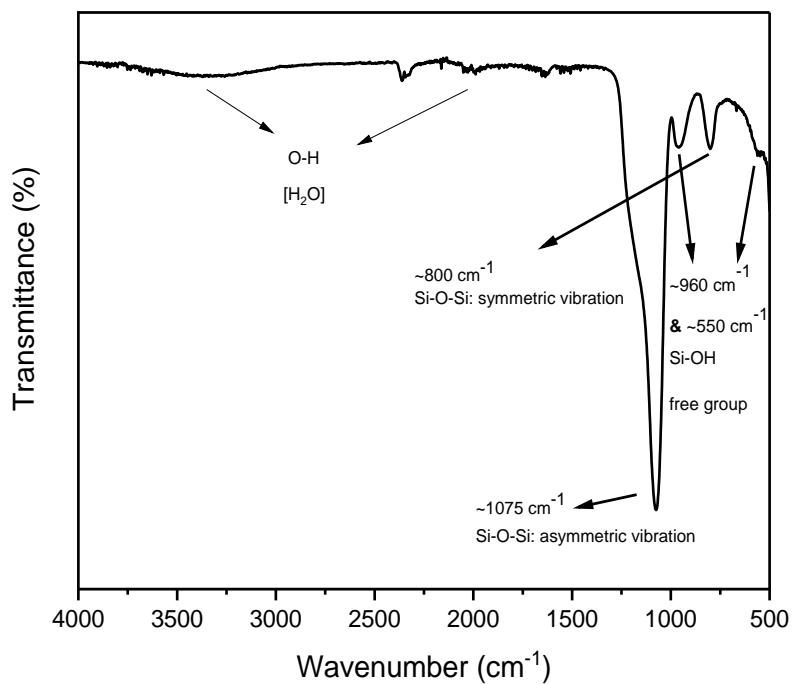


Figure 5.6: A representative FTIR spectrum of a silica aerogel.

#### 5.4 X-ray diffraction of silica aerogels

The XRD (methodology described in Chapter 3.3) patterns of pure and 500, 700 and 900 ppm raw microdiamond-doped silica aerogels (preparation method described in Chapter 3.1.3) are presented in Figure 5.7. All silica aerogels have a broad, amorphous peak at  $\sim 22^\circ$  [150], while all doped aerogels show three additional crystalline diamond peaks. A representative XRD pattern of a diamond-doped silica aerogel is represented in Figure 5.8. The diamond peaks correspond to the cubic diamond structure with the following diamond planes [143]:  $44^\circ$  (111),  $75.4^\circ$  (220) and  $91.4^\circ$  (311). Furthermore, the XRD patterns are in agreement with the observed diamond-doping of silica aerogel determined by TEM.

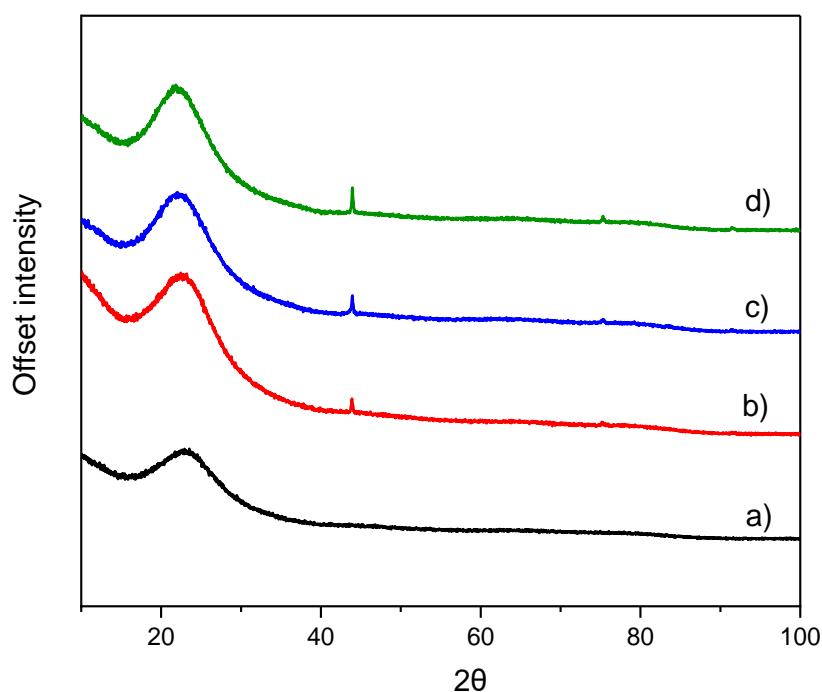


Figure 5.7: XRD patterns of: a) pure, b) 500 ppm microdiamonds/silica, c) 700 ppm microdiamonds/silica, and d) 900 ppm microdiamonds/silica aerogel.

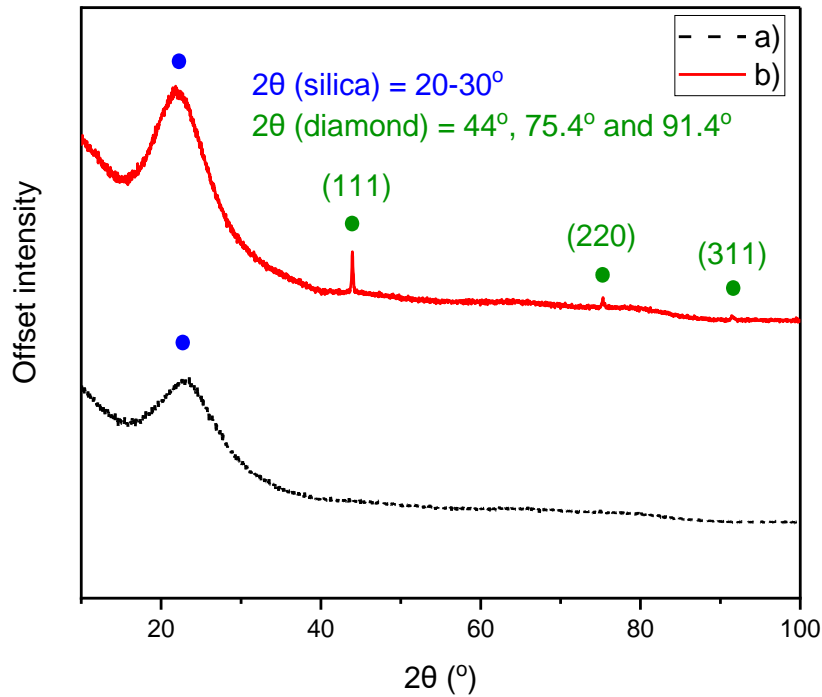


Figure 5.8: A representative XRD pattern of: a) pure, and b) diamond-doped silica aerogel.

Additionally, the results of the XRD quantitative analysis (methodology described in Chapter 3.3) of 500, 700 and 900 ppm raw microdiamonds in silica aerogels (preparation method described in Chapter 3.1.3) are listed in Table 5.1. For the silica aerogels doped with raw microdiamonds, the higher the doping concentrations in precursors, the higher amount of the diamond in the final silica aerogels. Hence the final diamond incorporation in silica aerogels is as follows: 500 R (2.8 wt%) < 700 R (3.0 wt%) < 900 R (3.3 wt%) (see Figure 5.9). Accordingly, all samples have more than 96 wt% of silica aerogel. XRD percentages for the synthesized aerogels are consistent with the adapted procedure [104], where Ni nanoparticles are doped to TEOS aerogels with concentrations of 500, 700 and 900 ppm in the precursor solution and 2.9-4.9 wt% in the final aerogel.

Table 5.1: Comparison between concentration of diamond in the precursor sol (ppm) and amount of diamond in the final silica aerogel (%).

Sample	Concentration of diamond in the precursor sol (ppm)	Diamond, wt% (XRD) [± 0.1 wt%]	Silica, wt% (XRD) [± 0.1 wt%]
Pure 0.5	0	0	100
Pure 0.6	0	0	100
500 R	500	2.8	97.2
700 R	700	3	97
900 R	900	3.3	96.7

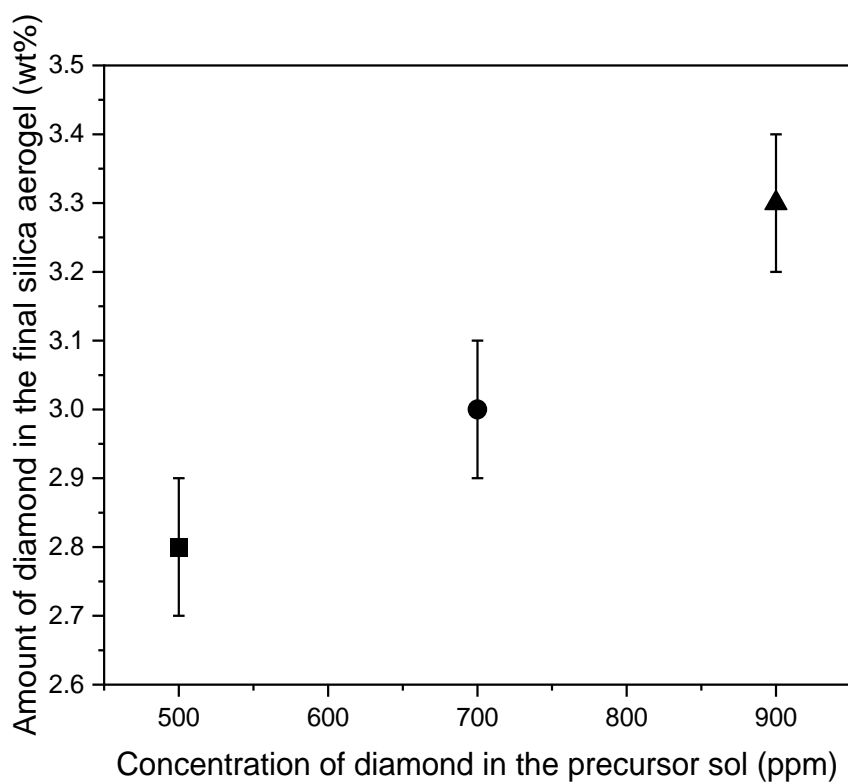


Figure 5.9: Plot of concentration of diamond in the precursor sol (ppm) Vs amount of diamond in the final silica aerogel (wt%) for 500, 700 and 900 ppm microdiamonds/silica aerogels.

## 5.5 Brunauer-Emmett-Teller and Barrett-Joyner-Halenda analysis of silica aerogels

The adsorption-desorption isotherm (methodology described in Chapter 3.7) of pure and 500, 700 and 900 ppm raw microdiamond-doped silica aerogels (preparation method described in Chapter 3.1.3) are presented in Figure 5.10-5.14. As described in Chapter 3.1.3, two pure silica aerogels were prepared, with 0.5 and 0.6 ml catalyst, in order to be used as reference samples for 500 ppm (prepared with 0.5 ml catalyst), and 700 and 900 ppm (prepared with 0.6 ml catalyst) raw microdiamond-doped silica aerogels. The presence and shape of the hysteresis loop (H1 type) is observed, that suggests the presence of open cylindrical mesopores in all samples of aerogels [134].

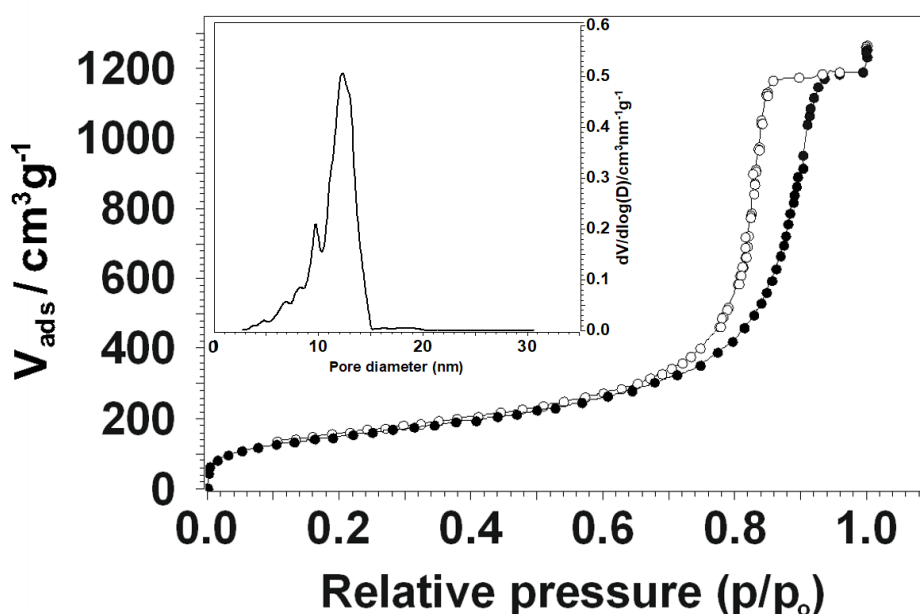


Figure 5.10: The nitrogen adsorption-desorption isotherm and the pore size distribution of the 0.5 ml catalyst pure silica aerogel (as insert).

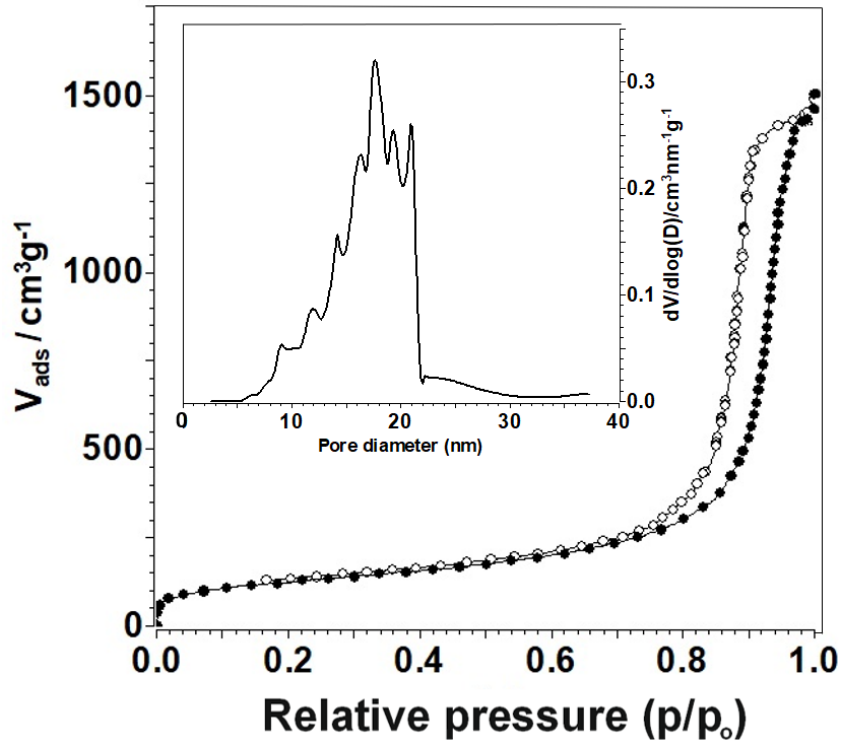


Figure 5.11: The nitrogen adsorption-desorption isotherm and the pore size distribution of the 500 ppm raw microdiamond-doped silica aerogel (as insert).

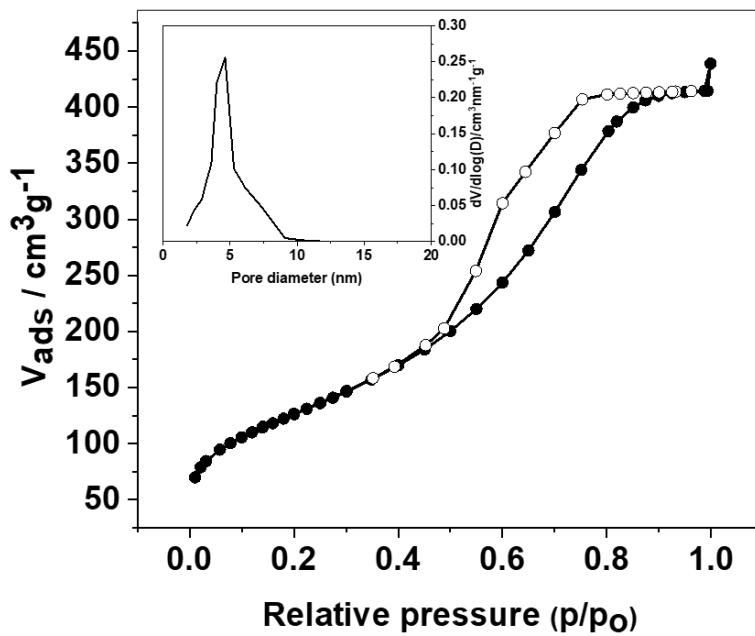


Figure 5.12: The nitrogen adsorption-desorption isotherm and the pore size distribution of the 0.6 ml catalyst pure silica aerogel (as insert).

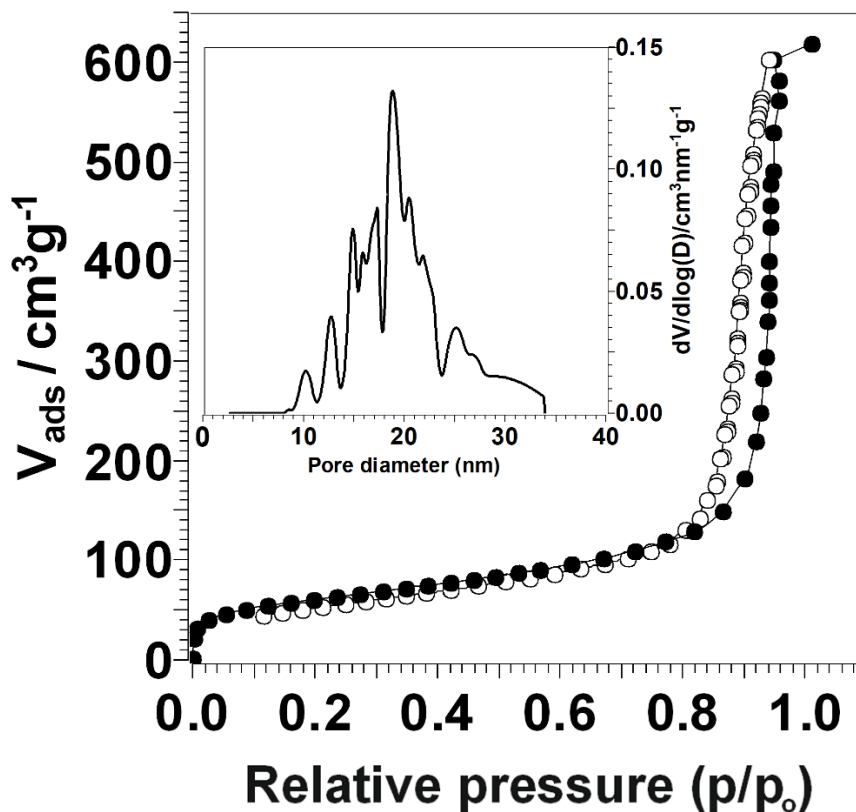


Figure 5.13: The nitrogen adsorption-desorption isotherm and the pore size distribution of the 700 ppm raw microdiamond-doped silica aerogel (as insert).

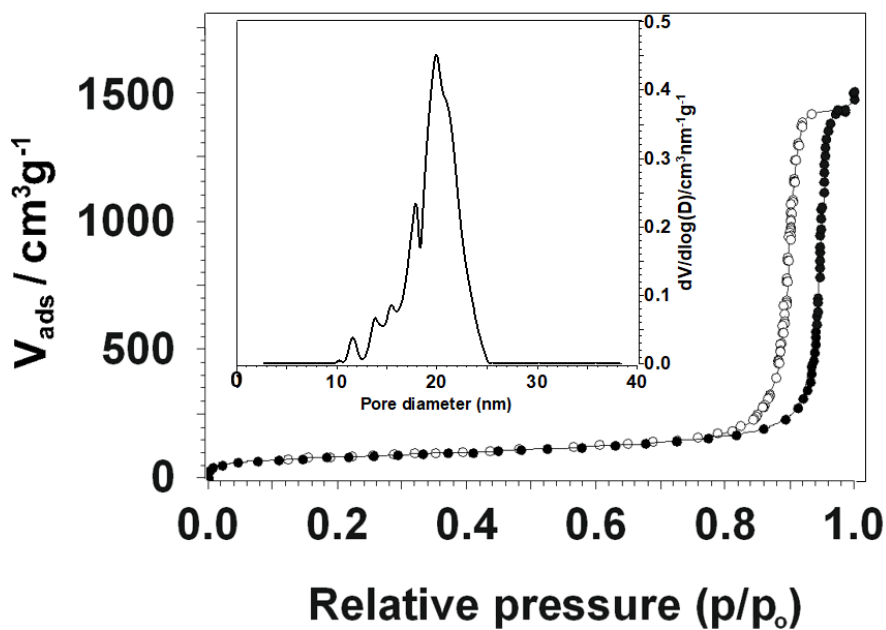


Figure 5.14: The nitrogen adsorption-desorption isotherm and the pore size distribution of the 900 ppm raw microdiamond-doped silica aerogel (as insert).

Table 5.2 lists BET surface area, pore specific volume, average pore size and porosity of pure (0.5 ml catalyst), pure (0.6 ml catalyst), 500, 700, 900 ppm raw microdiamond-doped silica aerogels. In general, it can be seen that the higher BET surface area of the final microdiamond-doped aerogels is obtained when less diamond is added to the precursor solution (see Figure 5.15a). Similarly, higher BET surface area is observed in case of raw microdiamond-doped silica aerogels when less diamond is incorporated in the final aerogel (Figure 5.15b), where BET surface area was in the range 215-445 m<sup>2</sup>/g. The 700 ppm raw microdiamond-doped aerogel sample does not follow this decrease trend in BET surface area. Therefore, it can be assumed that diamond particles do not decrease the surface area just due to doping but due to increasing the stress in the silica possibly breaking and inducing stress to silica network during drying. Average pore diameter is the lowest for pure aerogels with 0.5 and 0.6 ml catalyst, with them having the highest BET surface area of all aerogels (544 m<sup>2</sup>/g and 459 m<sup>2</sup>/g, respectively). It can be concluded that doping of silica aerogels with raw microdiamonds decreases the surface area with a slight increase of average pore diameter (Figure 5.16a and b). However, the surface area and porosity remain high which would reflect greatly on the predicted fall speed of pure and 900 ppm raw microdiamond-doped aerogels discussed in the following section (Section 5.6). No relationship between the pure and doped aerogels is observed for pore specific volume.

*Table 5.2: Relationship between with XRD percentage of diamond in silica aerogels and BET surface area, pore specific volume, average pore diameter and porosity.*

Sample	Diamond, wt% (XRD) [± 0.1 wt%]	BET SA, m <sup>2</sup> /g [± 5 m <sup>2</sup> /g]	Pore specific volume, cm <sup>3</sup> /g [± 0.02 cm <sup>3</sup> /g]	Average pore diameter, nm [± 0.1 nm]
Pure 0.5	0	544	1.85	12.0
Pure 0.6	0	459	0.64	4.7
500 R	2.8	445	2.24	17.7
700 R	3	215	0.87	19.6
900 R	3.3	284	2.25	20.2

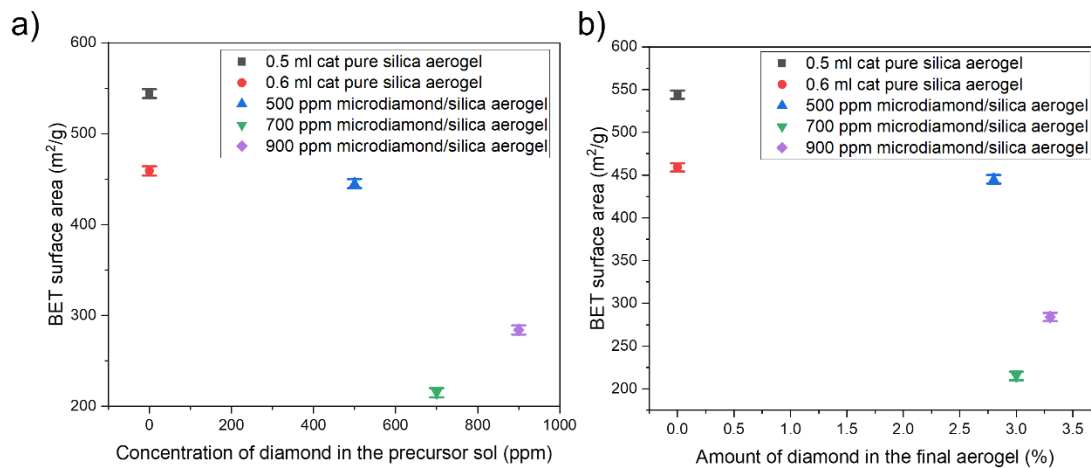


Figure 5.15: a) BET surface area Vs concentration of diamond in the precursor sol, and b) BET surface area Vs amount of diamond in the final aerogel, for pure (0.5 ml catalyst), pure (0.6 ml catalyst), 500, 700 and 900 ppm microdiamond-doped silica aerogels.

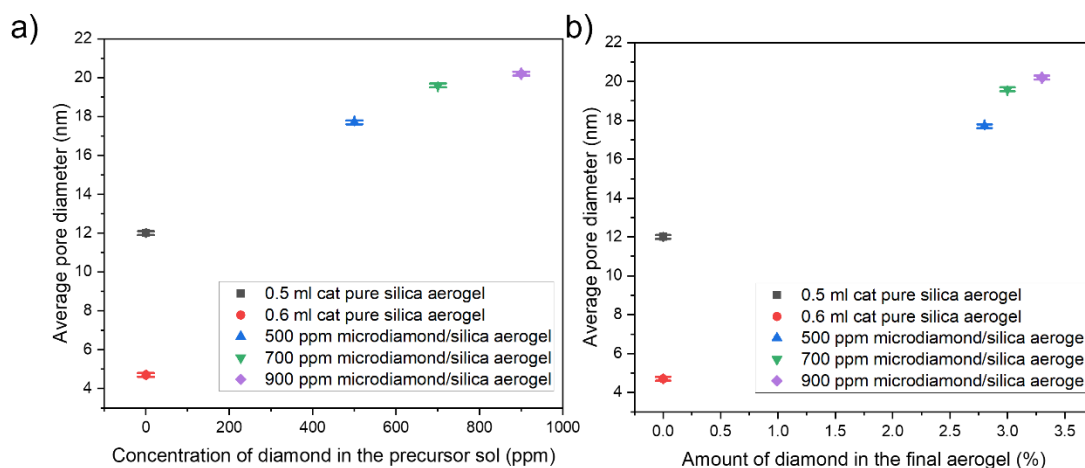


Figure 5.16: a) Average pore diameter Vs concentration of diamond in the precursor sol, and b) Average pore diameter Vs amount of diamond in the final aerogel, for pure (0.5 ml catalyst), pure (0.6 ml catalyst), 500, 700 and 900 ppm microdiamond-doped silica aerogels.

## 5.6 Density and fall speed of silica aerogels

The skeletal densities of pure and 500, 700 and 900 ppm raw microdiamond-doped silica aerogels (preparation method described in Chapter 3.1.3) are included in Table 5.3, where the pure and raw microdiamond-doped silica aerogels show similar skeletal density of  $\sim 2.65$ - $2.68 \text{ g/cm}^3$ . The mass per volume (bulk density) was determined and along with the skeletal density, porosity of all samples was calculated (methodology described in Chapter 3.7). It can

be observed that the density slightly increases and porosity decreases after doping with microdiamonds, as 500, 700 and 900 ppm raw microdiamond-doped silica aerogels show a higher density ( $\sim 0.353\text{-}0.381\text{ g/cm}^3$ ) and a lower porosity ( $\sim 85.8\text{-}86.8\%$ ) compared to the 0.5 ml catalyst pure silica aerogel (bulk density of  $0.281\text{ g/cm}^3$  and porosity of  $89.4\%$ ). The amount of catalyst (0.6 ml) used for the doped aerogels with 700 and 900 ppm raw microdiamonds is higher than that for the 500 ppm raw microdiamonds in silica due to the necessity of speeding up the gelation process in order to mitigate diamond particle accumulation and sedimentation. Compared to the pure silica aerogel with 0.5 ml catalyst, the pure silica aerogel with 0.6 ml catalyst has slightly increased bulk density ( $0.282\text{ g/cm}^3$ ) and decreased porosity ( $89.3\%$ ). The bulk density and porosity measurements suggest that the doping with all three concentrations seem to have greater influence on the increase of the bulk density and the decrease of the porosity than the influence of the amount of catalyst.

*Table 5.3: Relationship between with XRD percentage of diamond in silica aerogels and skeletal, bulk density and porosity.*

Sample	Diamond % (XRD) [ $\pm 0.1\text{ wt}\%$ ]	Silica % (XRD) [ $\pm 0.1\text{ wt}\%$ ]	Skeletal density, $\text{g/cm}^3$	Bulk density, $\text{g/cm}^3$ [ $\pm 0.001\text{ g/cm}^3$ ]	Porosity, %
Pure 0.5	0	100	2.65	0.281	89.4
Pure 0.6	0	100	2.65	0.282	89.3
500 R	2.8	97.2	2.67	0.353	86.8
700 R	3	97	2.68	0.381	85.8
900 R	3.3	96.7	2.68	0.368	86.3

Table 5.4 shows the average fall speed and time before particle sedimentation (methodology described in Chapter 3.8) for raw microdiamond, pure silica and 900 ppm raw microdiamond-doped silica aerogel particles, for the values of pressure,  $p=25\text{ hPa}$ , and temperature,  $T=220\text{ K}$ , which are the conditions of pressure and temperature at the altitude of 20 km in the stratosphere where solar aerosols are suggested [3] to be injected. Even though these values change during the particle fall, the aim is to give an idea of a fall speed and time (in days) the diamond-doped silica aerogel particles would stay in the atmosphere. Furthermore,

theoretical models should be employed in order to take changes in pressure and temperature into account and predict more precisely the fall speed and time. Since the highest wt% of microdiamonds in aerogel was in case of 900 ppm microdiamonds/silica sample, the fall speed (Section 5.6) and reflectance (Section 5.7) were obtained for that sample.

*Table 5.4: Average fall speed and time accordingly for raw microdiamond, pure silica and raw microdiamond-doped silica aerogel according to equation 2.5.*

Particle	Particle size, $\mu\text{m}^*$	Average density, $\text{g}/\text{cm}^3$	Average fall speed, $\text{cm}/\text{s}$	Average time in the atmosphere, days (years)
Microdiamond	0.5	3.51	0.0219	1057 (2.9)
Pure silica aerogel	1	0.281	0.0070	3306 (9)
Raw microdiamond-doped silica aerogel	1	0.368	0.0092	2516 (6.9)

*\*particle size is taken according to the average diamond particle size seen with DLS, as well as aerogel particle size seen on TEM and within the size range of minimum inhalation for humans.*

The average value of fall speed for both pure and doped aerogels are significantly lower (0.0070 and 0.0092 cm/s, respectively) than that of diamond particle alone (0.0219 cm/s), leading to years (9 and 6.9 years for pure and diamond-doped aerogel, respectively) of staying in the atmosphere before sedimentation. The average density for aerogel particles are taken for comparison since no size selection of the aerogel particles had been performed. However, it is suggested that the average fall speed could be used for offering an indication of how light the prepared materials are.

### 5.7 Reflectance of microdiamonds, pure and microdiamond-doped silica aerogel

Figure 5.17 shows the total diffuse reflectance (methodology described in Chapter 3.4.2) plot for a) the glass slide, b) raw microdiamond powder, c) pure silica aerogel, and d) 900 ppm raw

microdiamond-doped silica aerogel (preparation method described in Chapter 3.1.3). The glass slide, without a sample, was also scanned to account for the sample holder reflectance. Raw powder, pure silica aerogel, and diamond-doped silica aerogel samples all exhibited a reflectance between 30-50 %, out of which the glass slide contribution to the reflectance is only a couple of percent. It can be seen that pure diamonds decrease reflectance in the UV/Vis (290-600 nm), while improving the reflectance in the NIR (> 2000 nm), when compared to pure silica aerogel. This is a bit surprising, but can be explained because the diamond powder appears brown in colour, so increased absorption in the Vis region is expected, and therefore the subsequent reduction of the reflectance. Diamonds (without impurities and defects) generally will not absorb in the wavelength range of 225 nm to 1 mm and its structural symmetry leads to non-IR absorption [69]. However, this absorption edge can be shifted to a wavelength of 290 nm, when nitrogen impurities are present [151]. These nitrogen defects might have been introduced into the diamond powder during a high pressure high temperature (HPHT) synthesis. The nanoporous structure of silica aerogels gives rise to Rayleigh scattering, which is more intense for shorter wavelength scattering when the sunlight is passing through [35]. Hence, the high reflectance of silica aerogel in the region of ~ 290-400 nm was measured. From there, the silica aerogel reflectance decreases from ~ 400-800 nm because the transmission in this range increases towards longer wavelengths [152]. Also, it suggested that Mie scattering of the incoming radiation contributes to the reflectance in case of diamond particles and the white fine powder silica aerogel, which is not strongly wavelength dependent. The bands associated with the regions ~ 1400 nm and ~ 1900 nm are related to water and CO<sub>2</sub> absorption and appear only in silica aerogel reflectance patterns [36, 37]. The gratings change at 720 nm, while detectors switch at ~ 870 nm and 1650 nm and these show as features in the spectra [153]. The combination of O-H and Si-O in the structure gives rise to the ~ 2300 nm and 2500 nm bands [36, 38, 39]. These two absorptions are typical for silica aerogel. It can be seen that with the addition of diamond these two bands have a lower intensity. Taking into account that only ~ 3.3 wt% of diamond is added to the silica aerogel, the impact of diamond on the final reflectance of the doped-silica aerogel in the ~ 2300-2500 nm reflectance range is significant. Therefore, diamond justifies the theoretical predictions [6] about improving non-absorption in the NIR region. However, silica aerogel alone showed the highest reflectance in the UVA/UVB (290-400 nm) range. This suggests that silica aerogel would reflect this harmful radiation back into space and lessen the amount of

UVA/UVB radiation that reaches the Earth's surface. The combination of silica aerogel doped with diamond improves the up-scattering NIR light, in comparison to silica aerogel samples alone.

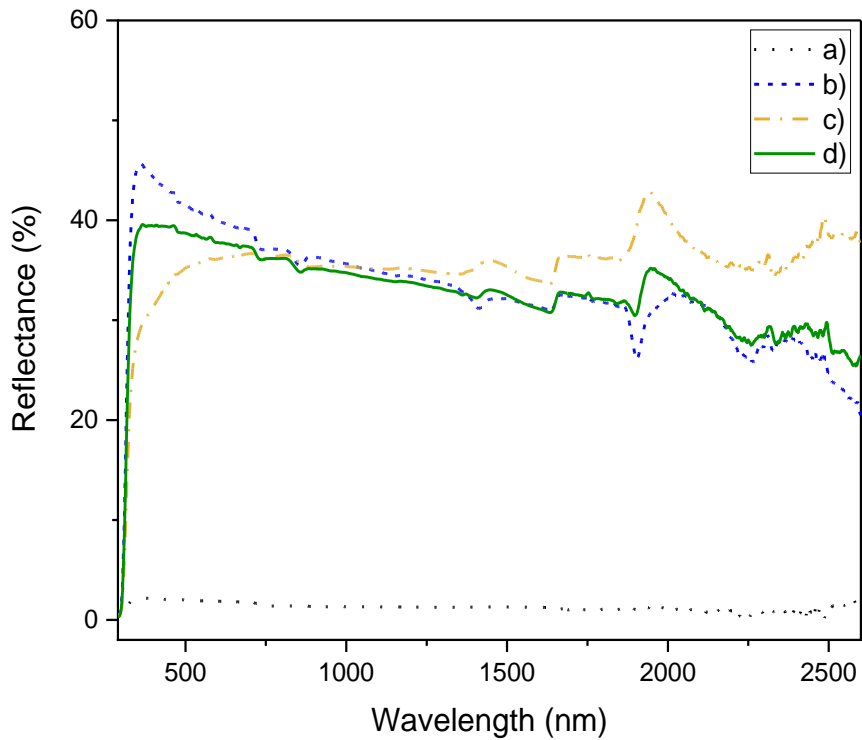


Figure 5.17: Reflectance spectra of: a) glass slide only, b) pure aerogel, c) raw microdiamond, and d) 900 ppm raw microdiamond-doped silica aerogel.

## 5.8 Conclusion

In this work, a diamond-doped silica aerogel for solar geoengineering has been successfully synthesized for the first time to the best of our knowledge. After doping with diamonds (particle size  $\sim 500$  nm), silica aerogel remained porous, with a low density, and a high surface area. For the intended application of the doped aerogel as a solar aerosol material, a  $1 \mu\text{m}$  composite size, observed by TEM, fulfils the prerequisite safety condition concerning particle inhalation. Reflectance of the prepared composite was measured to investigate the effect of the diamond doping on the optical properties of the silica aerogel. It could be noted that the microdiamond-doped aerogels had lower surface and higher density compared to the pure silica aerogels.

Due to its nanostructured composition, silica aerogel alone contributes to the highest scattering which is evident in the UVA/UVB/Vis wavelength range, whereas the diamond particles and diamond-doped silica aerogels allow improved scattering in the NIR radiation range. As for the UV/Vis region, composite shows lower reflectance compared to pure silica aerogel. Possible reason is that the HPHT diamonds often contain non-fluorescent isolated nitrogen atoms in the diamond lattice that absorbs below about 550 nm [154]. So it is suggested that one possibility in the future would be to use diamond particles without isolated nitrogen impurities, which could improve further the up-scattering in the UV/Vis. Ultimately, the reflectance data support the use of silica aerogel alone as a good scatterer in the UV/Vis, while the optimization of the diamond-doping is promising to further enhance the scattering in the UV/Vis and the transmission in the IR.

Importantly, the proposed composite design offers an opportunity to conduct a comparative optical study with smaller sized diamonds (nanoparticles, < 100 nm), where silica aerogel would serve as a matrix in order to maintain the aerosol particle size in the safer range (0.1-1  $\mu\text{m}$ ). Additionally, narrower size selection of the diamond dopant, as well as the doped aerogel, would allow measurement that can account for the specific particle size-reflectance relationship. In addition, due to the much lower density of aerogels compared to the density of diamonds, silica aerogels and silica aerogel diamond composite materials can provide substantially longer lifetime of aerosols in the stratosphere before they sediment and fall. It is believed that this work can give incentive to further research into the aerosol geoengineering field, in particular stratospheric chemistry and safety of the proposed diamond-doped silica aerosols based on the surface group interaction with resident stratospheric particles.

## Chapter 6 Detonation nanodiamonds in silica aerogel

*The results of characterisation of nanodiamonds are presented in this chapter. HRTEM was used to assess their size, while SAED and EELS were used to confirm the nanodiamond structure and presence of  $sp^2$  carbon on the surface. UV/Vis absorption spectroscopy was used to show optical behaviour in the range that is of interest for solar scattering. Nanodiamond colloids with different concentrations (4 wt% and 1 wt%) were characterized by pH-Zeta potential and DLS in order to examine their stability over time. Nanodiamonds were used to dope a silica aerogel. The characterization of nanodiamond-doped silica aerogel was done by HRTEM and XRD in order to observe nanodiamond distribution and content in the aerogel. The BET surface area and BJH pore size distribution were obtained to compare surface area and pore size of the pure and nanodiamond-doped silica aerogel. The obtained results in this chapter were compared to the data discussed in Chapter 5- raw microdiamonds in silica aerogels. Due to presence of graphitic surface on the nanodiamonds, these particles are not suitable for geoengineering as they absorb UV/Vis radiation. Nevertheless, some properties are desirable for progression towards improving diamond-doped silica aerogel for the solar aerosols application, such as higher content of nanodiamonds in the final doped aerogel in comparison to that of microdiamonds, and higher surface area of nanodiamond-doped aerogel than before the doping.*

As discussed in Chapter 2, nanodiamonds (from NanoCarbon Institute) with graphitic shell on the surface exhibit positive Zeta potential at acidic pH ( $\sim 4.7$ - $5.2$ ). Furthermore, the most stable nanodiamond concentration in a colloid was determined to be 4 wt%, whereas the nanodiamonds agglomerated and formed bigger particles in case of further dilution. In this chapter, it is aimed to observe the stability of nanodiamond colloids of different dilutions over time (6 days). Zeta-pH and DLS measurements will be used to evaluate the stability of colloids. Also, nanodiamonds will be added to silica aerogel in order to study the doping and silica aerogel properties such as surface area, density and porosity after addition of nanodiamonds, similarly to microdiamond doping of silica aerogels in Chapter 5. The goal is to compare how diamond particles size influence the properties of silica aerogel. Although detonation nanodiamond with graphitic carbon shell are not suitable for solar scattering, the smaller size can be used in order to investigate the proposed concept of this thesis, which is a diamond-silica aerogel composite for geoengineering.

## 6.1 Characterization of pure detonation nanodiamonds

Nanodiamonds dispersed in DI water (preparation method described in Chapter 3.1.4) were imaged in order to examine the particle size and presence of graphitic carbon on the diamond surface.

### *6.1.1 High resolution transmission electron microscopy of nanodiamonds*

Figure 6.1 shows the HRTEM image of nanodiamonds (methodology described in Chapter 3.2.2). It can be observed that nanodiamonds are between  $\sim 2$ -5 nm in size.

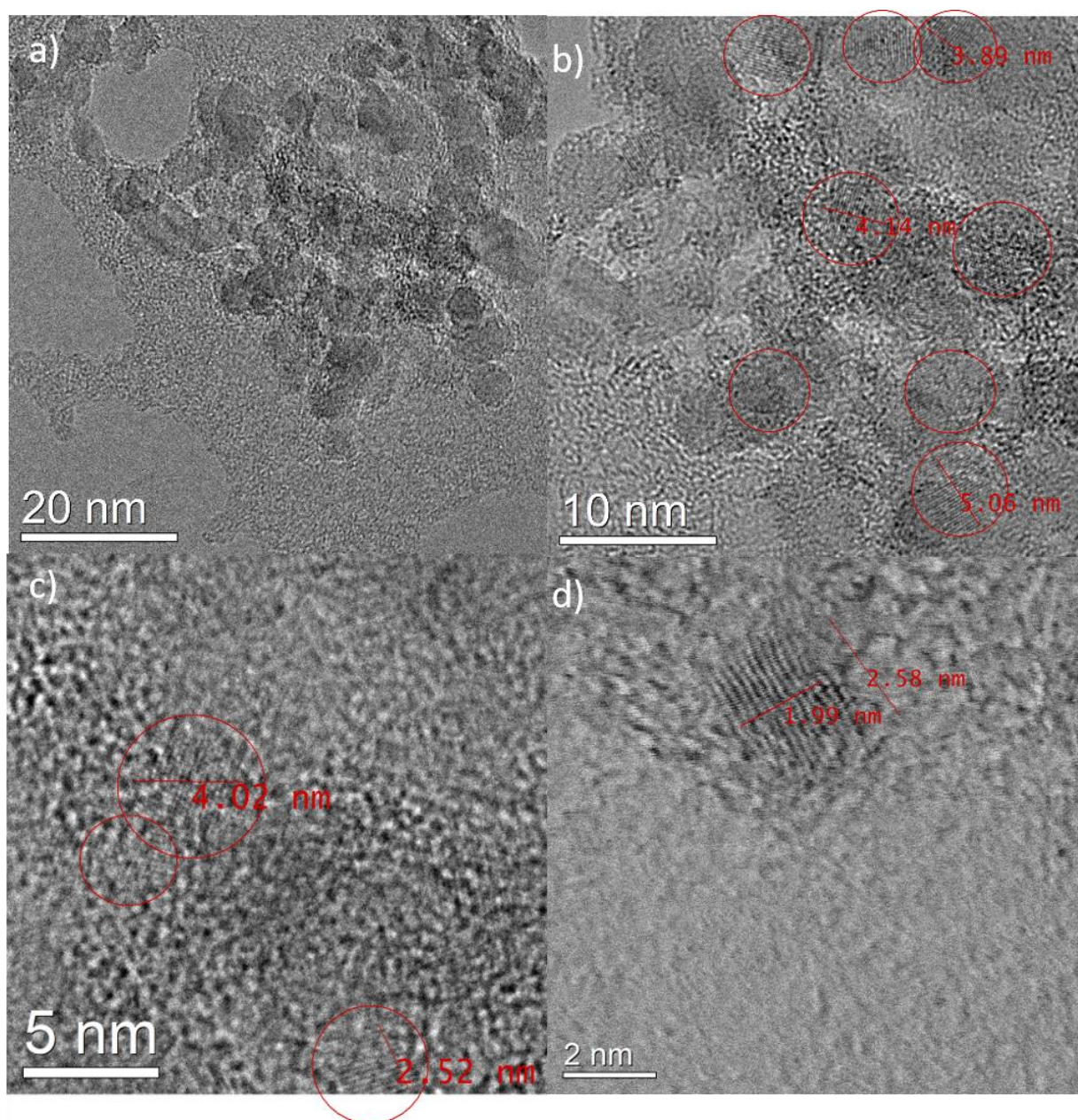


Figure 6.1: HRTEM images of nanodiamonds circled in red with scale bar: a) 20 nm, b) 10 nm, c) 5 nm, and d) 2 nm.

### 6.1.2 Selected area electron diffraction of nanodiamonds

The SAED (methodology described in Chapter 3.2.2.1) pattern of nanodiamonds is presented in Figure 6.2. Nanodiamonds match the typical cubic diamond SAED pattern of characteristic diamond planes with Miller indices (111), (220) and (311) [155].

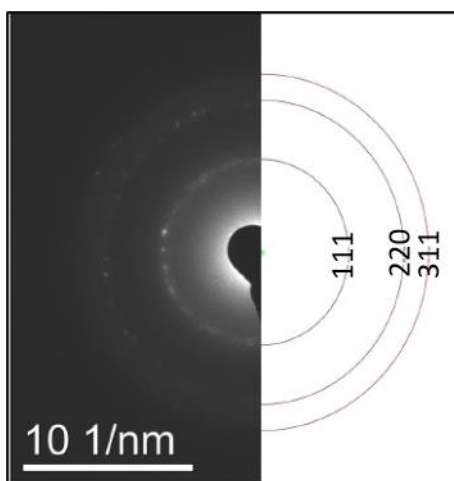


Figure 6.2: The SAED pattern of nanodiamonds with Miller indices (111), (220), (311).

### 6.1.3 Electron energy loss spectroscopy of nanodiamonds

The nanodiamond carbon K-edge EELS (methodology described in Chapter 3.2.2.2) spectrum (Figure 6.3) shows the characteristic diamond peaks at 290, 295 and 304 eV, as well as additional 283 eV peak that is attributed to the graphitic shell that surrounds the nanodiamond particle. The diamond peaks are due to the transition to  $sp^3 - \sigma^*$  transition, while  $sp^2 - \pi^*$  are related to graphitic carbon [156, 157].

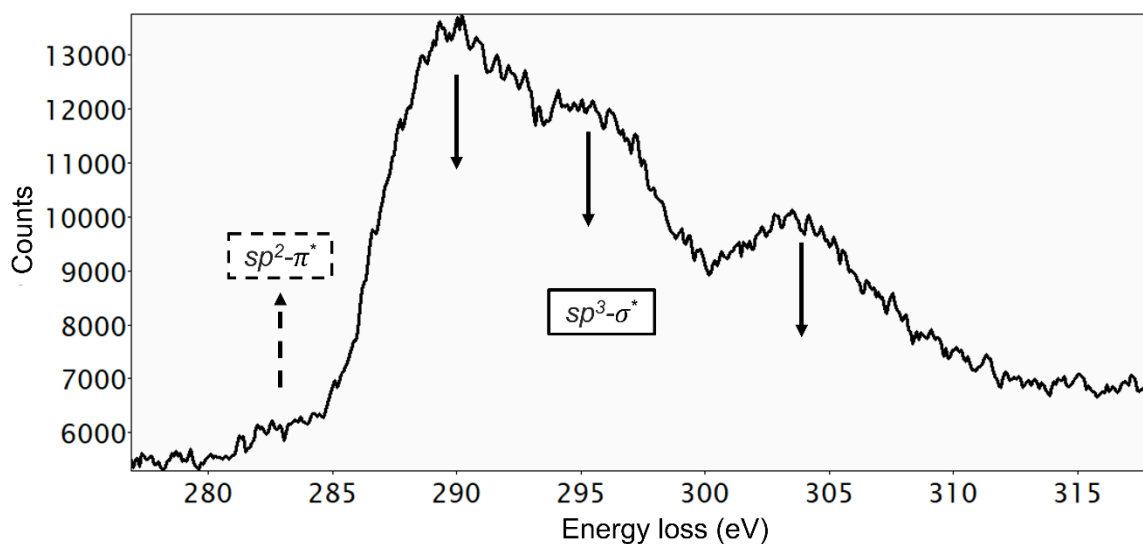


Figure 6.3: The EELS spectrum of carbon K-edge excitation of nanodiamond.

## 6.2 Agglomeration of nanodiamonds upon dilution with DI water

As reported in the literature (Chapter 2), detonation nanodiamond colloids (preparation method described in Chapter 3.1.4) obtained from Nanocarbon Institute (Japan) with positive

Zeta potential are stable with 4 wt% concentration of nanodiamonds, but become unstable with more dilution with DI water, resulting in increase in nanodiamond particle size from ~ 3 nm to ~ 30 nm [98]. However, the stability of these colloids measured with Zeta potential-pH and DLS particles size distribution over time has not yet been reported. The aim of our study is to measure the nanodiamond colloid properties up to 6 days after opening the original 4 wt% of nanodiamonds stock bottle.

### *6.2.1 UV/Visible absorption of nanodiamonds*

The UV/Vis absorption (methodology described in Chapter 3.4.1) spectra of the three nanodiamond colloids with concentrations of 0.2 wt%, 0.25 wt% and 0.3 wt% are shown in Figure 6.4. The peak at the 288 nm is related to the graphitic carbon on the diamond surface and peak shift to higher wavelengths, 290 nm for 0.25 wt% and 295 nm for 0.3 wt% in case of the most concentrated samples, can be accounted to the increased concentration of nanodiamonds  $sp^2$  [142]. This is consistent to EELS spectrum obtained for the nanodiamond particles in Figure 6.3.  $Sp^2$  hybridized carbon on the nanodiamond particle surface can attenuate transmittance by decreasing the bandgap of diamond, which is 5.50 eV, meaning that diamond starts absorbing wavelengths above 225 nm [158].

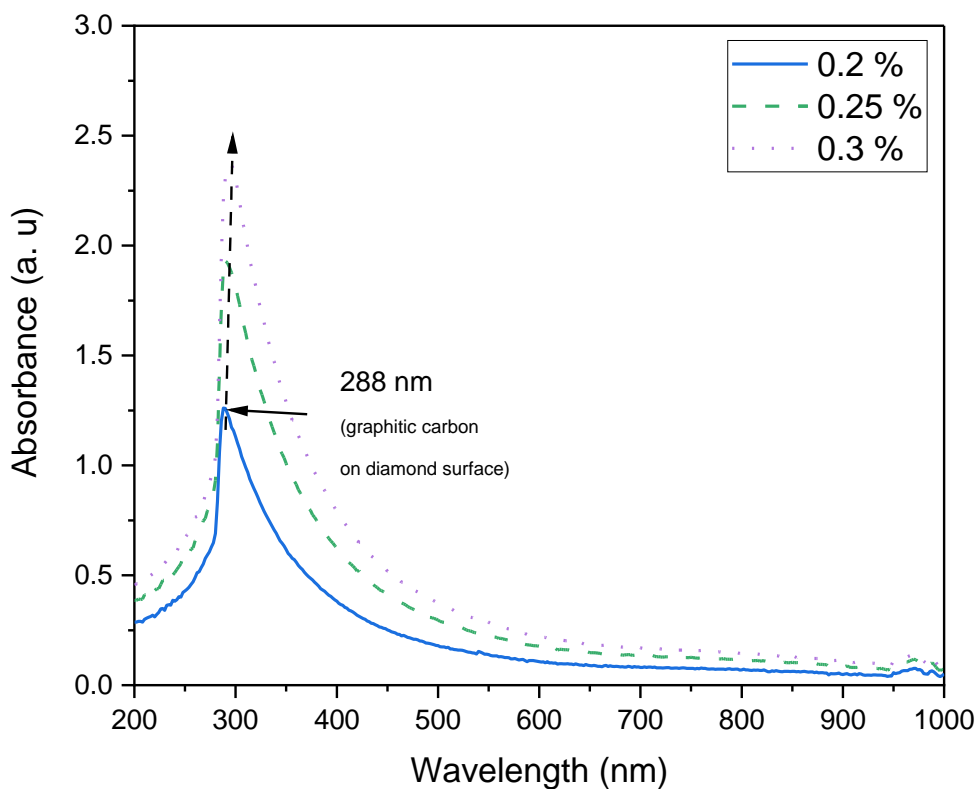


Figure 6.4: UV/Vis absorption of the nanodiamond colloids at different concentrations.

### 6.2.2 The pH and Zeta potential of nanodiamond colloids

Figure 6.5 represents the plot of pH and Zeta potential of original (4 wt%) and the diluted (1 wt%) nanodiamond colloid potential over time (6 days) (methodology described in Chapter 3.6.1). The colloid of nanodiamonds at (4 wt%) show the pH decrease from  $5.19 \pm 0.01$  to  $4.95 \pm 0.01$ , while the zeta potential simultaneously increases from  $40.1 \pm 0.4$  mV to  $43.1 \pm 0.2$  mV from day 1 to day 6, respectively. For the diluted colloid (1 wt%) pH and zeta potential started off with  $5.12 \pm 0.01$  and  $41.7 \pm 0.4$  mV, respectively, and reached a lower pH value of  $4.86 \pm 0.01$  and higher zeta potential value of  $49.4 \pm 1.0$  mV on day 6.

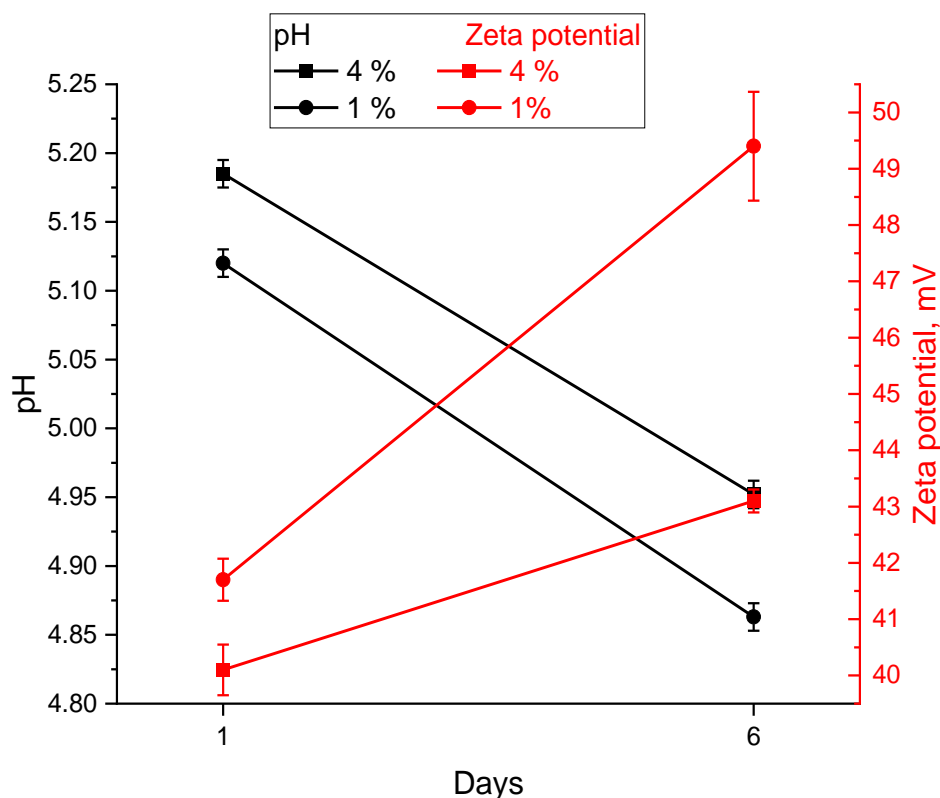
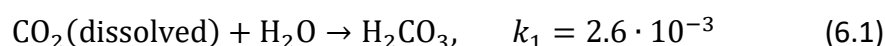


Figure 6.5: pH and Zeta potential of the original (4 wt%) and 1 wt% nanodiamond colloid.

Over time, pH decreases, while the zeta potential increases accordingly for both colloids. For each measurement, pH is lower for the 1 wt% solution compared to the original solution. Likewise, the zeta potential has a greater value for the 1 wt% solution.

One of the properties of carbon dioxide from air is its solubility in DI water/aqueous solutions, it forms a carbonic acid according to equation (6.1). The carbonic acid dissociates in two steps as given in equations (6.2-6.3) by increasing the concentration of  $H^+$  ions that lower the pH of DI water. Therefore, instead of being neutral (pH=7), the DI water is slightly acidic [159, 160].

The formation and dissociation of carbonic acid (at 298 K, 1 atm) [159]:



In other words, CO<sub>2</sub> from air gets absorbed in the solution of nanodiamonds, making it more acidic. This leads to the lowering of the solution's pH, meaning that the concentration of H<sup>+</sup> has increased, which then introduces a larger positive charge and increased repulsion of initially positively charged nanodiamond particles, resulting in an increase in Zeta potential. The colloid measured on the first day showed higher pH (and hence lower zeta potential) than those colloids recorded on day 6. This indicates that the CO<sub>2</sub> content in colloids on day 6 is greater than that on day 1. Similarly, it is assumed that 1 wt% colloids that is more diluted than original colloid, would show the similar behaviour to pH-zeta potential values over time.

According to Zeta potential values that are greater than 30 mV for both 4 wt% and 1 wt% from Figure 6.5, which believed to lead to stable colloids [95], one expects that both nanodiamond colloids are stable over period of 6 days.

### *6.2.3 Dynamic light scattering of nanodiamond colloids*

The DLS particle size measurements (methodology described in Chapter 3.6) (Figure 6.6a) show a slightly bigger average size of nanodiamonds in the 1 wt% colloid (5.0-5.7 nm) than in the original 4 wt% colloid (3.3-3.7 nm) (Table 6.1). The size of the primary diamond particle is suggested to be ~ 3 nm (3.3 nm obtained on day 1 for the original colloid). Particle sizes (> 3 nm) in 1 wt% colloid for both on day 1 and 6 and also in 4 wt% colloid on day 6, are related to the agglomerate size. Figure 6.6b shows the DLS size distribution for the original 4 wt% and diluted 1 wt% nanodiamond colloid for day 1 and 6, where the peaks shift to greater particle sizes for both nanodiamond concentrations on day 6. Similar behavior was reported [23, 98] for detonation nanodiamonds for 5 wt%, 0.3 wt% and 0.01 wt% concentrations, where particle size of  $2.8 \pm 0.6$  nm for 5 wt% increased after dilution to ~ 30 nm for both dilutions.

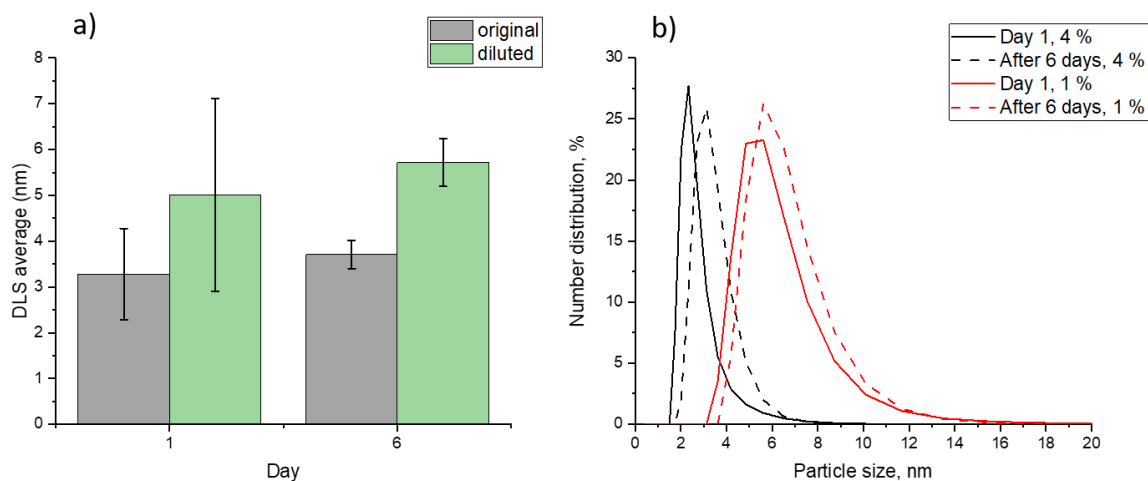


Figure 6.6: a) DLS average particle size, and b) DLS size distribution for original (4 wt%) and diluted (1 wt%) nanodiamond colloids on day 1 and 6.

Table 6.1: DLS particle size of the original (4 %) and 1 % colloid.

Sample	Day 1 DLS particle size, nm	Day 6 DLS particle size, nm
4% (original)	$3.3 \pm 1.0$	$3.7 \pm 0.3$
1%	$5.0 \pm 2.1$	$5.7 \pm 0.5$

It is suggested that the agglomeration of the nanodiamonds in the 1 wt% solution is due to a high concentration of carbonate ions which causes the particles to agglomerate. Namely, positively charged nanodiamonds are surrounded by counter carbonate ions. Even if the Zeta potential is greater than  $\pm 30$  mV, which is usually taken as the boundary for the particle stability in colloids [95], the 1 wt% colloid is not stable. The effect known as the Coulomb depletion effect leads to agglomeration. Repulsive forces between the carbonate ions are greater than the repulsive forces between nanodiamond particles. This causes the depletion zone and the attraction between the same charge particles- nanodiamonds, similar to [95]. The 1 wt% contains more carbonate ions and less particles to oppose the counter charge repulsion forces and agglomerates, while the 4 wt% solution is more stable (has smaller particles).

To conclude, nanoscale diamond particles in form of water colloid are first characterized. It was confirmed by HRTEM that nanodiamonds are  $\sim 2-5$  nm and covered with graphite like carbon ( $sp^2$ ), as expected from the black colour of the colloid. Then, the original 4 wt% dispersion of nanodiamonds in colloid was compared to the 1 wt% (diluted) colloid solution. With high Zeta potentials, the both colloids were thought to be stable over time. However, DLS particle size measurements suggested otherwise, where carbon dioxide was responsible for the pH decrease over time, including its higher content in the diluted sample. The Coulomb depletion effect was introduced to explain the relationship between pH-Zeta potential and DLS size data. With the increased acidity of water in which nanodiamonds are dispersed, the content of  $CO_3^{2-}$  is also increased, which forces like-charged nanodiamonds to agglomerate. Hence, 1 wt% nanodiamond colloid is more prone to destabilize than 4 wt% colloid. Also, this means that over time, the concentration of  $CO_2$  increases and leads to the agglomeration of nanodiamonds in both colloids. In conclusion, the examined nanodiamond colloids are not stable in air.

### 6.3 Nanodiamond-doped silica aerogel

Nanodiamonds characterized in Chapter 6, Sections 6.1 and 6.2 were incorporated in the silica aerogel before gelation (preparation described in Chapter 3.1.5) and the properties of the pure and nanodiamond-doped silica aerogel were assessed. Since the stability of nanodiamonds in colloid is suggested to be compromised over time during exposure to ambient air, doping to silica aerogel, that serves as a matrix for nanodiamonds, can be used to avoid agglomeration.

#### *6.3.1 High resolution transmission electron microscopy of nanodiamond-doped silica aerogel*

The HRTEM (methodology described in Chapter 3.2.2) images of the nanodiamond-doped silica aerogel are given in Figure 6.7. A porous network of silica aerogel can be clearly observed (Figure 6.7a), where the darker parts of the sample are related to higher thickness of the aerogel than to nanodiamond doping. Crystalline nanodiamonds (with particle size of  $\sim 4$  nm) are seen to be incorporated in the silica aerogel (Figure 6.7b). The nanodiamond particles are not agglomerated in the final aerogel and maintain the size as observed in Figure 6.1a-d.

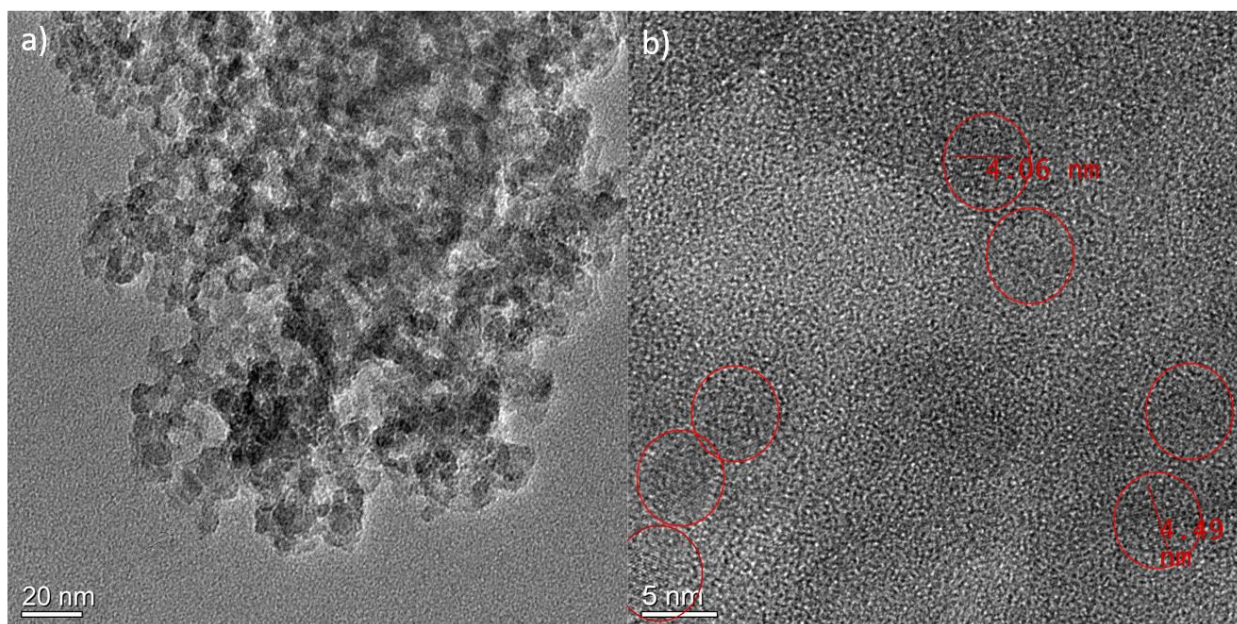


Figure 6.7: HRTEM image of nanodiamond-doped silica aerogel with scale bar: a) 20 nm, and b) 5 nm with nanodiamonds labelled in red.

### 6.3.2 X-ray diffraction of nanodiamond-doped silica aerogel

Figure 6.8 shows the XRD (methodology described in Chapter 3.3) patterns of pure silica aerogel (black) and nanodiamond-doped silica aerogel (red). The broad peak at  $\sim 20\text{-}30^\circ$  corresponds to the amorphous silica [150] observed in both samples, consistent with silica aerogel patterns in Chapter 5.4. In case of the nanodiamond doping, three additional peaks, at  $2\theta$  at  $44^\circ$  are related to (111) plane, at  $75.4^\circ$  to (220) plane and at  $91.4^\circ$  to (311) plane [143], consistent with Chapters 4.5, as well as SAED pattern (see paragraph 6.1.2) for the nanodiamond particles. However, nanodiamond cubic lattice gives rise to broader peaks, due to the nanometer size.

The amount of the diamond in aerogel phase is about 7.5 wt%, which is considerably higher than that obtained in microdiamond-doped silica aerogels in Chapter 5.4 (which was up to 3.3 wt%). Although the nanodiamond concentration (ppm) in the precursor sol in this work was about 8000 ppm when compared to the maximum of 900 ppm in Chapter 5.4, the incorporation of nanodiamonds by such a high concentration in the final silica aerogel can be explained by the size of nanodiamonds ( $\sim 5$  nm) that is significantly smaller and they are much lighter than microdiamonds ( $\sim 500$  nm) used in Chapter 5. Therefore, the silica aerogel

network is less disturbed by the dopant particles, preventing the collapse of the aerogel network and the washing out of the nanodiamonds during solvent exchange.

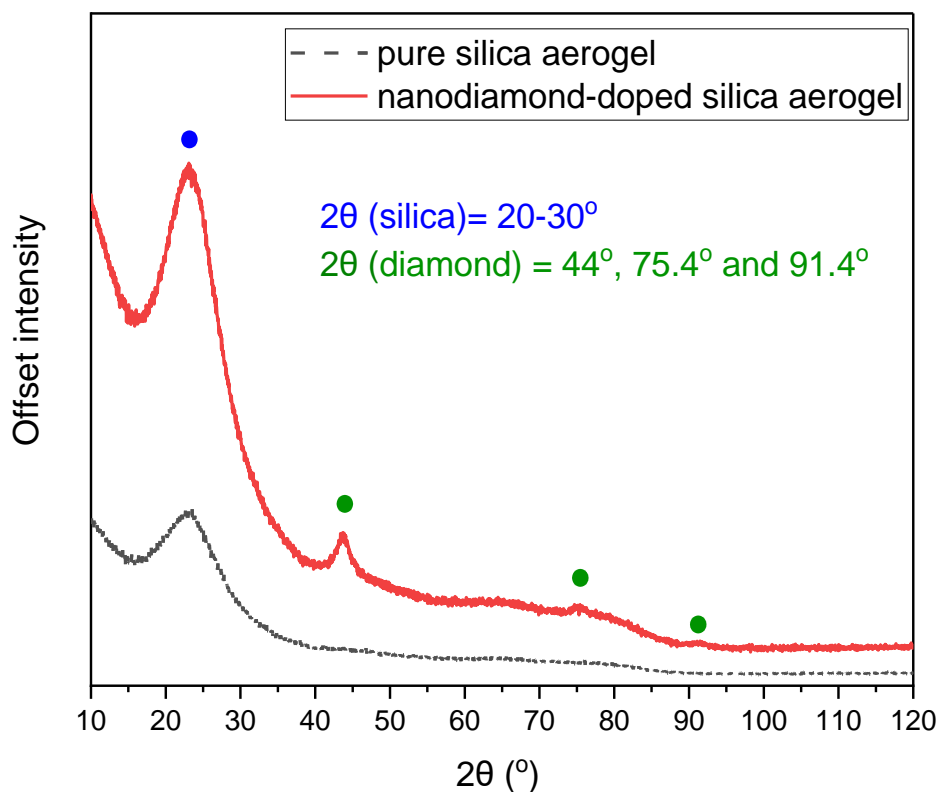


Figure 6.8: XRD patterns of pure silica aerogel (black) and nanodiamond-doped silica aerogel (red).

### 6.3.3 Brunauer-Emmett-Teller and Barrett-Joyner-Halenda theories of nanodiamond-doped silica aerogel

Figure 6.9 and Figure 6.10 show the nitrogen adsorption-desorption isotherms (methodology described in Chapter 3.7) of pure and nanodiamond-doped silica aerogel. The hysteresis loop of the mesoporous isotherms suggests H1 isotherm shape for both aerogels, with open cylindrical mesopores [161]. The two-step desorption isotherm for nanodiamond-doped silica aerogel is due to the presence of blocked pores in otherwise open porosity. It was reported that TEOS could lead to blocked cylindrical mesopores in low pH environment. The part of an open pore is blocked by a silica aerogel microporous plugs so that emptying of the blocked pores takes place at the pressure lower than in case of open pores [162, 163].

The BET surface area, as well as pore specific volume and average pore diameter values are given in Table 6.2 for both pure and nanodiamond-doped aerogel. The nanodiamond-silica aerogel has significantly higher surface area ( $831 \text{ m}^2/\text{g}$ ) compared to the pure silica aerogel ( $506 \text{ m}^2/\text{g}$ ). Also, pore volume and average pore diameter are higher in case of nanodiamond-doped aerogel ( $2.71 \text{ cm}^3/\text{g}$  and  $9.4 \text{ nm}$ ) than that for pure aerogel ( $0.76 \text{ cm}^3/\text{g}$  and  $4.9 \text{ nm}$ ). Moreover, BET surface area results indicate that nanosize of diamond particles is suitable for nanoscale silica aerogel matrix and that it is possible that they enhance/stabilize the porous network formation, rather than dismantling it like in case of microdiamonds (Chapter 5).

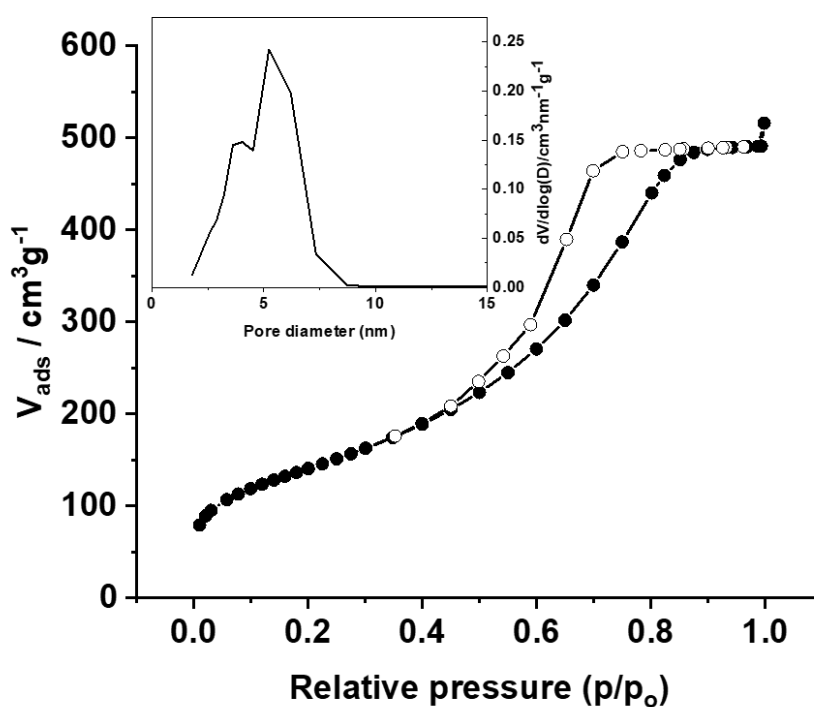


Figure 6.9: The nitrogen adsorption-desorption isotherm of pure silica aerogel with pore size distribution (as insert).

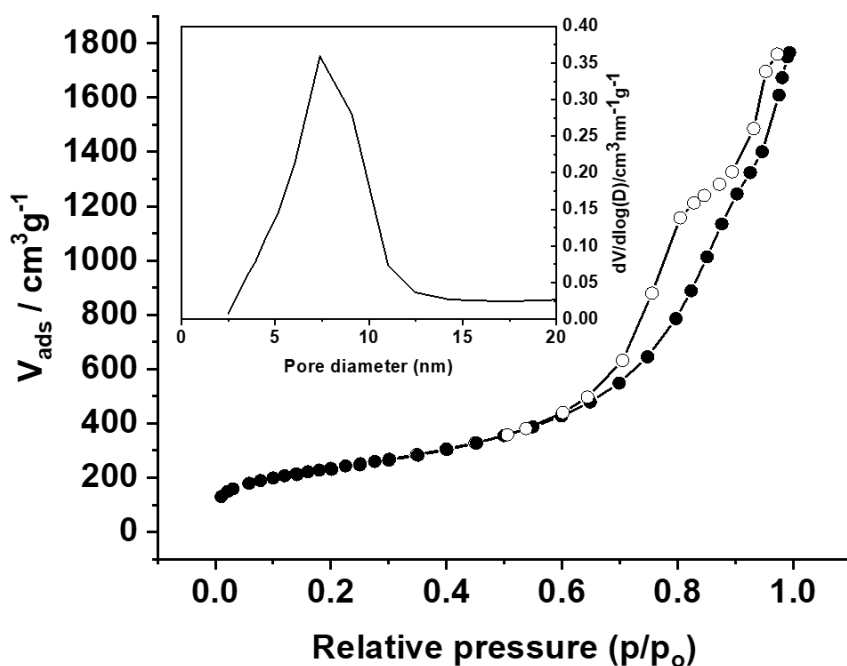


Figure 6.10: The nitrogen adsorption-desorption isotherm of nanodiamond-silica aerogel with pore size distribution (as insert).

Table 6.2: Relationship between with XRD percentage of nanodiamonds in silica aerogel and BET surface area, pore specific volume, average pore diameter and porosity.

Sample	Diamond XRD (wt%) [± 0.1 wt%]	BET surface area, m <sup>2</sup> /g [± 5 m <sup>2</sup> /g]	Specific pore volume, cm <sup>3</sup> /g [± 0.02 cm <sup>3</sup> /g]	Average pore diameter, nm [± 0.1 nm]	Porosity, %
Pure silica aerogel	0	506	0.76	4.9	89.9
Nanodiamond-doped silica aerogel	7.5	831	2.71	9.4	94.5

### 6.3.4 Density of nanodiamond-doped silica aerogel

Table 6.3 shows the skeletal and bulk density of pure and nanodiamond-doped silica aerogel, as well as the calculated porosity (methodology described in Chapter 3.7). The silica aerogel with nanodiamonds has lower bulk density (0.148 g/cm<sup>3</sup>) and higher porosity (94.5 %) compared to the silica aerogel without nanodiamonds (bulk density-0.270 g/cm<sup>3</sup> and porosity- 89.8 %).

*Table 6.3: Relationship between XRD percentage of nanodiamonds in silica aerogel and their skeletal and bulk density, and porosity.*

Sample	Diamond (XRD wt%) [± 0.1 wt%]	Silica (XRD wt%) [± 0.1 wt%]	Skeletal density, g/cm <sup>3</sup>	Bulk density, g/cm <sup>3</sup> [± 0.001 g/cm <sup>3</sup> ]	Porosity, %
Pure silica aerogel	0	100	2.65	0.270	89.8
Nanodiamond- doped silica aerogel	7.5	92.5	2.71	0.148	94.5

\*Diamond skeletal density is taken as 3.51 g/cm<sup>3</sup> [8] and silica skeletal density as 2.65 g/cm<sup>3</sup> [137].

The diamond doping of silica aerogels with nano- and micro-sized particles in terms of BET surface area and bulk density is presented in Figure 6.11 (discussed in Chapter 5 and 6). While microdiamonds decrease the BET surface area and increase the bulk density of the pure silica aerogel, nanodiamonds simultaneously increase the surface area and decrease the bulk density of the pure aerogel. Due to low weight of nanodiamonds in silica aerogels, it is suggested the nanodiamond-doped silica aerogel will stay longer in the atmosphere before settling down compared to both pure and microdiamond-doped aerogels.

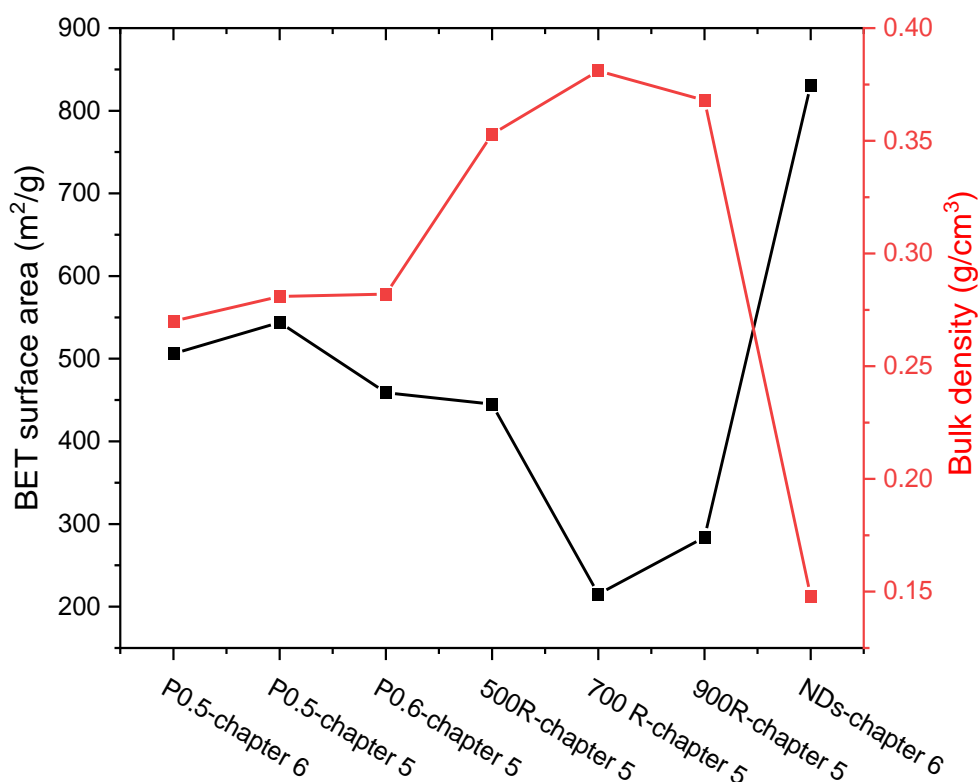


Figure 6.11: BET surface area and bulk density of pure, micro- and nanodiamond-doped silica aerogels discussed in Chapter 5 and 6.

#### 6.4 Conclusion

pH-Zeta potentials measurements and DLS data suggest that dilution of the original nanodiamond stock of 4 wt% in DI water would lead to nanoparticle agglomeration, possibly due to the increase in carbonate ion concentration. UV/Vis data of nanodiamonds show the strong absorption in the recorded range confirmed that these diamonds are not suitable for solar scattering application. Nevertheless, it is helpful to be able to compare the properties of the aerogels doped with micro- and nanodiamonds, which have different surface properties and particle size. The small size of detonation nanodiamonds is used and their doping and distribution in the silica aerogel matrix is studied. In this chapter nanodiamonds are successfully doped into silica aerogel. Nanodiamonds remained non-agglomerated in the final aerogel that exhibited high surface area and porosity and low bulk density. XRD showed amorphous silica aerogel structure, with crystalline diamond peaks. Also, the concentration of the diamond phase was  $\sim 7.5\%$ , which is an increase in doping concentration compared to

the microdiamond doping presented in Chapter 5. The BET surface area strongly suggests that the similar sizes of nanodiamond dopant and silica nanosize particles lead to an aerogel with higher surface area compared to the microdiamond-doped aerogel from Chapter 5. In conclusion, higher surface area and porosity with lower bulk density of the nanodiamond-doped aerogel in comparison with microdiamond doping could be beneficial for solar aerosol application if the graphitic layer from nanodiamonds can be removed. Furthermore, it is proposed that the nanoparticles could be protected from moisture in the silica matrix but still retain their optical properties in case fluorescent nanodiamonds are used.

## Chapter 7 Conclusion and future work

### 7.1 Summary

The global warming mainly due to CO<sub>2</sub> emissions is a pressing issue of the world today. Cutting down the green gas emission and shifting to greener energy sources has not been as swift and productive as of yet. Aerosol injection as one of the geoengineering methods to fight climate change has been assessed by theoretical models to be the most cost-effective technique with a potential to be developed and employed quickly. Good solar scatterers should have high up-scattering in the UV/Vis range in order to scatter back the radiation coming from Sun, while transmitting in the IR, which is the region the Earth radiates its energy. The aim of this thesis was to synthesize a novel composite material- diamond-doped silica aerogel with a goal to use it as solar scatterer, which is believed to have the qualities to outperform other materials proposed in the literature. Namely, diamond is an amazing light scatterer with high refractive index (2.41) and no IR absorption, while silica aerogel is very light and suitable for hosting various dopants. In the literature, silica aerogel is a material of choice for nanoparticles when nanoparticles need to be accessible in the matrix, but porosity and low weight of the aerogel are utilised here. Our synthesis experiments and experimental optical measurements conducted for this work are the first attempt to experimentally study such proposed solar scatterers. Moreover, our diamond/silica aerogel concept has never been reported for the solar geoengineering in the literature before.

Two types of diamonds were studied: HPHT microdiamonds (0-2 μm in size) and DNDs (2-5 nm in size), before adding the diamond phase to the silica aerogels before the gelation. HPHT microdiamonds were shaken with zirconia beads and 1-undecene and the properties of microdiamond powders before and after the treatment were compared. Nanodiamonds were purchased from NanoCarbon Institute (Japan) as 4 wt% nanodiamond colloid, and the properties of the original and diluted to 1 wt% nanodiamond colloid were compared. Raw microdiamonds and nanodiamonds are separately added to the silica aerogel and the effect of doping was evaluated for both composites. All silica aerogels were prepared using TEOS as precursor using ambient pressure drying method.

According to FTIR and NMR spectroscopy in Chapter 4, treated HPHT microdiamonds are terminated with alkyl groups unlike the raw microdiamond powder. The DLS particle size

shifts to narrower distribution towards smaller particle size (average size  $\sim 552$  to  $\sim 507$  nm). Additionally, shape of microdiamonds is irregular with sharp edges unrelated to the shaking treatment (according to SEM and TEM). XRD and Raman spectroscopy suggest high purity of both microdiamond powders, where microdiamond have no impurities except for zirconium oxide in case of treated microdiamonds due to shaking with beads, and the graphitic carbon is not present even after shaking.

Chapter 5 showed doping of silica aerogels with HPHT microdiamonds with three different concentrations- 500, 700 and 900 ppm in the silica precursor before gelation, which respectively led to 2.8, 3 and 3.3 wt% of diamond phase in the final aerogels. The BET surface area for the microdiamond-doped aerogel was in the range of 215-445 m<sup>2</sup>/g, whereas for the pure aerogels the surface area was 459-544 m<sup>2</sup>/g. The bulk density was  $\sim 0.353$ - $0.381$  g/cm<sup>3</sup> and  $\sim 0.281$  g/cm<sup>3</sup> for the microdiamond-doped and pure silica aerogels, respectively. Additionally, the low density and hence slower fall speed before sedimentation of pure and microdiamond-doped aerogels would allow these aerogel-based aerosols to stay in the atmosphere for a longer time ( $\sim 9$  and 6.9 years, for the pure and the 900 ppm microdiamond-doped silica aerogel, respectively) compared to the pure microdiamond particles ( $\sim 2.9$  years), meaning these aerosols can scatter sunlight for longer period of time after injecting in the stratosphere. TEM images showed that microdiamond particles ( $\sim 500$  nm) are incorporated in  $\sim 1$   $\mu$ m aerogel particle, which is desirable due to the lowest inhalation of PM<sub>2.5</sub> hazardous small particles that is in 0.1-1  $\mu$ m particle range.

The doped silica aerogel with the highest wt% of raw HPHT microdiamonds was chosen for the diffuse reflectance measurements, along with the pristine silica aerogel and pure microdiamond powder as a reference. The composite microdiamond/silica aerogel has the improved reflectance in the UVA/UVB compared to the pure silica and in the NIR compared to the pure microdiamond powder.

In Chapter 6 nanodiamonds tend to agglomerate when the concentration of nanodiamonds in the colloid is diluted from the original 4 wt% to 1 wt%. Furthermore, when the stock bottle with the original 4 wt% is opened, the Zeta potential, pH and DLS measurements suggest that after 6 days, the agglomeration occurs for both 4 wt% and 1 wt% colloids. It is proposed that CO<sub>2</sub> from air causes the pH to decrease (become more acidic), introducing CO<sub>3</sub><sup>2-</sup> in the solution which act as counterions. In sufficient concentration, these counterions to the positive

nanodiamond particles lead to depletion of charge between diamond particles and ultimately to agglomeration. Additionally, detonation nanodiamond-doped silica aerogels were successfully prepared and dispersed nanodiamonds in silica matrix were observed using HRTEM.

According to XRD, 7.5 wt% of nanodiamonds are incorporated to silica aerogel, while only up to 3.3 wt% of microdiamonds are found in the final silica aerogel. Also, the BET surface and bulk density of the nanodiamond-doped silica aerogel is improved compared to the microdiamond-doped silica aerogel. Namely, doping with nanodiamonds led to higher surface area and lower bulk density than that in case of microdiamonds. Interestingly, nanodiamond/silica composite had higher surface area (831 m<sup>2</sup>/g) and lower bulk density (0.148 g/cm<sup>3</sup>) than pure silica aerogel. Finally, the porosity of all synthesized silica aerogels in this thesis (pure, nano- and microdiamond-doped aerogels) is in the range of 85.8-94.5 %.

Ultimately, our study shows that the proposed diamond/silica aerogel is promising for use as a solar scatterer as a light and efficient scatterer in the UV/Vis/NIR region. Both materials are produced commercially on large scale. Also, this is the first experimental evaluation of the scatterer material for geoengineering application, and due to encouraging results further studies are recommended in order to advance towards the proposed application.

## 7.2 Future recommendations

Size selection of microdiamonds and silica aerogel particles by grinding would give insight in dependency of both diamond and silica sizes on reflectance data. Also, the use of nanodiamonds without graphitic sp<sup>2</sup> shell for doping and reflectance measurement is recommended, since graphitic shell is found to absorb in the UV/Vis range where the solar scattering should be substantial in order for scattering and cooling effect to be possible, without a compensation for the IR absorption that would minimize the cooling of the Earth's surface. Evaluation of scattering of different sizes of diamond particles in aerogels is suggested since nanodiamonds can be incorporated by higher wt% than microdiamonds. Nevertheless, diamond particles sizes proposed in the theoretical model are greater than a few nanometres, measuring the reflectance properties of nanodiamond/silica aerogel is suggested to give a valuable insight and assess the theoretical predictions.

The optical transmission measurement of the pure diamonds, pure and the doped aerogels is suggested in order to study the behaviour of the diamond/silica composite in the IR radiation range. Since pure bulk diamond does not absorb in the IR, the diamond-doped silica aerogels is suggested to have the improved transmittance compared to the pure silica aerogel.

The use of TMOS (higher transparency of TEOS precursor) or co-precursor (TEOS/MTMS) (hydrophobic aerogel) or silylation of TEOS aerogel to make it hydrophobic is recommended because the hydrophobic material is desirable for solar scattering due to such materials being unable to catalyse the depletion of ozone. Furthermore, the stratospheric chemistry should be examined since both diamond and silica are not naturally present in the atmosphere unlike sulfate aerosols originating from the volcanic eruptions.

The future work also includes exploration of different applications of diamond-doped aerogels, such as functionalization of HPHT fluorescent diamonds and evaluation of fluorescent properties before and after the treatment. Silica aerogel is a good host of nanoparticles and is transparent and hence suitable for optically active dopants. Alkyl groups on the fluorescent particle surface are reported to influence the decay time of the fluorescence. Also, adding fluorescent nanodiamonds to the silica aerogel transparent and porous matrix could prevent nanodiamond agglomeration upon drying or in the colloid over time, allowing nanodiamonds to keep their optical properties without any light attenuation from the silica host.

## References

1. *Geoengineering the climate Science, governance and uncertainty*. 2009, The Royal Society: London.
2. Gomes, M.S.d.P. and M.S.M. de Araújo, *Artificial cooling of the atmosphere—A discussion on the environmental effects*. *Renewable and Sustainable Energy Reviews*, 2011. **15**(1): p. 780-786.
3. Robock, A. *Stratospheric aerosol geoengineering*. in *AIP Conference Proceedings*. 2015. American Institute of Physics Inc.
4. Crutzen, P.J., *Albedo Enhancement by Stratospheric Sulfur Injections: A Contribution to Resolve a Policy Dilemma?* *Climatic Change*, 2006. **77**(3-4): p. 211-220.
5. McNeill, V.F., *Atmospheric Aerosols: Clouds, Chemistry, and Climate*. *Annual Review of Chemical and Biomolecular Engineering*, 2017. **8**: p. 427-444.
6. Weisenstein, D.K., D.W. Keith, and J.A. Dykema, *Solar geoengineering using solid aerosol in the stratosphere*. *Atmospheric Chemistry and Physics*, 2015. **15**(20): p. 11835-11859.
7. Pope, F.D., et al., *Stratospheric aerosol particles and solar-radiation management*. *Nature Climate Change*, 2012. **2**(10): p. 713-719.
8. Dykema, J.A., D.W. Keith, and F.N. Keutsch, *Improved aerosol radiative properties as a foundation for solar geoengineering risk assessment*. *Geophysical Research Letters*, 2016. **43**(14): p. 7758-7766.
9. Keith, D.W., et al., *Stratospheric solar geoengineering without ozone loss*. *Proceedings of the National Academy of Sciences of the United States of America*, 2016. **113**(52): p. 14910-14914.
10. Group, K. *SCoPEX: Stratospheric Controlled Perturbation Experiment*. 2021 [11.02.2021]; Available from: <https://www.keutschgroup.com/scopex>.
11. Mochalin, V.N., et al., *The properties and applications of nanodiamonds*. *Nature Nanotechnology*, 2011. **7**(1): p. 11-23.
12. Maleki, H., L. Durães, and A. Portugal, *An overview on silica aerogels synthesis and different mechanical reinforcing strategies*. *Journal of Non-Crystalline Solids*, 2014. **385**: p. 55-74.

13. Wordsworth, R., L. Kerber, and C. Cockell, *Enabling Martian habitability with silica aerogel via the solid-state greenhouse effect*. *Nature Astronomy*, 2019. **3**(10): p. 898-903.
14. Strobach, E., et al., *High temperature stability of transparent silica aerogels for solar thermal applications*. *APL Materials*, 2019. **7**(8): p. 081104.
15. Ziegler, C., et al., *Modern Inorganic Aerogels*. *Angewandte Chemie*, 2017. **56**(43): p. 13200-13221.
16. Lamy-Mendes, A., R.F. Silva, and L. Duraes, *Advances in carbon nanostructure–silica aerogel composites: a review*. *Journal of Materials Chemistry A*, 2018. **6**(4): p. 1340-1369.
17. Benson, J.M., *Safety consideration when handling metal powders*. *The Journal of The Southern African Institute of Mining and Metallurgy*, 2012. **112**(7): p. 563-575.
18. Han, X., et al., *Bioinspired Synthesis of Monolithic and Layered Aerogels*. *Advanced Materials*, 2018. **30**(23): p. e1706294.
19. De Pooter, S., et al., *Optimized synthesis of ambient pressure dried thermal insulating silica aerogel powder from non-ion exchanged water glass*. *Journal of Non-Crystalline Solids*, 2018. **499**: p. 217-226.
20. Zhao, S., et al., *Phase transfer agents facilitate the production of superinsulating silica aerogel powders by simultaneous hydrophobization and solvent- and ion-exchange*. *Chemical Engineering Journal*, 2020. **381**: p. 122421.
21. Jacobson, M.Z., *Fundamentals of Atmospheric Modeling*. 2005: Cambridge University Press.
22. de Weerd, C., et al., *Comparison of the Optical Properties of Graphene and Alkyl-terminated Si and Ge Quantum Dots*. *Scientific Reports*, 2017. **7**(1): p. 14463.
23. McHedlov-Petrosyan, N.O., et al., *The Properties of 3 nm-Sized Detonation Diamond from the Point of View of Colloid Science*. *Ukrainian Journal of Physics*, 2015. **60**(9): p. 932-937.
24. United Nations Environment Programme, *Emissions Gap Report 2018*. 2018.
25. IPCC, *Climate Change 2014: Synthesis Report. Contribution of Working Groups I, II and III to the Fifth Assessment Report of the Intergovernmental Panel on Climate Change*, R.K.P.a.L.A.M.e. Core Writing Team, Editor. 2014: Geneva, Switzerland.

26. Satheesh, S. and K. Krishnamoorthy, *Radiative effects of natural aerosols: A review*. Atmospheric Environment, 2005. **39**(11): p. 2089-2110.
27. Visioni, D., G. Pitari, and V. Aquila, *Sulfate geoengineering: a review of the factors controlling the needed injection of sulfur dioxide*. Atmospheric Chemistry and Physics, 2017. **17**(6): p. 3879-3889.
28. Change, U.N.F.C.o.C. *The Paris Agreement*. 2021 [29.05.2021]; Available from: <https://unfccc.int/process-and-meetings/the-paris-agreement/the-paris-agreement>.
29. GeoExPro. *Recent Advances in Climate Change Research: Part I - Blackbody Radiation and Milankovic Cycles*. 2021 [04.11.2021]; Available from: <https://www.geoexpro.com/articles/2019/08/recent-advances-in-climate-change-research-part-i-blackbody-radiation-and-milankovic-cycles>.
30. Budyko, M.I., *Climate and Life*. Vol. 18. 1974, New York: Academic Press.
31. OpenStax. *Total Internal Reflection*. 2020 [29.05.2021]; Available from: <https://phys.libretexts.org/@go/page/4488>
32. Keith, D.W., *Photophoretic levitation of engineered aerosols for geoengineering*. Proceedings of the National Academy of Sciences of the United States of America, 2010. **107**(38): p. 16428-16431.
33. Huynh, H.N. and V.F. McNeill, *Heterogeneous Chemistry of CaCO<sub>3</sub> Aerosols with HNO<sub>3</sub> and HCl*. The Journal of Physical Chemistry A, 2020. **124**(19): p. 3886-3895.
34. Aegerter, M., N. Leventis, and M. Koebel, *Aerogels Handbook*. Advances in Sol-Gel Derived Materials and Technologies. 2011, New York: Springer.
35. Zinzi, M., et al., *Optical and visual experimental characterization of a glazing system with monolithic silica aerogel*. Solar Energy, 2019. **183**: p. 30-39.
36. Rubin, M. and C.M. Lampert, *Transparent silica aerogels for window insulation*. Solar Energy Materials, 1983. **7**(4): p. 393.
37. Berardi, U., *Development of Glazing Systems with Silica Aerogel*. Energy Procedia, 2015. **78**: p. 394-399.
38. Buratti, C. and E. Moretti, *Experimental performance evaluation of aerogel glazing systems*. Applied Energy, 2012. **97**: p. 430-437.
39. Zhao, L., et al., *Modeling silica aerogel optical performance by determining its radiative properties*. AIP Advances, 2016. **6**(2): p. 025123.

40. Wang, J., D. Petit, and S. Ren, *Transparent thermal insulation silica aerogels*. *Nanoscale Advances*, 2020. **2**(12): p. 5504-5515.
41. Soleimani Dorcheh, A. and M.H. Abbasi, *Silica aerogel; synthesis, properties and characterization*. *Journal of Materials Processing Technology*, 2008. **199**(1-3): p. 10-26.
42. Smitha, S., et al., *Effect of aging time and concentration of aging solution on the porosity characteristics of subcritically dried silica aerogels*. *Microporous and Mesoporous Materials*, 2006. **91**(1-3): p. 286-292.
43. Shlyakhtina, A.V. and Y.-J. Oh, *Transparent SiO<sub>2</sub> aerogels prepared by ambient pressure drying with ternary azeotropes as components of pore fluid*. *Journal of Non-Crystalline Solids*, 2008. **354**(15): p. 1633-1642.
44. Prakash, S.S., et al., *Erratum: Silica aerogel films prepared at ambient pressure by using surface derivatization to induce reversible drying shrinkage*. *Nature*, 1995. **375**(6530): p. 431-431.
45. Kanamori, K., et al., *New Transparent Methylsilsesquioxane Aerogels and Xerogels with Improved Mechanical Properties*. *Advanced Materials*, 2007. **19**(12): p. 1589-1593.
46. Khedkar, M.V., et al., *Physicochemical properties of ambient pressure dried surface modified silica aerogels: effect of pH variation*. *SN Applied Sciences*, 2020. **2**(4).
47. Iswar, S., et al., *Effect of aging on silica aerogel properties*. *Microporous and Mesoporous Materials*, 2017. **241**: p. 293-302.
48. Gurav, J.L., et al., *Silica Aerogel: Synthesis and Applications*. *Journal of Nanomaterials*, 2010. **2010**: p. 1-11.
49. Wagh, P.B., et al., *Comparison of some physical properties of silica aerogel monoliths synthesized by different precursors*. *Materials Chemistry and Physics* 1999. **57**: p. 214-218.
50. Venkateswara Rao, A., A. Parvathy Rao, and M.M. Kulkarni, *Influence of gel aging and Na<sub>2</sub>SiO<sub>3</sub>/H<sub>2</sub>O molar ratio on monolithicity and physical properties of water-glass-based aerogels dried at atmospheric pressure*. *Journal of Non-Crystalline Solids*, 2004. **350**: p. 224-229.

51. Pisal, A.A. and A. Venkateswara Rao, *Development of hydrophobic and optically transparent monolithic silica aerogels for window panel applications*. Journal of Porous Materials, 2016. **24**(3): p. 685-695.
52. Schwertfeger, F., D. Frank, and M. Schmidt, *Hydrophobic waterglass based aerogels without solvent exchange or supercritical drying*. Journal of Non-Crystalline Solids, 1998. **225**: p. 24-29.
53. Lee, C.J., G.S. Kim, and S.H. Hyun, *Synthesis of silica aerogels from waterglass via new modified ambient drying*. Journal of Materials Science 2002. **37**: p. 2237-2241.
54. Bangi, U.K., A. Venkateswara Rao, and A. Parvathy Rao, *A new route for preparation of sodium-silicate-based hydrophobic silica aerogels via ambient-pressure drying*. Science and Technology of Advanced Materials, 2008. **9**(3): p. 035006.
55. Liu, Y., et al., *Effect of sodium bicarbonate solution on methyltrimethoxysilane-derived silica aerogels dried at ambient pressure*. Frontiers of Chemical Science and Engineering, 2021. **15**: p. 954–959.
56. Lu, J., et al., *Morphology control of nickel nanoparticles prepared in situ within silica aerogels produced by novel ambient pressure drying*. Scientific Reports, 2020. **10**(1): p. 11743.
57. Parale, V.G., et al., *Ambient pressure dried tetrapropoxysilane-based silica aerogels with high specific surface area*. Solid State Sciences, 2018. **75**: p. 63-70.
58. Rao, A.V. and D. Haranath, *Effect of methyltrimethoxysilane as a synthesis component on the hydrophobicity and some physical properties of silica aerogels*. Microporous and Mesoporous Materials, 1999. **30**: p. 267–273.
59. Pan, Y., et al., *Low thermal-conductivity and high thermal stable silica aerogel based on MTMS/Water-glass co-precursor prepared by freeze drying*. Materials & Design, 2017. **113**: p. 246-253.
60. Nah, H.-Y., et al., *Comparisional studies of surface modification reaction using various silylating agents for silica aerogel*. Journal of Sol-Gel Science and Technology, 2020. **96**(2): p. 346-359.
61. Sorensen, L., G.F. Strouse, and A.E. Stiegman, *Fabrication of Stable Low-Density Silica Aerogels Containing Luminescent ZnS Capped CdSe Quantum Dots*. Advanced Materials, 2006. **18**(15): p. 1965-1967.

62. Zhou, D., et al., *Conquering Aggregation-Induced Solid-State Luminescence Quenching of Carbon Dots through a Carbon Dots-Triggered Silica Gelation Process*. *Chemistry of Materials*, 2017. **29**(4): p. 1779-1787.
63. Inam, F., et al., *Emission and Nonradiative Decay of Nanodiamond NV Centers in a Low Refractive Index Environment*. *ACS Nano*, 2013. **7**: p. 3833–3843.
64. Nor, R.M., et al., *Diamond: Synthesis, Characterisation and Applications*, in *Carbon and Oxide Nanostructures*. 2010, Springer: Berlin, Heidelberg. p. 195-217.
65. Dreyer, D.R., et al., *The chemistry of graphene oxide*. *Chemical Society Reviews*, 2010. **39**(1): p. 228-40.
66. Chung, D.D.L., *Review Graphite*. *Journal of Materials Science*, 2002. **37**: p. 1475– 1489.
67. University, R. *Hybrid Atomic Orbitals*. 2021 [07.06.2021]; Available from: <https://openstax.org/books/chemistry-2e/pages/8-2-hybrid-atomic-orbitals>.
68. Zare, K. and M.A. Malkeshi, *Effect of catalyst on growth of diamond by plasma-enhanced chemical vapor deposition*. *Journal of Nanostructure in Chemistry*, 2013. **27**(3): p. 1-5.
69. Tropf, J.W. and E.M. Thomas, *Optical Properties of Diamond*. *Johns Hopkins APL Technical Digest*, 1993. **14**: p. 16-23.
70. Edwards, D.F. and E. Ochoa, *Infrared refractive index of diamond*. *Optical Society of America*, 1981. **71**: p. 607-608.
71. Energy, N. *Top five diamond mining countries in the world*. 2021 [04.11.2021]; Available from: <https://www.nsenenergybusiness.com/news/top-diamond-mining-countries-world/>.
72. Khmel'nitskiy, R.A., *Prospects for the synthesis of large single-crystal diamonds*. *Physics-Usp'ekhi*, 2015. **58**(2): p. 134-149.
73. Danilenko, V.V., *On the History of the Discovery of Nanodiamond Synthesis*. *Physics of the Solid State*, 2004. **46**(4): p. 595–599.
74. Arnault, J.-C., *Nanodiamonds: Advanced Material Analysis, Properties and Applications*. In *Micro and Nano Technologies*. 2017, Amsterdam, Netherlands: Elsevier.
75. Sun, H., et al., *Reducing GaN-on-diamond interfacial thermal resistance for high power transistor applications*. *Applied Physics Letters*, 2015. **106**(11): p. 111906.

76. Sumiya, H. and S. Satoh, *High-pressure synthesis of high-purity diamond crystal*. *Diamond and Related Materials*, 1996. **5**: p. 1359-1365.
77. Li, Y.-D., et al., *Effects of catalyst height on diamond crystal morphology under high pressure and high temperature*. *Chinese Physics B*, 2016. **25**(4): p. 048103.
78. Yeganeh, M., et al., *Atomic hydrogen treatment of nanodiamond powder studied with photoemission spectroscopy*. *Physical Review B*, 2007. **75**(15): p. 155404.
79. Krüger, A., et al., *Unusually tight aggregation in detonation nanodiamond: Identification and disintegration*. *Carbon*, 2005. **43**(8): p. 1722-1730.
80. Osswald, S., et al., *Control of  $sp^2/sp^3$  Carbon Ratio and Surface Chemistry of Nanodiamond Powders by Selective Oxidation in Air*. *Journal of the American Chemical Society*, 2006. **128**(35): p. 11635-11642.
81. Astuti, Y., et al., *Evaporation and alignment of 1-undecene functionalised nanodiamonds*. *Journal of Luminescence*, 2014. **156**: p. 41-48.
82. Stehlik, S., et al., *Size and Purity Control of HPHT Nanodiamonds down to 1 nm*. *The Journal of Physical Chemistry C*, 2015. **119**(49): p. 27708-27720.
83. Krueger, A. and D. Lang, *Functionality is Key: Recent Progress in the Surface Modification of Nanodiamond*. *Advanced Functional Materials*, 2012. **22**(5): p. 890-906.
84. Xu, K. and Q. Xue, *A new method for deaggregation of nanodiamond from explosive detonation, Graphitization-oxidation method*. *Physics of the Solid State*, 2004. **46**(4): p. 633-634.
85. Ackermann, J. and A. Krueger, *Efficient surface functionalization of detonation nanodiamond using ozone under ambient conditions*. *Nanoscale*, 2019. **11**(16): p. 8012-8019.
86. Jung, H.S. and K.C. Neuman, *Surface Modification of Fluorescent Nanodiamonds for Biological Applications*. *Nanomaterials*, 2021. **11**(1): p. 1-23.
87. Gibson, N., et al., *Colloidal stability of modified nanodiamond particles*. *Diamond and Related Materials*, 2009. **18**(4): p. 620-626.
88. Krueger, A., et al., *Deagglomeration and functionalisation of detonation diamond*. *physica status solidi (a)*, 2007. **204**(9): p. 2881-2887.
89. Eidelman, E.D., et al., *A stable suspension of single ultrananocrystalline diamond particles*. *Diamond and Related Materials*, 2005. **14**(11-12): p. 1765-1769.

90. Pentecost, A., et al., *Deaggregation of nanodiamond powders using salt- and sugar-assisted milling*. ACS Applied Materials & Interfaces, 2010. **2**(11): p. 3289-3294.
91. Turcheniuk, K., et al., *Salt-Assisted Ultrasonic Deaggregation of Nanodiamond*. ACS Applied Materials & Interfaces, 2016. **8**(38): p. 25461-25468.
92. Shenderova, O.A., et al., *Review Article: Synthesis, properties, and applications of fluorescent diamond particles*. Journal of Vacuum Science & Technology B, Nanotechnology and Microelectronics: Materials, Processing, Measurement, and Phenomena, 2019. **37**(3): p. 030802.
93. Shenderova, O.A. and G.E. McGuire, *Science and engineering of nanodiamond particle surfaces for biological applications (Review)*. Biointerphases, 2015. **10**(3): p. 030802.
94. Abdullahi, I.M., et al., *Explosive Fragmentation of Luminescent Diamond Particles*. Carbon, 2020. **164**: p. 442-450.
95. Petit, T., et al., *Surface transfer doping can mediate both colloidal stability and self-assembly of nanodiamonds*. Nanoscale, 2013. **5**(19): p. 8958-8962.
96. Gines, L., et al., *Positive zeta potential of nanodiamonds*. Nanoscale, 2017. **9**(34): p. 12549-12555.
97. Xu, X., et al., *Effect of sodium oleate adsorption on the colloidal stability and zeta potential of detonation synthesized diamond particles in aqueous solutions*. Diamond and Related Materials, 2005. **14**(2): p. 206-212.
98. McHedlov-Petrosyan, N.O., et al., *Colloidal properties and behaviors of 3 nm primary particles of detonation nanodiamonds in aqueous media*. Physical Chemistry Chemical Physics, 2015. **17**(24): p. 16186-16203.
99. Petit, T., et al., *Oxygen hole doping of nanodiamond*. Nanoscale, 2012. **4**(21): p. 6792-6799.
100. Williams, O.A., et al., *Size-Dependent Reactivity of Diamond Nanoparticles*. ACS Nano, 2010. **4**(8): p. 4824-4830.
101. Mandal, S., et al., *Surface Zeta Potential and Diamond Seeding on Gallium Nitride Films*. ACS Omega, 2017. **2**(10): p. 7275-7280.
102. Liu, D., et al., *Impact of diamond seeding on the microstructural properties and thermal stability of GaN-on-diamond wafers for high-power electronic devices*. Scripta Materialia, 2017. **128**: p. 57-60.

103. Ōsawa, E., *Monodisperse single nanodiamond particulates*. Pure and Applied Chemistry, 2008. **80**(7): p. 1365-1379.
104. Han, X., et al., *Synthesis and characterisation of ambient pressure dried composites of silica aerogel matrix and embedded nickel nanoparticles*. The Journal of Supercritical Fluids, 2015. **106**: p. 140-144.
105. Le, Q.T., *Laser ablation dentin and its medical application*, in *Material chemistry*. 2017, Université de Bordeaux: Bordeaux, France.
106. D'Amore, J.J., et al., *Methods for speciation of metals in soils: a review*. Journal of Environmental Quality, 2005. **34**(5): p. 1707-1745.
107. Egerton, R.F., *Physical Principles of Electron Microscopy*. 2016, Switzerland: Springer
108. Cambridge, U.o. *Looking at materials up close - The Scanning Electron Microscope (SEM)*. 2021 [3.5.2021]; Available from: <https://www.rrutc.msm.cam.ac.uk/outreach/articles/the-scanning-electron-microscope>.
109. Goodhew, P.J., *Electron Microscopy and Analysis*. 2001, London Taylor & Francis.
110. Encyclopædia Britannica, I. *Transmission electron microscope*. 2021 [3.5.2021]; Available from: <https://www.britannica.com/technology/transmission-electron-microscope>.
111. West, A.R., *Solid State Chemistry and its Applications*. John Wiley & Sons Ltd, 2014.
112. 2021 Gatan, I. *Spectroscopy*. 2021 [3.5.2021]; Available from: <https://eels.info/about/techniques/eels-0>.
113. Ltd, J. *Electron energy-loss spectroscopy*. 2021 [3.5.2021]; Available from: [https://www.jeol.co.jp/en/words/emterms/search\\_result.html?keyword=EELS](https://www.jeol.co.jp/en/words/emterms/search_result.html?keyword=EELS).
114. Unruh, D.K. and T.Z. Forbes, *X-ray Diffraction Techniques*, in *Analytical Geomicrobiology: A Handbook of Instrumental Techniques*, D.S. Alessi, H. Veeramani, and J.P.L. Kenney, Editors. 2019, Cambridge University Press: Cambridge. p. 215-237.
115. Yadav, L.D.S., *Introduction to Spectroscopy (Spectrometry)*. Organic Spectroscopy. 2005, Dordrecht: Springer.
116. Instruments, S.S. *Instrument Design* 2020 [30.11.2020]; Available from: <https://www.ssi.shimadzu.com/products/uv-vis-spectrophotometers/faqs/instrument-design.html>.

117. Instruments, E. *What is a Spectrometer?* 2020 [30.11.2020]; Available from: <https://www.edinst.com/us/blog/what-is-a-spectrometer/>.
118. SphereOptics, *Integrating sphere technical guide*. 2004: SphereOptics Hoffman-LLC.
119. Instruments, S.S. *Diffuse Reflectance Measurement*. 2020 [30.11.2020]; Available from: <https://www.ssi.shimadzu.com/products/uv-vis-spectrophotometers/diffuse-reflectance-measurement.html>.
120. Ferraro, J.R., K. Nakamoto, and C.W. Brown, *Introductory Raman Spectroscopy* Elsevier, 2003.
121. Instruments, E. *What is Raman Spectroscopy?* 2021 [3.5.2021]; Available from: <https://www.edinst.com/blog/what-is-raman-spectroscopy/>.
122. Knight, D.S. and W.B. White, *Characterization of diamond films by Raman spectroscopy*. *Journal of Materials Research*, 2011. **4**(02): p. 385-393.
123. Perkins, W.D., *Fourier Transform-Infrared Spectroscopy*. *Topic in chemical instrumentation*, 1986. **63**: p. 5-10.
124. Coates, J., *Interpretation of Infrared Spectra, A Practical Approach*. *Encyclopedia of Analytical Chemistry*. 2000, Chichester: John Wiley & Sons Ltd. 10815–10837.
125. GmbH, A.P. *Attenuated total reflectance (ATR)*. 2021 [3.5.2021]; Available from: <https://wiki.anton-paar.com/en/attenuated-total-reflectance-atr/>.
126. *Zetasizer Nano Series User Manual* Malvern, 2013.
127. Standardization, I.O.f., *Particle size analysis — Dynamic light scattering (DLS)*. 2008.
128. Cosgrove, T., *Colloid Science - Principles, Methods and Applications*. 2005, Bristol Colloid Centre: Blackwell Publishing Ltd.
129. Kaszuba, M., et al., *High-concentration zeta potential measurements using light-scattering techniques*. *Philosophical Transactions of the Royal Society A: Mathematical, Physical and Engineering Sciences*, 2010. **368**(1927): p. 4439-4451.
130. Balbuena, P.B. and K.E. Gubbins, *Theoretical Interpretation of Adsorption Behavior of Simple Fluids in Slit Pores*. *Langmuir* 1993. **9**(7): p. 1801-1814.
131. Condon, J., *Surface Area and Porosity Determinations by Physisorption: Measurements and Theory*. Elsevier Science, 2006.
132. Sing, K.S.W., et al., *Reporting physisorption data for gas solid systems* *Pure and Applied Chemistry*, 1985. **57**(4): p. 603—619.

133. Alothman, Z., *A Review: Fundamental Aspects of Silicate Mesoporous Materials*. Materials, 2012. **5**(12): p. 2874-2902.
134. Wang, Z., et al., *Nano-Scale Pore Structure and Its Multi-Fractal Characteristics of Tight Sandstone by N<sub>2</sub> Adsorption/Desorption Analyses: A Case Study of Shihezi Formation from the Sulige Gas Field, Ordos Basin, China*. Minerals, 2020. **377**(4): p. 1-21.
135. Brunauer, S., P.H. Emmett, and E. Teller, *Adsorption of Gases in Multimolecular Layers*. Journal of the American Chemical Society, 1938. **60**(2): p. 309-319.
136. Barrett, E.P., L.G. Joyner, and P.P. Halenda, *The Determination of Pore Volume and Area Distributions in Porous Substances. I Computations from Nitrogen Isotherms*. Journal of the American Chemical Society, 1951. **73**(1): p. 373-380.
137. Reede, S., F. Bunge, and M.J. Vellekoop, *Integration of Silica Aerogels in Microfluidic Chips*. Proceedings, 2017. **298**(4): p. 1-4.
138. Mochalin, V.N. and Y. Gogotsi, *Wet Chemistry Route to Hydrophobic Blue Fluorescent Nanodiamond*. Journal of American Chemical Society, 2009. **131**: p. 4594–4595.
139. Astuti, Y., N.R.J. Poolton, and L. Šiller, *Raman and Photoluminescence Spectroscopic Study of 1-Undecene Functionalized Nanodiamonds*. Materials Research Society Proceedings, 2013. **1597**.
140. Chung, P.H., E. Perevedentseva, and C.L. Cheng, *The particle size-dependent photoluminescence of nanodiamonds*. Surface Science, 2007. **601**(18): p. 3866-3870.
141. Praver, S. and R.J. Nemanich, *Raman spectroscopy of diamond and doped diamond*. Philosophical Transactions of the Royal Society A: Mathematical, Physical and Engineering Sciences, 2004. **362**(1824): p. 2537-65.
142. Shenderova, O., et al., *Detonation nanodiamonds as UV radiation filter*. Diamond and Related Materials, 2007. **16**(12): p. 2003-2008.
143. Barbosa, D.C., et al., *Activation energies for the growth of diamond films and the renucleation of diamond grains during film growth*. Journal of Vacuum Science & Technology B, Nanotechnology and Microelectronics: Materials, Processing, Measurement, and Phenomena, 2014. **32**(3): p. 031808.
144. Ruvinskiy, P., et al., *Nano-Silicon Containing Composite Graphitic Anodes with Improved Cycling Stability for Application in High Energy Lithium-Ion Batteries*. ECS Journal of Solid State Science and Technology, 2013. **2**(10): p. M3028-M3033.

145. Garai, J. and S.E. Haggerty, *Infrared absorption investigations confirm the extraterrestrial origin of carbonado diamond*. The astrophysical journal, 2006. **653**(2): p. 153-156.
146. Donnet, J., P., et al., *<sup>13</sup>C NMR characterization of nanodiamonds* Comptes Rendus de l'Académie des Sciences - Series IIC - Chemistry, 2000. **3**: p. 831–838.
147. Vukajlovic, J., et al., *Diamond-doped silica aerogel for solar geoengineering*. Diamond and Related Materials, 2021. **117**: p. 108474.
148. Vinogradova, E., M. Estrada, and A. Moreno, *Colloidal aggregation phenomena: Spatial structuring of TEOS-derived silica aerogels*. Journal of Colloid and Interface Science, 2006. **298**(1): p. 209-212.
149. Li, M., H. Jiang, and D. Xu, *Preparation of sponge-reinforced silica aerogels from tetraethoxysilane and methyltrimethoxysilane for oil/water separation*. Materials Research Express, 2018. **5**(4): p. 045003.
150. Khedkar, M.V., et al., *Surface modified sodium silicate based superhydrophobic silica aerogels prepared via ambient pressure drying process*. Journal of Non-Crystalline Solids, 2019. **511**: p. 140-146.
151. Snail, K., et al., *Hemispherical Transmittance Of Several Free Standing Diamond Films*. 33rd Annual Technical Symposium. Vol. 1146. 1989: SPIE.
152. Buratti, C. and E. Moretti, *Glazing systems with silica aerogel for energy savings in buildings*. Applied Energy, 2012. **98**: p. 396-403.
153. Shimadzu. *Shimadzu UV-VIS-NIR Spectrophotometer*. 2020 [14.04.2020]; Available from: [https://www.shimadzu.com/an/molecular\\_spectro/uv/solidspec/solid.html](https://www.shimadzu.com/an/molecular_spectro/uv/solidspec/solid.html).
154. Eaton-Magana, S., J.E. Shigley, and C.M. Breeding, *Observations on HPHT-Grown Synthetic Diamonds: A Review*. Gems & Gemology, 2017. **53**(3): p. 262-284.
155. Narayan, R.J., et al., *Microstructural and biological properties of nanocrystalline diamond coatings*. Diamond and Related Materials, 2006. **15**(11-12): p. 1935-1940.
156. Egerton, R.F. and M.J. Whelan, *The electron energy loss spectrum and band structure of diamond*. Philosophical Magazine, 1974. **30**(4): p. 739-749.
157. Tafel, A., et al., *Fabrication and structural characterization of diamond-coated tungsten tips*. Diamond and Related Materials, 2019. **97**: p. 107446.
158. Aleksenskii, A.E., et al., *Optical Properties of Nanodiamond Layers*. Physics of the Solid State, 2001. **43**(1): p. 140–145.

159. Daniels, J.A., R. Krishnamurthi, and S.S. Rizvi, *A Review of Effects of Carbon Dioxide on Microbial Growth and Food Quality*. Journal of Food and Protection, 1985. **48**(6): p. 532-537.
160. Byck, H.T., *Effect of dissolved CO<sub>2</sub> on the pH of water*. Science, 1932. **75**(1938): p. 224.
161. IUPAC, *Reporting physisorption data for gas/solid systems with Special Reference to the Determination of Surface Area and Porosity*, in *Pure & Applied Chemistry*. 1985. p. 603—619.
162. Van der Voort, P., et al., *Plugged hexagonal templated silica: a unique micro- and mesoporous composite material with internal silica nanocapsules*. Chemical Communications, 2002(9): p. 1010-1011.
163. Groen, J.C., L.A.A. Peffer, and J. Pérez-Ramírez, *Pore size determination in modified micro- and mesoporous materials. Pitfalls and limitations in gas adsorption data analysis*. Microporous and Mesoporous Materials, 2003. **60**(1-3): p. 1-17.